University of Nebraska - Lincoln
DigitalCommons@University of Nebraska - Lincoln

Publications of the US Geological Survey | US Geological Survey

2009

CIRCULATION AND WATER PROPERTY VARIATIONS IN THE NEARSHORE ALASKAN BEAUFORT SEA (1999 – 2007)

Thomas J. Weingartner
University of Alaska Fairbanks

Seth L. Danielson
University of Alaska Fairbanks

Jeremy L. Kasper
University of Alaska Fairbanks

Stephen R. Okkonen
University of Alaska Fairbanks

Follow this and additional works at: https://digitalcommons.unl.edu/usgspubs

 Part of the Earth Sciences Commons

Weingartner, Thomas J.; Danielson, Seth L.; Kasper, Jeremy L.; and Okkonen, Stephen R., "CIRCULATION AND WATER PROPERTY VARIATIONS IN THE NEARSHORE ALASKAN BEAUFORT SEA (1999 – 2007)" (2009). *Publications of the US Geological Survey*. 88.
https://digitalcommons.unl.edu/usgspubs/88

This Article is brought to you for free and open access by the US Geological Survey at DigitalCommons@University of Nebraska - Lincoln. It has been accepted for inclusion in Publications of the US Geological Survey by an authorized administrator of DigitalCommons@University of Nebraska - Lincoln.

OCS Study MMS 2009-035

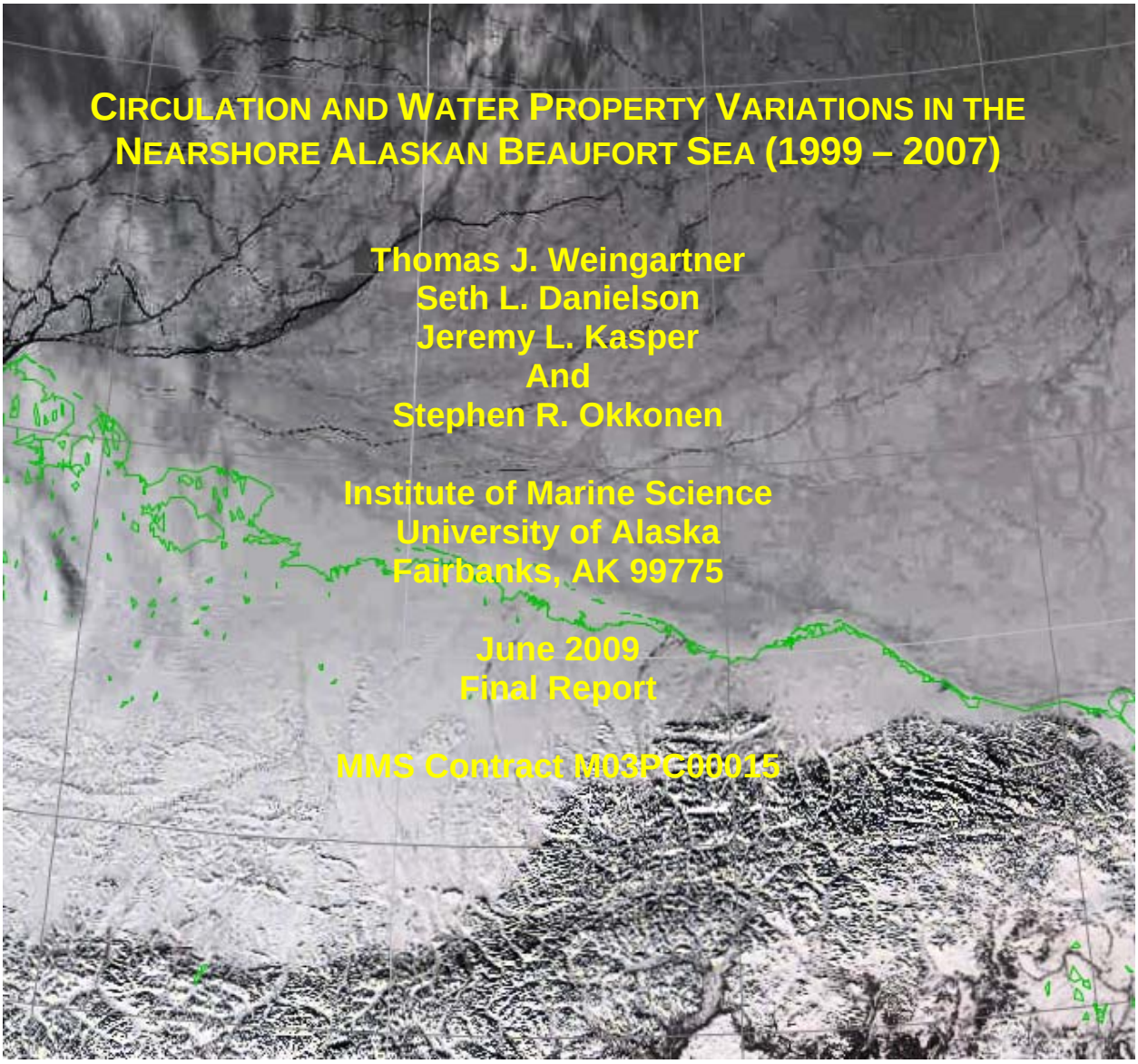

CIRCULATION AND WATER PROPERTY VARIATIONS IN THE NEARSHORE ALASKAN BEAUFORT SEA (1999 – 2007)

Thomas J. Weingartner
Seth L. Danielson
Jeremy L. Kasper
And
Stephen R. Okkonen

Institute of Marine Science
University of Alaska
Fairbanks, AK 99775

June 2009
Final Report

MMS Contract M03PC00015

MMS
US Department of Interior
Minerals Management Service
Alaska Outer Continental Shelf Region

CIRCULATION AND WATER PROPERTY VARIATIONS IN THE NEARSHORE ALASKAN BEAUFORT SEA

Thomas J. Weingartner
Seth L. Danielson
Jeremy L. Kasper
and
Stephen R. Okkonen

Institute of Marine Science
University of Alaska
Fairbanks, AK 99775

This project was funded by the U.S. Department of the Interior Minerals Management Service (MMS), Alaska Outer Continental Shelf Region, Anchorage Alaska, under Contract No M03PC00015, as part of the MMS Alaska Environmental Studies Program.

June 2009

The opinions, findings, conclusions, or recommendations expressed in this report or product are those of the authors and do not necessarily reflect the views of the U.S. Department of the Interior, nor does mention of trade names or commercial products constitute endorsement or recommendation for use by the Federal Government.

TABLE OF CONTENTS

LIST OF TABLES

LIST OF FIGURES

ABSTRACT

Six years of current meter and water property data were collected year-round (1999 – 2007) from the landfast ice zone of the nearshore Alaskan Beaufort Sea (ABS). The data show large seasonal differences in the circulation that is defined by the set-up and breakup of the landfast ice. During the open water season (July – mid-October) mid-depth currents often exceed 20 cm-s^{-1}, whereas during the landfast ice season (mid-October – June) these currents are generally <10 cm-s^{-1}. Tidal currents are feeble (<3 cm-s^{-1}) year-round and probably do not play a dynamically significant role on the inner shelf.

Most (>90%) of the current variability is in the along-shore direction year-round. In general the mean currents are not statistically different from zero over the whole record or in individual seasons. Open water currents are significantly correlated with the local winds, but currents beneath the landfast ice are not. Calculations conducted over both seasons suggest along-shore sea-level gradients are about 10^{-6}, with the magnitude of these gradients being only slightly larger during the open water season than during the landfast ice season. These gradients are presumably set-up by the winds during the open water season, but their origin during the landfast ice season is unknown. However, preliminary model studies indicate that spatial variations in the underice friction coefficient are capable of establishing along-shore pressure gradients of this magnitude. During the open water season upwelling-favorable winds force westward flows that are strongly sheared in the vertical and with maximum currents at the surface. In contrast, downwelling favorable winds are weakly sheared in the vertical. The asymmetric current structure is presumed due to differences in stratification; strongly stratified during upwelling (westward) winds and weakly stratified during downwelling (eastward) winds.

Cross-shore flows are generally small (~3 cm s^{-1}) compared to along-shore currents. However, cross-shore flows of ~10 cm-s^{-1} were observed during the landfast ice season when the spring freshet resulted in an offshore spreading of a buoyant plume beneath the landfast ice. Although measured cross-shore flows are generally small, satellite imagery suggests that frontal instabilities associated with low-salinity nearshore plumes can transport inner shelf waters offshore to the Beaufort shelfbreak during the open water season. Observations from elsewhere in the Arctic suggest that cross-shore current speeds associated with instabilities can be as large as 30 cm s^{-1}.

Our results suggest that oil spilled beneath the landfast ice will stay within the vicinity of the oil spill source as current speeds will rarely exceed the threshold velocity required to transport an oil slick once it has attained its equilibrium thickness. We find that an underice oil spill has a 90% probability of remaining within 20 km of its origin over a 12-day period. Because of the broad spatial coherence in the flow field (~100 km in along-shore extent), underice currents could be monitored at one point and transmitted real-time to cleanup crews in the event of an underice spill. This information would verify the current speeds and whether oil would stay in the vicinity of the spill. Oil spilled during the open water season could be rapidly dispersed over great distances (~200 km in 12 days) in both the along- and cross-shore directions, however.

Water properties also vary seasonally in response to ice formation and melting, the spring freshet, and wind-mixing. Salinities increase and temperatures decrease throughout the winter due to freezing and brine expulsion from sea-ice. During the spring freshet, the inner shelf is strongly stratified and remains so until the ice retreats and downwelling winds mix the water column. The annual suspended sediment cycle, based on transmissivity measurements, suggests

rapid deposition of river borne sediments beneath the landfast ice during the spring freshet, with re-suspension and transport occurring throughout the open water season depending upon storm frequency. Re-suspension and transport is also vigorous during the formation of landfast ice and we conclude that much sediment is incorporated into the ice matrix at this time of the year. Ice-incorporated sediments are either transported with the ice or returned to the water column during melting the following summer.

There are several important issues that we believe need to be addressed in the future. Modeling of the landfast ice zone requires an understanding of the role that ice-water friction plays in this region. Measurements of the spatially and temporally varying underice topography are critical to understanding the dynamics of this shelf. Second, the source and magnitude of the along-shore pressure gradients responsible for the underice currents needs to be determined. Third, it is not clear if the findings based on current measurements made in water depths $\leq$17 m apply to deeper portions of the landfast ice zone. Hence the cross-shore coherence in the underice circulation field needs to be determined. Fourth, the introduction of freshwater creates stratification that can lead to an asymmetric current response to wind-forcing during the open water season. Observations on the thermohaline structure of the Beaufort shelf are needed in order to understand and model the circulation field during the open water season. Cross-shore salinity fronts, established by river runoff, can become unstable and cause energetic cross-shelf flows capable of carrying pollutants far offshore. The dynamics and kinematics of these features need study. Fifth, sediments can adsorb pollutants and be incorporated into the ice along with oil; hence we recommend that consideration be given to the potential role that ice plays in the transport of sediments and pollutants on this shelf.

I. INTRODUCTION

The nearshore zone (here defined as the portion of the shelf between the coast and the ~20 m isobath) of arctic shelves differs substantially from their mid- and low-latitude counterparts because of unique geomorphologic and climatological attributes. Arctic shelf tides are generally weak and rivers empty directly onto the shelf rather than into bays. Thus, the nearshore effectively functions as an estuary, insofar as it serves as the transition and mixing zone between the Arctic's terrestrial and marine environments. Climatologically, the large annual cycle in air-sea heat exchange and freshwater runoff cause enormous seasonal variations in the buoyancy and momentum fluxes to the shelf. For example, more than 90% of the annual river discharge from arctic rivers (defined here as rivers whose watersheds lie entirely north of the Arctic Circle) occurs over a brief period in early summer. (For larger rivers, such as the Mackenzie or Lena, approximately 90% of the annual discharge occurs between June and September.) Much of this discharge occurs before the landfast ice has completely retreated. Landfast ice is a unique characteristic of most arctic shelves. During the winter months it is anchored to the seafloor out to the 2 m isobath [*Reimnitz*, 2000] and can extend offshore to between the 20 and 40 m isobath [*Reimnitz and Kempema*, 1984; *Macdonald and Carmack*, 1991]. In contrast to drifting pack ice found over the outer shelf and basin, landfast ice is virtually immobile. On windward shelves, such as the Beaufort, its offshore boundary is highly deformed when pack ice collides with the landfast ice edge. On lee shelves, such as the Laptev Sea, the offshore edge of the landfast ice is typically smooth and terminates at the edge of a polynya. The width of the landfast ice zone varies amongst arctic shelves; it extends ~100 km offshore in the East Siberian Sea [*Morris et al*., 1999] but is much narrower, and in a few places absent, on the Chukchi shelf. Because it is effectively immobile, landfast ice inhibits the transfer of momentum from the wind to the ocean and therefore drastically influences arctic shelf

dynamics. Moreover, it probably reduces communication between nearshore and outer shelf waters where the wind stress is transmitted more efficiently to the ocean. As will be seen the landfast ice effectively determines seasonal conditions on arctic shelves.

Herein we report on year-round measurements of currents, temperature, salinity, transmissivity and fluorescence (which provide qualitative measures of suspended load and chlorophyll, respectively) obtained from moored instruments in the Alaskan Beaufort Sea that were deployed between 1999 and 2007. The primary goal of the program was to assess the magnitude of underice currents in the vicinity of Prudhoe Bay and elsewhere along the Alaska Beaufort Sea shelf where offshore petroleum development activities are being considered. The present effort builds on earlier work funded by MMS and previously reported by *Weingartner et al.* (2005). The measurements are needed to guide response procedures in the event of an underice oil spill. Laboratory studies indicate that oil slicks at equilibrium thickness and in contact with immobile, smooth ice begin moving at current speeds of from 3 cm-s^{-1} for low viscosity oils to 7 cm-s^{-1} for high viscosity oils [*Cox and Schultz,* 1980]. Threshold velocities increase to 15 - 25 cm-s^{-1} as the underice roughness increases.

Prior current measurements in this region yielded contradictory results. *Aagaard's* [1984] measurements suggested that current speeds seldom exceed 10 cm-s^{-1} in the landfast ice portion of the Beaufort Sea, while *Matthews* [1981] inferred that speeds of up to 35 cm-s^{-1} were possible, at least occasionally. Both studies were of relatively short-term duration, however with instruments moored close to the seabed. The measurements reported here were made year-round from bottom-mounted acoustic Doppler current profilers (ADCPs) within the landfast ice zone. Although the geographic scope of the program was limited, the results provide a regional basis for regional oil spill response planning. In addition, the data provide a look at this unique marine

environment and raise a number of questions pertinent to the physical oceanography of nearshore arctic shelves influenced by landfast ice.

The outline of the report is a follows. Section II provides background information on the Alaskan Beaufort Sea shelf. The field program is described in Section III and the results and dynamical inferences are presented in Section IV. Section V explores some of the possible influences of freshwater runoff on the oceanic dispersal of any contaminants introduced at the coast. Conclusions and recommendations are summarized in section VI.

II. THE REGIONAL SETTING

The Alaskan Beaufort Sea shelf (**Figure 1**) extends ~500 km eastward from Point Barrow to the Mackenzie portion of the Beaufort Sea shelf in Canadian waters. The shelf width is ~80 km as measured from the coast to the 200 m isobath. Shelf depths grade smoothly offshore with bottom slopes typically being $\sim 10^{-3}$ inshore of the 100 m isobath.

Sea ice can cover the shelf year-round, although more typically the inner shelf (and in recent years the entire shelf) is ice-free during the summer months. Landfast ice begins to form in October and extends 20 – 40 km offshore through mid-June so that it covers nearly 25% of the shelf area [*Barnes et al*., 1984] through most of the year. The landfast ice is relatively smooth adjacent to the coast, but is increasingly deformed offshore. Maximum ridge intensity and height increases moving seaward, and the magnitudes of both variables increase through winter [*Tucker et al.,* 1979]. Both parameters may also vary along-shelf and it appears that the landfast ice zone on the Mackenzie shelf is much less deformed than on the Alaskan Beaufort shelf [*Tucker et al.* 1979]. Ice keels form beneath the ridges and can gouge the seafloor [*Barnes et al*., 1984] and form piles of grounded ice, stamukhi, along the seaward edge of the landfast ice. The stamukhi

appears to be important in protecting the inner shelf (and landfast ice) from pack ice forces [*Reimnitz and Kempena*, 1984] and on the Mackenzie shelf provides an effective barrier to the

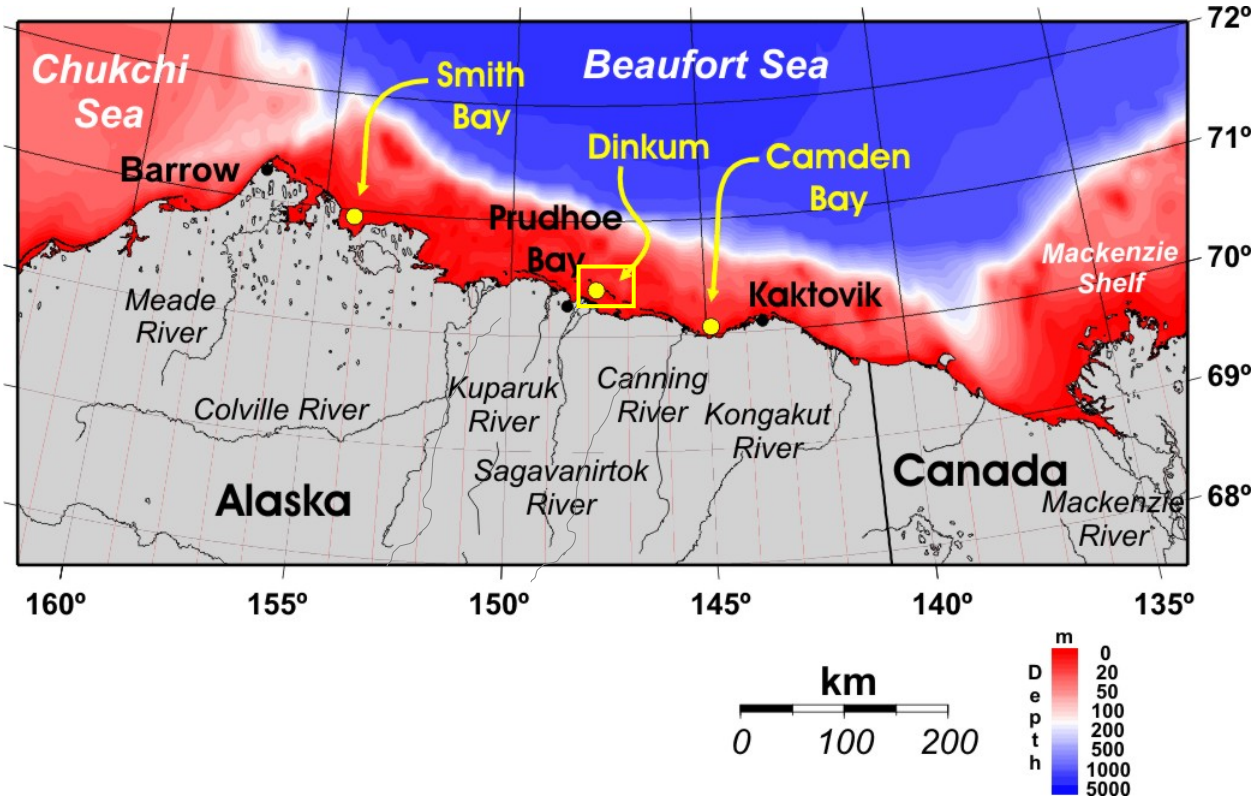

Figure 1. Map of the Alaskan Beaufort Sea and North Slope with place names and subdivisions indicated. Moorings were located at Smith Bay, Dinkum, and Camden Bay and within the yellow box encircling the Dinkum site. Mooring locations in this box are shown in **Figure 4**.

exchange between nearshore waters and offshore waters [*Macdonald and Carmack,* 1991].

The ocean circulation and ice deformation are related to the seasonally varying winds. These we summarized in the form of monthly statistics using the archived National Weather Service wind record in Barrow from 1949 – 2005. The statistics plotted in **Figure 2** are based on the alongshore component of the winds, which accounts for most of the variance in the winds and which are primarily responsible for forcing shelf circulations. In general, northeasterly winds prevail throughout the year. On a monthly basis the majority of the alongshore winds are westward (upwelling favorable) and westward winds are, on average, stronger than eastward

(downwelling-favorable) winds. There are however, substantial seasonal differences. Westward winds are strongest in late fall and early winter and occur most frequently in October and November and in March. Westward winds are only slightly more frequent than eastward winds in July and August, although westward winds are stronger in these months. Thus, on average, upwelling favorable conditions prevail throughout the year. Although the alongshelf wind stress

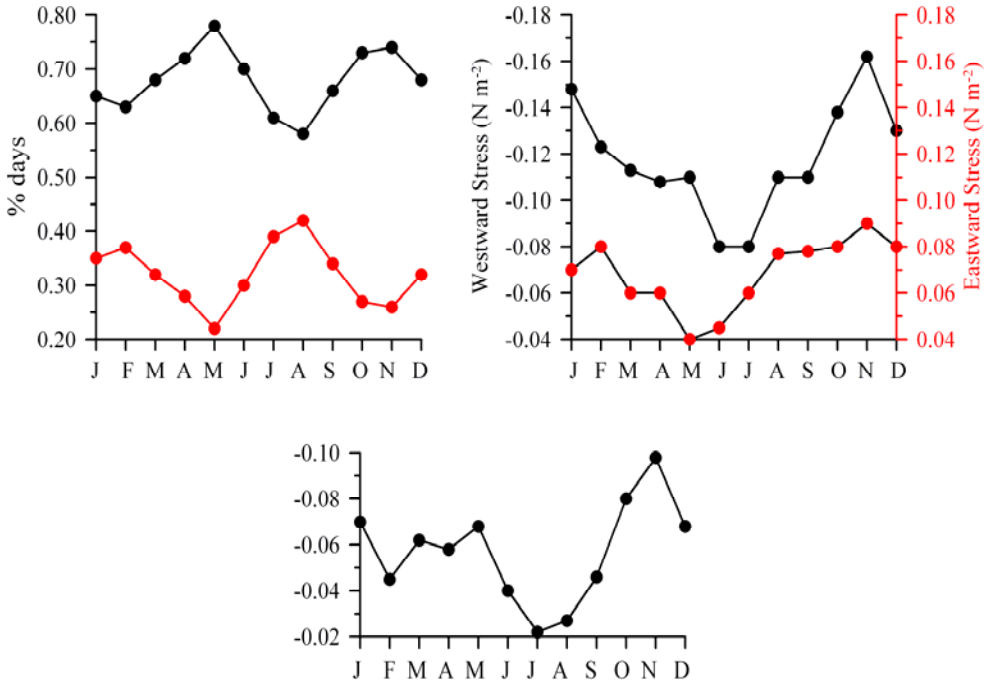

Figure 2. Mean monthly wind statistics of the alongshore winds based on the 1949 – 2005 National Weather Service observations from Barrow Alaska. Upper left panel shows the percentage of days in a month in which there are westward (upwelling-favorable; black circles) and eastward (downwelling-favorable; red circles) winds. The upper right panel shows the mean monthly wind stress for eastward and westward winds. The bottom panel shows the mean monthly wind stress (which is westward in all months).

component is important in the ocean circulation, the north-south component plays an important role in ice dynamics. In particular, winter winds are primarily onshore and thus force pack ice onshore and deform the landfast ice edge. Less frequent offshore or southerly winds can result in detachment of the landfast ice (breakouts). These seasonal variations are primarily related to the deep high pressure cell centered over the Arctic Ocean in winter. However, the high pressure

system weakens in summer and fall, when low-pressure systems invade the Beaufort Sea from the North Pacific [*Maslanik et al.*, 1999].

Seasonally varying mesoscale winds may substantially alter the synoptic wind field in the nearshore zone, however. For example, a persistent summer sea breeze results in mean westward winds within ~25 km of the coast [*Kozo*, 1982a, b]. *Brower et al.* [1988] indicate that mean summer winds are easterly, which suggests there is a reversal in wind direction on crossing the shelf. From October through April mountain barrier baroclinicity [*Kozo*, 1980; 1984] can produce along-shore divergence in the wind field. This effect occurs when the southward flow of low-level cold air from the Arctic Ocean is blocked along the northern flank of the Brooks Range. The resulting isopycnal slopes induce eastward surface winds of about 15 m s^{-1} over a horizontal width scale of 200 – 300 km. The western Beaufort coast is rarely influenced by the mountain barrier effect because it lies more than 300 km north of the Brooks Range, but the eastern Beaufort coast lies within 60 km of the mountains. Consequently, winds can be westward over the western Beaufort coast but eastward along the eastern coast. *Kozo* [1984] estimated that the mountain barrier baroclinicity effect occurs ~20% of the time during winter.

Three distinct oceanic regimes bound the Alaskan Beaufort Sea. To the west, waters of Pacific Ocean origin flow northward from Bering Strait and across the Chukchi shelf. While this flow divides along three main branches across the Chukchi shelf, the one most relevant for the Beaufort shelf is the outflow through Barrow Canyon in the northeast Chukchi Sea [*Mountain et al.*, 1976; *Aagaard and Roach*, 1990; *Weingartner et al.,* 1998; *Weingartner et al., 2005*]. Variability in the canyon outflow flow is large, especially in fall and winter, and mainly due to fluctuations in the regional winds [*Weingartner et al.,* 1998; *Weingartner et al., 2005; Woodgate et al*., 2005]. Some of the Barrow Canyon outflow continues eastward as a subsurface current (or

slope undercurrent) along the Beaufort shelfbreak and slope where it forms the upper halocline waters of the Canada Basin [*Mountain et al.*, 1976; *Aagaard*, 1984; *Pickart*, 2004; *Pickart et al*., 2005, *Nikopolous et al*., in press]. Under weak westward winds or eastward winds some of the water exiting Barrow Canyon rounds Pt. Barrow and continues onto the inner portion of the western Beaufort shelf (Okkonen, pers. comm.).

The outer shelf and continental slope provide the offshore boundary for the Alaskan Beaufort Sea. In the upper 50 m or so the flow is westward and part of the southern limb of the wind-driven Beaufort Gyre. This flow can occasionally be reversed by strong westerly winds and/or by occasional shelfbreak upwelling that advects eastward momentum from the slope undercurrent onto the shelf at least as far inshore as the 50 m isobath [*Aagaard*, 1984; *Pickart* 2004; *Nikopolous et al*., in press].

The Mackenzie shelf joins the Alaskan Beaufort shelf to the east and likely the the year-round discharge from the Mackenzie River influences the eastern Beaufort shelf [*Carmack et al.,* 1989; *Macdonald et al*., 1989; *Macdonald and Carmack,* 1991]. Mackenzie shelf water has been detected throughout much of the Canada basin, including the continental slope of the Chukchi and western Beaufort Sea as far as 160^{o}W longitude [*Guay and Falkner,* 1998; *MacDonald et al.*, 1999a]. Conceivably wind- driven currents transport Mackenzie shelf waters onto the Alaskan Beaufort shelf as well. In this regard, we note that the migratory behavior of arctic cisco provide indirect evidence for the intrusion of Mackenzie River waters onto the inner shelf of the Alaskan Beaufort Sea. These fish apparently require a nearshore band of low-salinity water in order to complete their annual migration between the Mackenzie and Colville rivers each summer [*Colonell and Galloway*, 1997]. The migratory corridor is presumably maintained by the westward drift of low-salinity water from the Mackenzie shelf. In addition to the

Mackenzie River, a large number of smaller rivers discharge into the Alaskan Beaufort Sea (**Figure 1**). These are asymmetrically distributed with most of them discharging into the central and eastern portions of the shelf. This asymmetric discharge, along with the influence of the Mackenzie, might establish an along-shelf density gradient that gives rise to an along-shelf baroclinic pressure gradient.

Our measurements were made in the vicinity of Prudhoe Bay, which lies about midway along the Alaskan Beaufort coast. Although a number of smaller streams empty into this area the three major rivers (and their watershed areas) that discharge into the study region are: the Sagavanirktok River (14900 km^2), the Kuparuk River (8100 km^2), and the Colville River (53,500 km^2). Only the first two of these were routinely gauged during the study period, and only seasonally, because the gauges are installed at breakup and removed in fall prior to freeze-up. The discharge time series for the two USGS gauged rivers are shown in **Figure 3** for each summer during which ocean measurements were made. (The spring freshet in summer 2002 was not detected as this occurred earlier than normal and prior to the installation of the gauge.) The annual discharge cycle is characterized by a rapid initiation and increase in runoff in late May or June that lasts about 2 weeks during which time nearly 90% of the annual discharge occurs. Following the spring freshet, the discharge is small and gradually decays to negligible values by October, although the decay can be punctuated by smaller, shorter-lived and sporadic discharge events following summer rain storms. The Colville has a similar seasonal cycle, although the discharge is substantially larger because of its larger drainage area. Unlike the Mackenzie and other large Arctic rivers, there is no measurable winter discharge from any North Slope rivers as most freeze to the bottom and all have watersheds lying entirely within drainages underlain by permafrost.

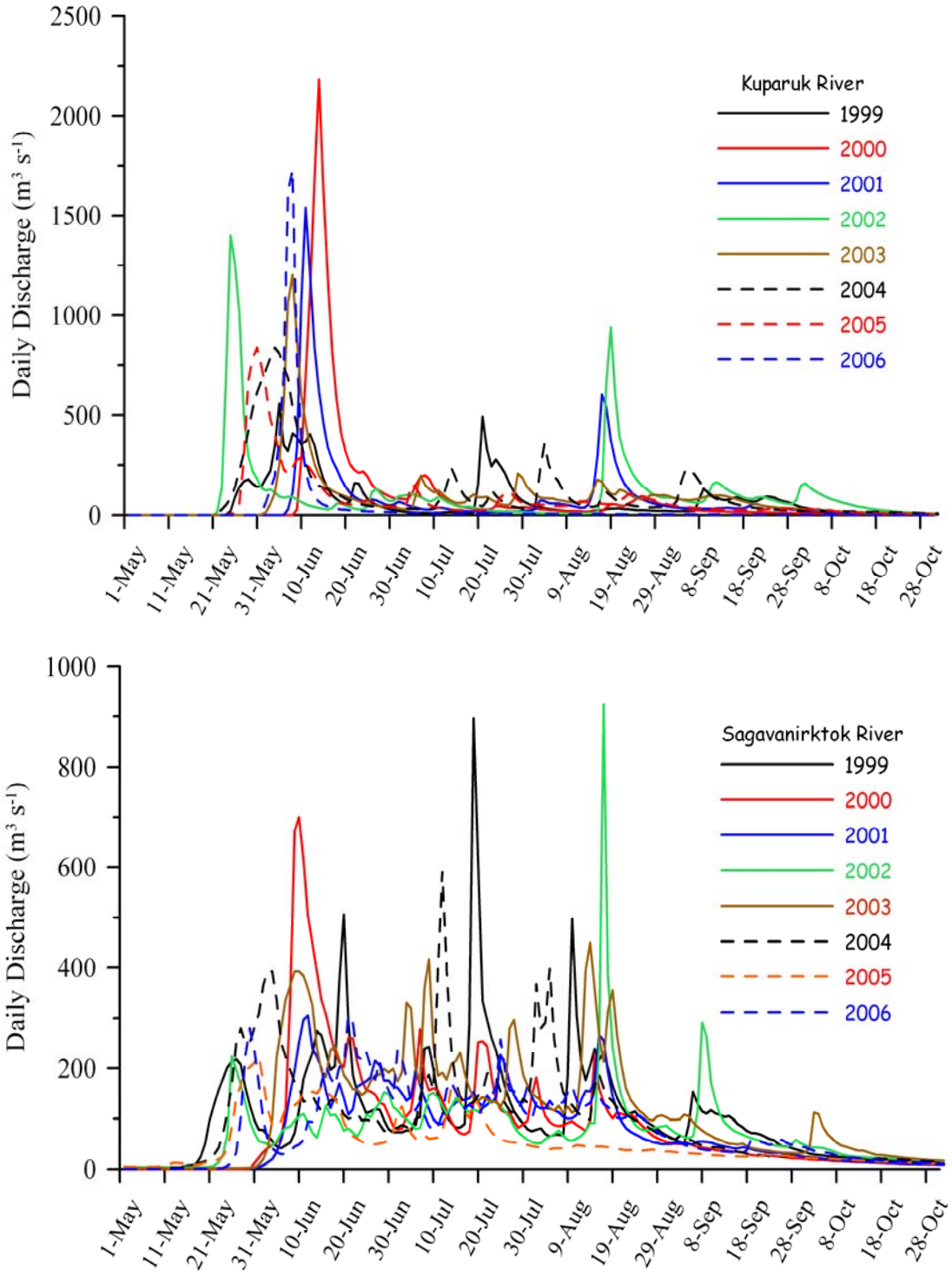

Figure 3. Mean daily discharge for the Kuparuk (upper panel) and Sagavanirktok (lower panel) rivers, May 1 – October 31, 1999 - 2006. The Sagavanirktok River gauge is located about 140 km inland from the coast so the discharge at the river mouth is greater than plotted.

III. METHODS

The data set described below comes from oceanographic moorings deployed (**Figure 4**) in Stefansson Sound and adjacent waters where present (Northstar Island) and future oil development efforts are targeted. Additional moorings were deployed in Camden Bay to the east and Smith Bay to the west of the Stefansson sound array (**Figure 1**). The mooring positions, sensor packages, bottom depths and problems encountered at each mooring site and for each year are summarized in **Tables 1 – 6**. All of these areas are important habitats or migratory routes for a variety of fish, birds, and marine mammals, including seals and bowhead whales. Of particular concern is the potential influence on the unique Boulder Patch kelp community in Stefansson Sound [*Dunton et al.*, 1982], which lies near the Liberty oil development prospect in the eastern portion of Stefannsson Sound. The moorings were deployed in late summer or fall of each year beginning August 1999 with the final recovery occurring in September 2008. At the onset of the program we were uncertain if moorings would survive drifting ice in this shallow (<10 m) environment so the initial deployments took advantage of partial protection afforded by a widely-separated chain of barrier islands and shoal, which lie 15 – 20 km offshore. In later years (after 2001), we felt confident that our mooring design minimized ice damage risk and so we deployed the REINDEER mooring in 12 m of water and the CROSS mooring in 17 m depth offshore of the islands. Moorings SMITH and CAMDEN were deployed in the second phase of the project to provide along-shore coverage. SMITH was ~235 km west of DINKUM and CAMDEN was ~120 km east of DINKUM. The majority of the moorings survived although there were problems. Two moorings were damaged by ice. The 2001 deployment of McCLURE was demolished by drifting ice 8 days after deployment. Although the instruments were recovered, the data are unusable for our purposes, except for the pressure record. The Smith Bay mooring was deployed in 2004 and recovered in 2005. However it was struck by ice in July

2005 during break up of the landfast ice. Again the instruments were recovered, but only that portion of the data record prior to dismantling of the mooring is usable. This mooring was not deployed subsequently. CAMDEN, DINKUM, and CROSS were deployed in August 2006, but a sever storm in October moved all the moorings and flipped the DINKUM so that only the pressure and temperature records from that mooring are useable after the storm. The same storm moved CROSS about 200 meters west of its deployed position. Although no damage was done to the instruments the conductivity cell was filled and compacted with re-suspended sediment and thus did not return useful salinity data after this event. In spite of these problems, we believe that the data presented here are the first year-round records from the nearshore zone of any arctic shelf.

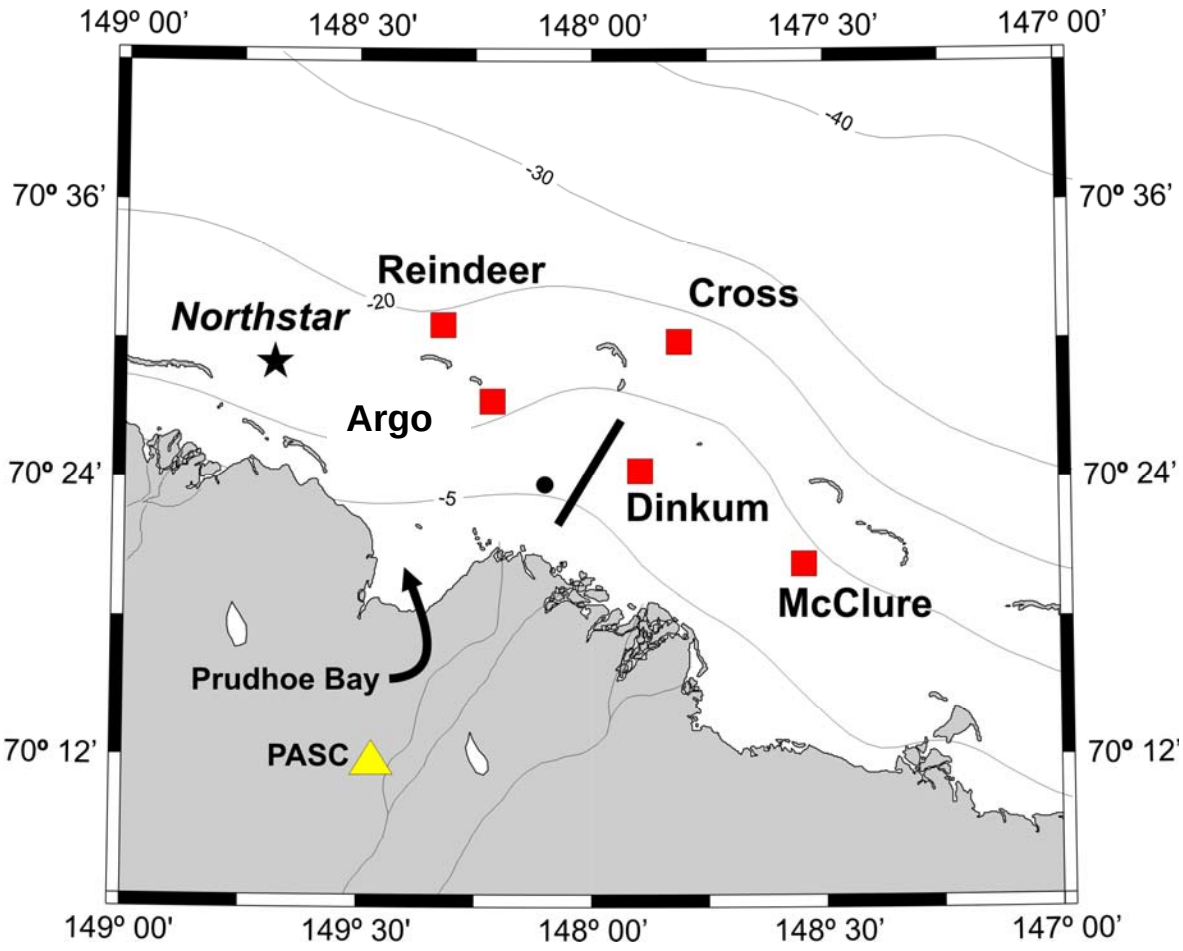

Figure 4. Location map showing current meter moorings and the PASC weather station in Deadhorse. Mooring specifics are given in Tables 1 – 6. Northstar is a production island constructed in 2000 and 2001, while the McCLURE mooring lies within the undeveloped Liberty field. The solid line near DINKUM indicates the approximate location of the June 2000 CTD transect. Depth contours are in meters.

Velocities were measured from either a 1200 or 600 kHz ADCP set in a gimbaled collar and mounted onto a mooring frame constructed from plastic angle stock (**Figure 5**). The gimbaled mount insured that the ADCP remained vertical even if the frame tilted from the horizontal by 20^{o} or less after deployment. (Observations made during recovery dives indicated that frame tilts were always negligible. Moreover, the ADCP tilt sensor indicates that the instruments remained level throughout the deployment.) Ancillary instruments (Seabird, Inc., MicroCats and/or SeaCats, with at least one mooring containing a strain-gauge pressure sensor) were fastened to the legs of each frame (**Figure 5**) and inclined to the vertical. At some locations the SeaCats included a transmissometer and a fluorometer. The inclined mount has no effect on the temperature and salinity measurements, however, the transmissometer lens might have collected settled sediment on occasion. We will note these possible biases when discussing the data.

The MicroCats and SeaCats were re-deployed after the first year without a post-calibration (performed by the manufacturer) while freshly calibrated instruments were used in succeeding years. Based on pre- and post-calibrations and comparisons with the winter T/S relationship along the freezing point curve we estimate that the salinity values are better than 0.1. (Salinity is evaluated using the practical salinity scale and is thus unitless.) The salinity record at mooring ARGO was erroneously high throughout the 2000 – 2001 winter and is not used. Hourly wind speed and direction were obtained from the Deadhorse airport, denoted as PASC in **Figure 4**.

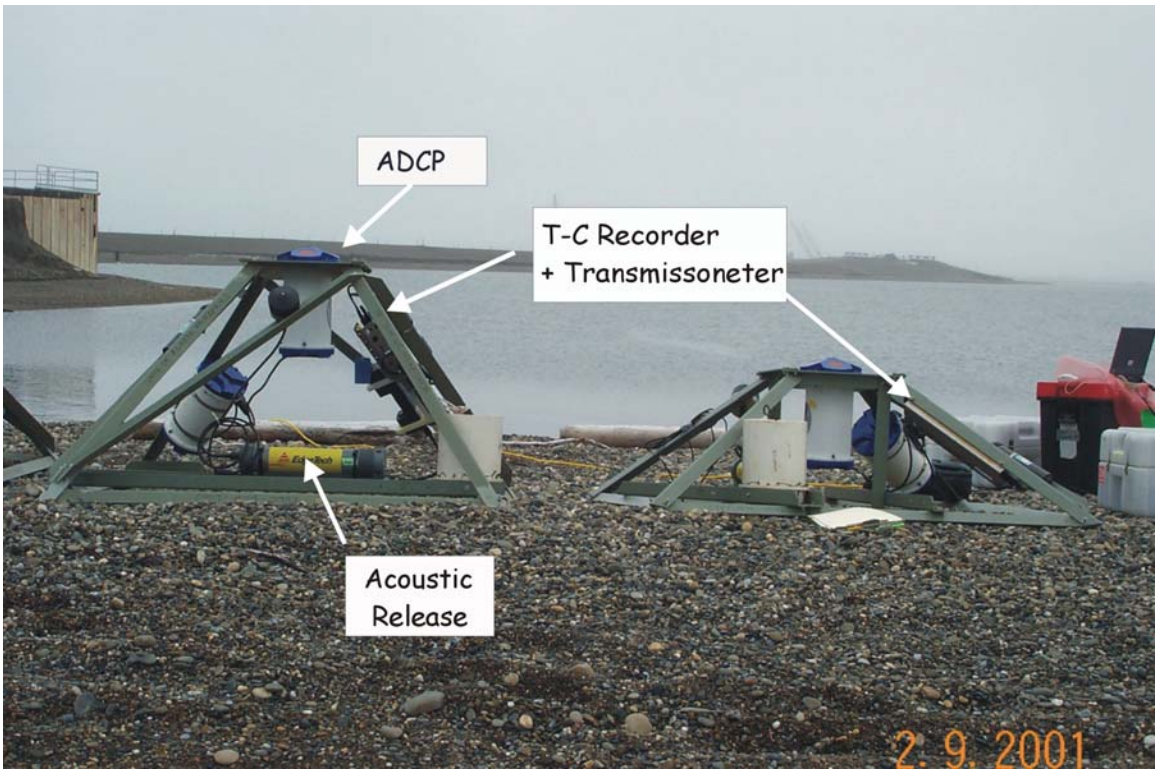

Figure 5. Photograph of two of the mooring frames with various instruments used in the study.

Table 1. Mooring Specifics for Data Analysis Period 2200/14/AUG/1999 - 2100/31/AUG/2000

Mooring Name	Latitude (ºN)	Longitude (ºW)	Instruments	Variables Measured	Bottom Depth (m)
ARGO	70º 27.177'	148º 12.722'	1200 kHz ADCP MicroCat	Water Velocity Temperature Salinity Water Pressure	8.4
DINKUM	70º 24.352'	147º 53.656'	1200 kHz ADCP SeaCat	Water Velocity Temperature Salinity Transmissivity	6.8
MCCLURE	70º 20.204'	147º 32.701'	1200 kHz ADCP SeaCat	Water Velocity Temperature* Salinity*	6.7
PASC	70º 11.7'	148º 27.7'	Anemometer	Wind Speed and Direction	

* McClure SeaCat data of 1999-2000 unusable because of instrument setup problem.

Table 2. Mooring Specifics for Data Analysis Period 2200/3/SEP/2000 - 1700/19/AUG/2001

Mooring Name	Latitude (ºN)	Longitude (ºW)	Instruments	Variables Measured	Bottom Depth (m)
ARGO	70º 27.172’	148º 12.666’	1200 kHz ADCP MicroCat	Water Velocity Temperature Salinity* Water Pressure	8.8
DINKUM	70º 24.371’	147º 53.632’	1200 kHz ADCP MicroCat	Water Velocity Temperature Salinity Water Pressure	7.3
MCCLURE	70º 20.164’	147º 32.700’	1200 kHz ADCP SeaCat MicroCat	Water Velocity Temperature Salinity Water Pressure Transmissivity	7.6
PASC	70º 11.7’	148º 27.7’	Anemometer	Wind Speed and Direction	

*ARGO salinity record in 2000-2001 not used because of sediment/biofouling and calibration problems.

Table 3. Mooring Specifics for Data Analysis Period 2200/2/SEPT/2001 - 1700/18/AUG/2002

Mooring Name	Latitude (ºN)	Longitude (ºW)	Instruments	Variables Measured	Bottom Depth (m)
ARGO	70° 27.168’	148° 12.654’	1200 kHz ADCP SeaCat	Water Velocity* Temperature Salinity Fluorescence	7.6
DINKUM	70° 24.371’	147° 53.632’	600 kHz ADCP SeaCat	Water Velocity* Temperature Salinity Transmissivity Fluorescence	6.8
MCCLURE	70° 20.164’	147° 32.700’	1200 kHz ADCP SeaCat	Water Velocity** Temperature** Salinity** Water Pressure Transmissivity** Fluorescence**	7.2
REINDEER	70° 30.539’	148° 19.212’	1200 kHz ADCP	Water Velocity*	12.7
PASC	70° 11.7’	148° 27.7’	Anemometer	Wind Speed and Direction	

* Bottom Track data on all ADCP instruments for this 2001 - 2002 was not collected. Water velocity data is good.
** McClure 2002-2003 mooring hit by ice 8 days into record and most data not usable. Pressure data is good.

Table 4. Mooring Specifics for Data Analysis Period August 2004-August 2005

Mooring Name	Latitude (°N)	Longitude (°W)	Instruments	Variables Measured	Bottom Depth (m)*
DINKUM	70° 24.4372'	147° 53.6563'	1200 kHz ADCP SeaCat	Water Velocity Temperature Salinity Water Pressure Transmissivity[1] Fluorescence	6.7 (6.9)
CAMDEN	70° 1.692'	144° 56.5846'	1200 kHz ADCP SeaCat	Water Velocity Temperature Salinity Water Pressure Transmissivity[1]	8.6 (8.7)
SMITH*+	70° 59.2881'	154° 1.9941'	1200 kHz ADCP SeaCat	Water Velocity Temperature Salinity[2] Water Pressure Transmissivity[1]	9.8 (9.5)

*Bottom Depth values outside (inside) parentheses indicate bottom depth estimated by the shipboard depth sounder (ADCP transducer reflection).

+Smith mooring demolished by ice on 7/24/2005. All instrumentation recovered by divers. To this date, complete ADCP records were recovered. Partial SeaCat records were recovered, however the SBE-16 instrument was flooded and destroyed. Mooring frame and ADCP external battery pack pressure housing were also destroyed.

[1] Transmissometer fouled in early fall – data not used.

[2] Conductivity cell clogged in September 2004 – data not used

Table 5. Mooring Specifics for Data Analysis Period August 2005-August 2006

Mooring Name	Latitude (ºN)	Longitude (ºW)	Instruments	Variables Measured	Bottom Depth (m)*
DINKUM	70° 24.4345’	147° 53.6898’	1200 kHz ADCP SeaCat	Water Velocity Temperature Salinity Water Pressure Transmissivity Fluorescence	7.3 (7.0)
CAMDEN	70° 1.689’	144° 56.532’	1200 kHz ADCP SeaCat	Water Velocity Temperature Salinity Water Pressure Transmissivity	8.7 (8.2)
REINDEER	70° 30.480’	148° 19.238’	600 kHz ADCP SeaCat	Water Velocity** Temperature Salinity[1] Water Pressure Transmissivity	12.6

* Bottom Depth values outside (inside) parentheses indicate bottom depth estimated by the shipboard depth sounder (ADCP transducer reflection).
** Water velocity measurements at Reindeer failed.
[1] Conductivity cell clogged in September 2005; data not used.

Table 6. Mooring Specifics for Data Analysis Period August 2006-September 2007/2008*

Mooring Name	Latitude (ºN)	Longitude (ºW)	Instruments	Variables Measured	Bottom Depth (m)**
DINKUM[1]	70º 24.441'	147º 53.6593'	1200 kHz ADCP SeaCat	Water Velocity Temperature Salinity Water Pressure Transmissivity Fluorescence	6.9 (6.9)
CAMDEN	70º 1.707'	144º 56.617'	1200 kHz ADCP SeaCat	Water Velocity Temperature Salinity[3] Water Pressure Transmissivity	8.1 (7.8)
CROSS[2]	70º 29.980'	147º 48.275'	600 kHz ADCP SeaCat	Water Velocity Temperature Salinity[3] Water Pressure Transmissivity	17.3 (16.3)

* All 3 moorings were moved by a large storm of October 2006.
**Bottom Depth values outside (inside) parentheses indicate bottom depth estimated by the shipboard depth sounder (ADCP transducer reflection).
[1]Waves flipped the DINKUM mooring on its side on 10/9/2006; velocity and salinity measurements made after this date are unusable.
[2]CROSS was not recovered in 2007 due to inclement weather conditions, but successfully recovered in August 2008.
[3]Conductivity cell clogged and unusable.

IV. RESULTS

1. Sea ice, currents, and winds

Before presenting the record length and seasonal statistics, we describe the seasonal cycle of currents and ice thickness for each year from the DINKUM mooring (**Figures 6 - 11**). Sea ice thickness, H_{ice}, was estimated from ADCP data as the difference between the bottom depth, Z_b (**Tables 1 - 6**), and the sum of the height of the transducer above the bottom, H_T, and the range from the transducer at which the intensity of the reflected acoustic signal was maximum, R, (e.g., $H_{ice} = \{Z_b - [H_T + R]\} * 1.12$), where the factor 1.12 is the ratio of the sea water density to the sea ice density. There is an uncertainty in the thickness estimates of 0.5 m because the ADCP integrates return signals over a 0.5 m depth bin. This error occasionally introduces high-frequency noise in the data which was eliminated by smoothing the ice thickness time series with a 5-day running mean. Sea ice forms in early October, gradually thickens to ~1.7 – 2.2 m by mid-March, and then remains constant through mid-June. Ice then melts rapidly and disappears by mid-July. The seasonal asymmetry in ice growth and ablation rates occurs because new ice forms on the underside of the ice with the freezing rate decreasing exponentially with H_{ice} [*Maykut*, 1986]. By contrast, ablation primarily occurs at the surface and proceeds rapidly once the surface snow cover melts or the surface is covered by low-albedo, silt-laden waters from river overflow [*Dean et al*., 1994; *Searcy et al.,* 1996].

Unfiltered velocity time series from the uppermost bin (bottom-track velocity; U_{BT} in the figures) are large and noisy when the surface is ice-free, but negligible once landfast ice is established. (A programming error in the 2001 - 2002 deployment voided the ice-tracking capability on the ADCPs. Instead of using U_{BT} to indicate the onset and end of the landfast ice period we used the large seasonal reduction in current speeds to approximate the dates of

landfast ice formation and retreat in this year.) The abrupt transition in U_{BT} allows unambiguous definition of the open water and landfast ice periods in each record. The data suggest that in each year landfast ice is present from mid-October through the end of June or the beginning of July, while the open water season (including drifting ice) spans the July through mid-October period. Thus landfast ice is present for about eight and one-half months. The figures also show time series of the vertical current shear, $d|\mathbf{V}|/dz$, (where $|\mathbf{V}|$ is the speed and z is depth) between the shallowest depth bin beneath the ice or sea surface and the deepest depth bin. At the DINKUM mooring the depth range over which these differences are computed varies ~4 m during the open water period to ~2 m during maximum ice thickness. Current speeds typically differ in the vertical by $\leq$4 cm s^{-1} when ice is present, but can exceed 40 cm s^{-1} during the open water period. The bottom panel in each plot shows the unfiltered time series of the velocity component projected onto the principal axis of variance (listed in **Tables 11 - 16**). These indicate that the largest current speeds and variance occurs when landfast ice is absent. This seasonal scenario is repeated in all years amongst all moorings.

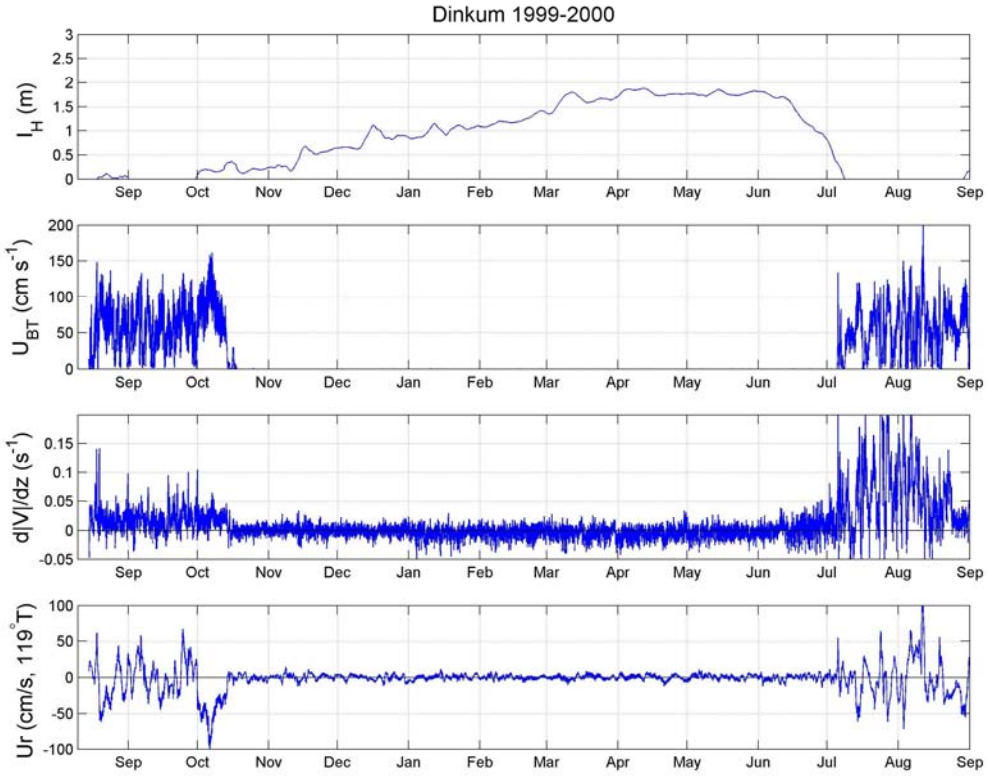

Figure 6. Time series of (from top to bottom) ice thickness, bottom track speed, shear, and velocity along the principal axis of variance at DINKUM for the first deployment period (1999 – 2000).

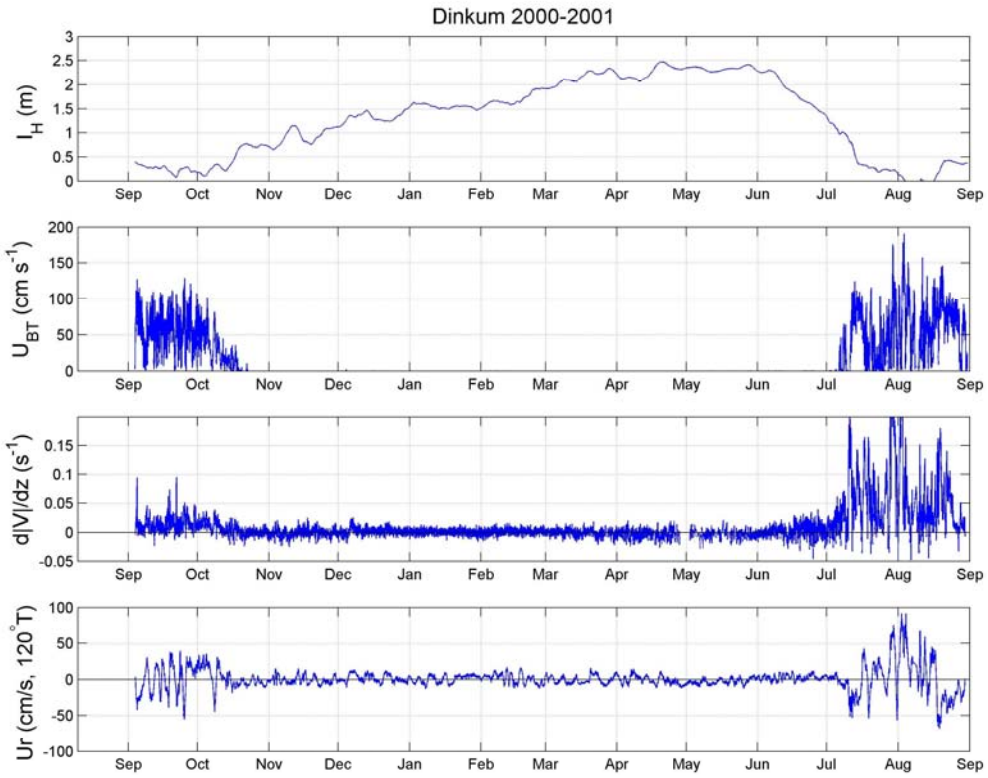

Figure 7. Time series of (from top to bottom) ice thickness, bottom track speed, shear, and velocity along the principal axis of variance at DINKUM for the second deployment period (2000 – 2001).

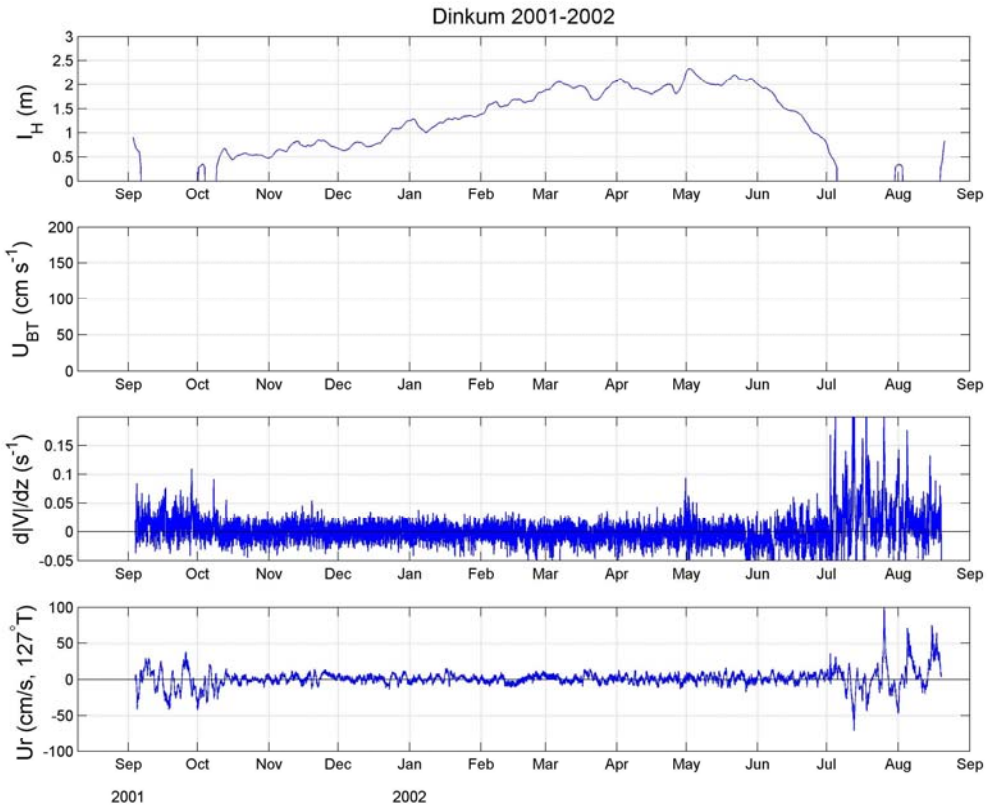

Figure 8. Time series of (from top to bottom) ice thickness, bottom track speed, shear, and velocity along the principal axis of variance at DINKUM for the third deployment period (2001 – 2002). A programming error voided measurements of the bottom track velocity.

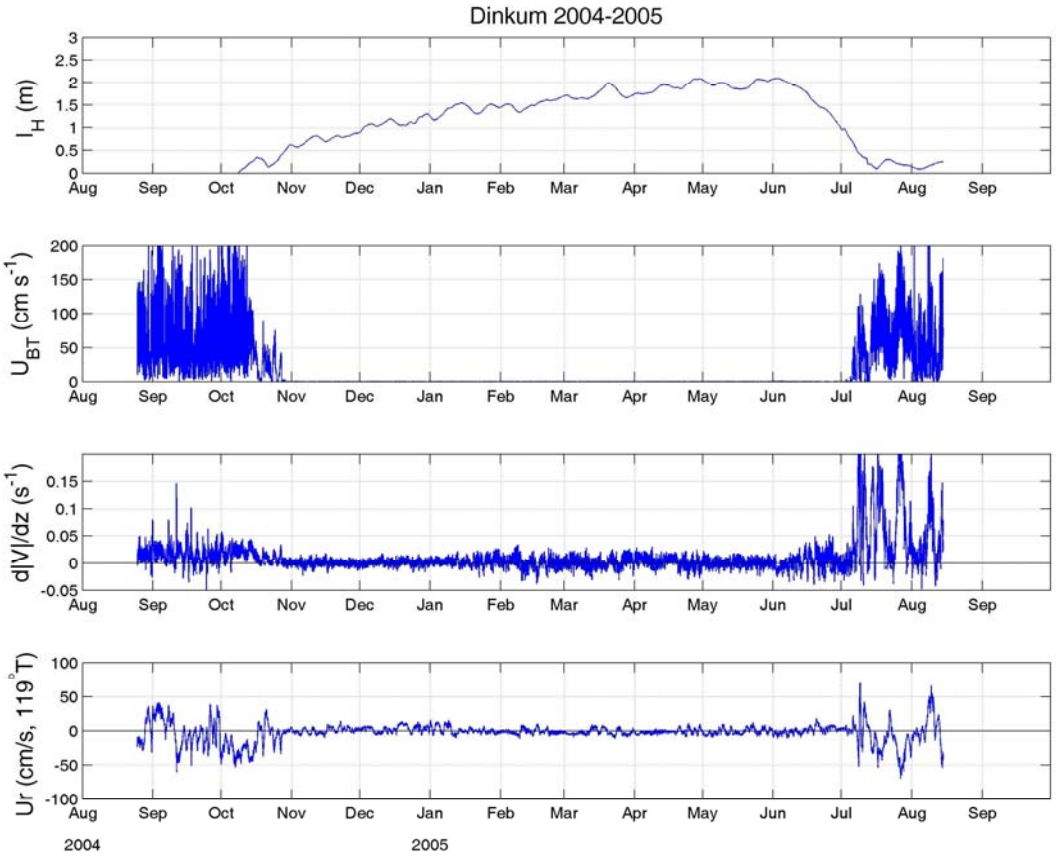

Figure 9. Time series of (from top to bottom) ice thickness, bottom track speed, shear, and velocity along the principal axis of variance at DINKUM for the fourth deployment period (2004 – 2005).

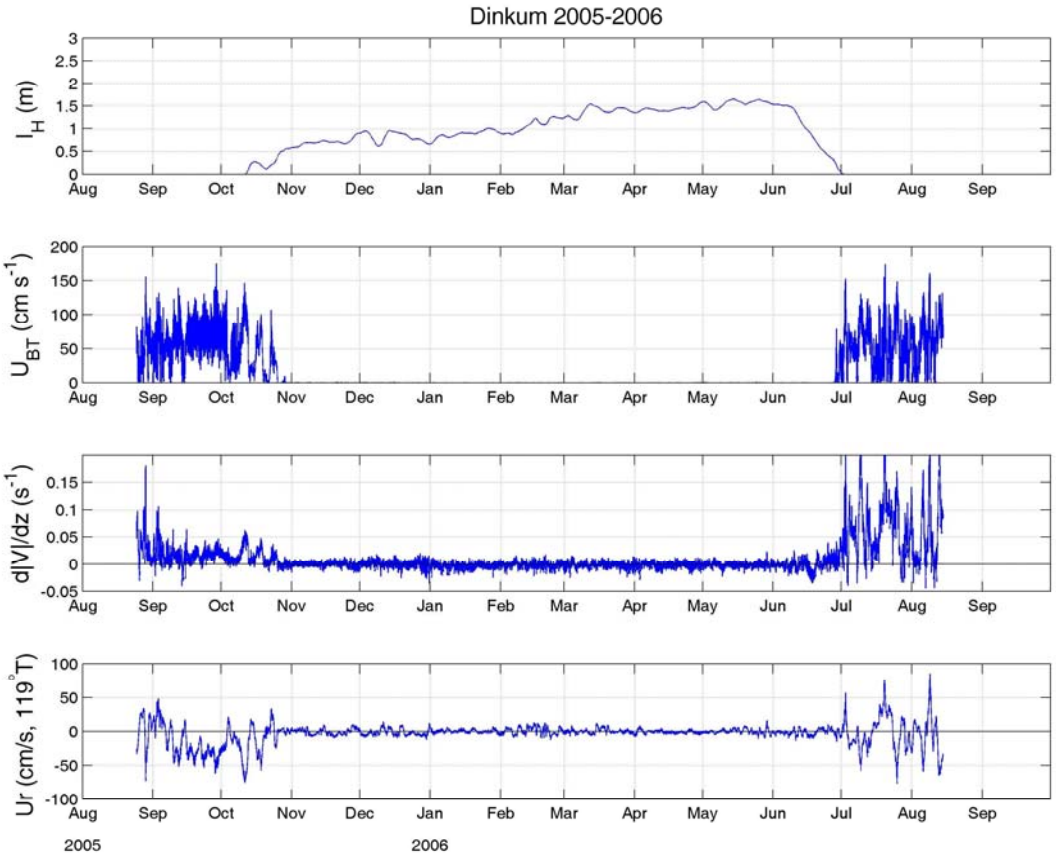

Figure 10. Time series of (from top to bottom) ice thickness, bottom track speed, shear, and velocity along the principal axis of variance at DINKUM for the fifth deployment period (2005 – 2006).

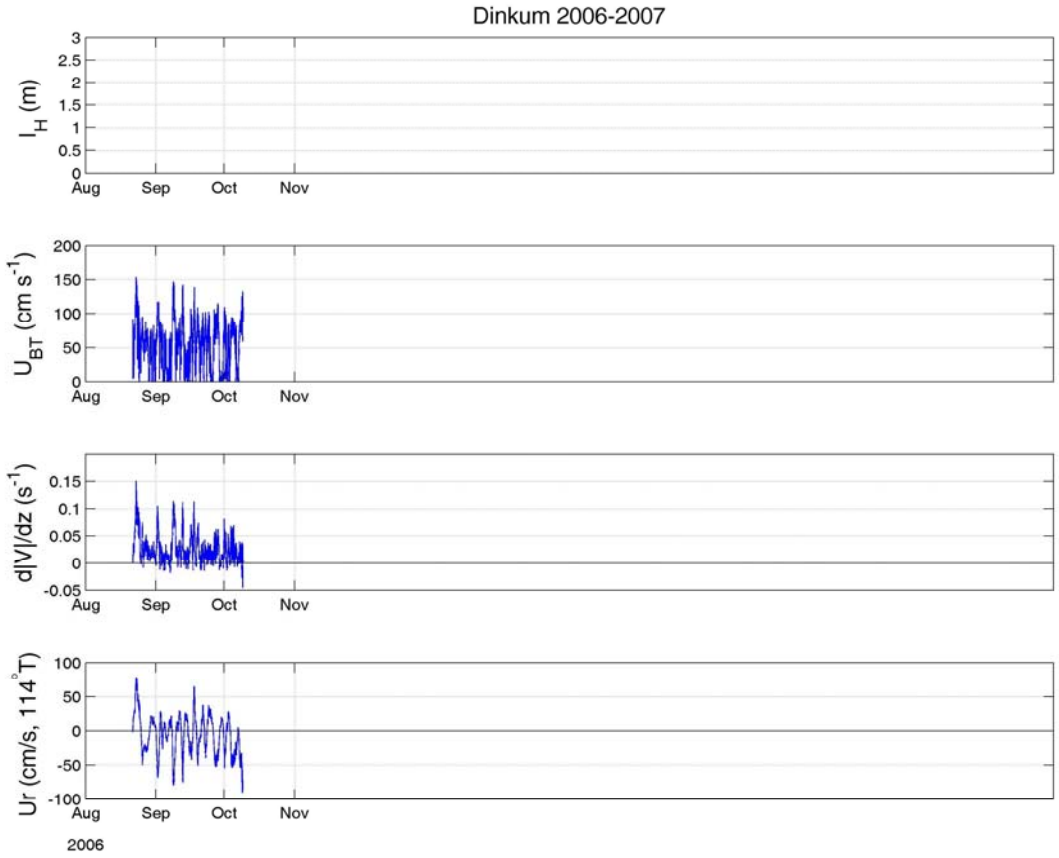

Figure 11. Time series of (from top to bottom) ice thickness, bottom track speed, shear, and velocity along the principal axis of variance at DINKUM for the sixth deployment period (2006-2007). The mooring was damaged by a storm in October 2006 that resulted in a truncated current velocity record.

Tables 7 and 8 lists the dates of landfast ice set-up and break-up for each year and mooring based on analysis of the ADCP data sets. The 5-year long DINKUM record provides the best estimate of the range in dates over which landfast ice setup and breakup occurs. Setup varied from as early as October 13th in 2001 and as late as October 27 in 2004. Breakup varied from June 23rd (2002) to July 5th (2005). Along shore variations in the timing of these events are

Table 7. Landfast ice set-up and breakup dates and times for each year and mooring, Phase I.

Phase I Landfast Ice Setup Date												
	Argo			***Dinkum***			***McClure***			***Reindeer***		
Year	1999	2000	2001	1999	2000	2001	1999	2000	2001	1999	2000	2001
Month	10	10	10	10	10	10	10	10				10
Day	15	20	13	15	22	13	15	22				10
Hour	0	3	12	0	16	10	0	16				15

Phase I Landfast Ice Breakup Date												
	Argo			***Dinkum***			***McClure***			***Reindeer***		
Year	2000	2001	2002	2000	2001	2002	2000	2001	2002	2000	2001	2002
Month	6	7	6	6	7	6	6	7				6
Day	30	4	30	30	2	23	30	2				27
Hour	23	18	1	23	5	23	23	0				14

Table 8. Landfast ice set-up and breakup dates and times for each year and mooring, Phase II.

Phase II Landfast Ice Setup Date												
	Dinkum			***Camden***			***Smith***			***Cross***		
Year	2004	2005	2006	2004	2005	2006	2004	2005	2006	2004	2005	2006
Month	10	10		10	10	10	10					11
Day	27	25		29	25	31	27					22
Hour	14	18		21	18	4	17					6

Phase II Landfast Ice Breakup Date												
	Dinkum			***Camden***			***Smith***			***Cross***		
Year	2005	2006	2007	2005	2006	2007	2005	2006	2007	2005	2006	2007
Month	7	6		7	6	6	7					7
Day	5	28		6	27	28	5					3
Hour	10	0		23	23	9	5					8

Landfast Ice Breakout Notes: Breakout events occurred at: 1) Smith Bay between 12/27/2004-1/10/2005; 2) Camden Bay 11/4/2005-11/6/2006; 3) Camden Bay 11/5/2006-11/8/2006; 4) Cross 12/1/2006-12/10/2006. The Smith Bay breakout was a mid-winter event, which dynamically may be different than the other events that occurred within 2 weeks of landfast ice setup.

small, thus the breakup and setup dates amongst CAMDEN, DINKUM, and SMITH are all within a few days of one another. For mooring CROSS the setup occurred in late November but this late date reflects the offshore development of the landfast ice, which setup inshore in late October (as evident in Synthetic Aperture Radar [SAR] images which are not shown).

Figures 12 - 27 are time series of the low-pass filtered (35-hr cutoff) major and minor velocity components, demeaned (over the deployment period) sea-level, and the wind stress components based on Deadhorse winds for each mooring. These are presented separately for each mooring for the landfast ice (**Figures 12 – 19**) and open water (**Figures 20 – 27)** seasons. Visual inspection suggests that the current components along the principal axes are highly correlated with one another during Phase I when the moorings were confined to Stefansson Sound and this is confirmed through empirical orthogonal function (EOF) analysis (based on the correlation matrix) whether calculated over the whole record or separately for each season. The results for each Phase are given in **Tables 9 and 10.** For Phase I the first mode accounts for ~90% of the variance, while the higher modes are not significant based on *North et al.*'s [1982] criterion. The dominance of the first EOF implies that flow variations in this region are coherent over spatial scales of at least 30 km so that a single mooring could be used to capture the local along-shore flow variability. Although this finding is not surprising given the simple bathymetry of the area, it was not clear at the outset of the study that these scales should hold in the presence of landfast ice because complex underice topography could generate velocity variability over small horizontal scales and thus degrade spatial coherence. Indeed the reduction in the variance explained by the first EOF mode during the 1999-2000 landfast ice season relative to later years could be due to differences in underice topography, although we have no means to examine this possibility. The EOF results in Phase 2 are quite different between the landfast and open water

seasons (**Table 10**). In Phase II, the first mode accounts for 82% of the variance during the open water season, but only 50% of the variance when landfast ice is present. Although we will return to this point later, the results suggest that alongshore de-correlation scales for velocity are substantially smaller (although larger than 30 km) when landfast ice is present.

Table 9. Percent variance explained by the first empirical orthogonal function for velocities projected along the principal axis of variance for moorings close by to Prudhoe Bay.

Period Analyzed	1999-2000	2000-2001	2001 – 2002
Landfast	77	90	94
Open Water	93	94	93
Whole Record	95	93	93

Table 10. Percent variance explained by the first empirical orthogonal function for velocities projected along the principal axis of variance for moorings separated by great distances in the along-shore direction.

Period Analyzed	2004-2005 Dinkum:Smith:Camden
Landfast	50
Open Water	82
Whole Record	79

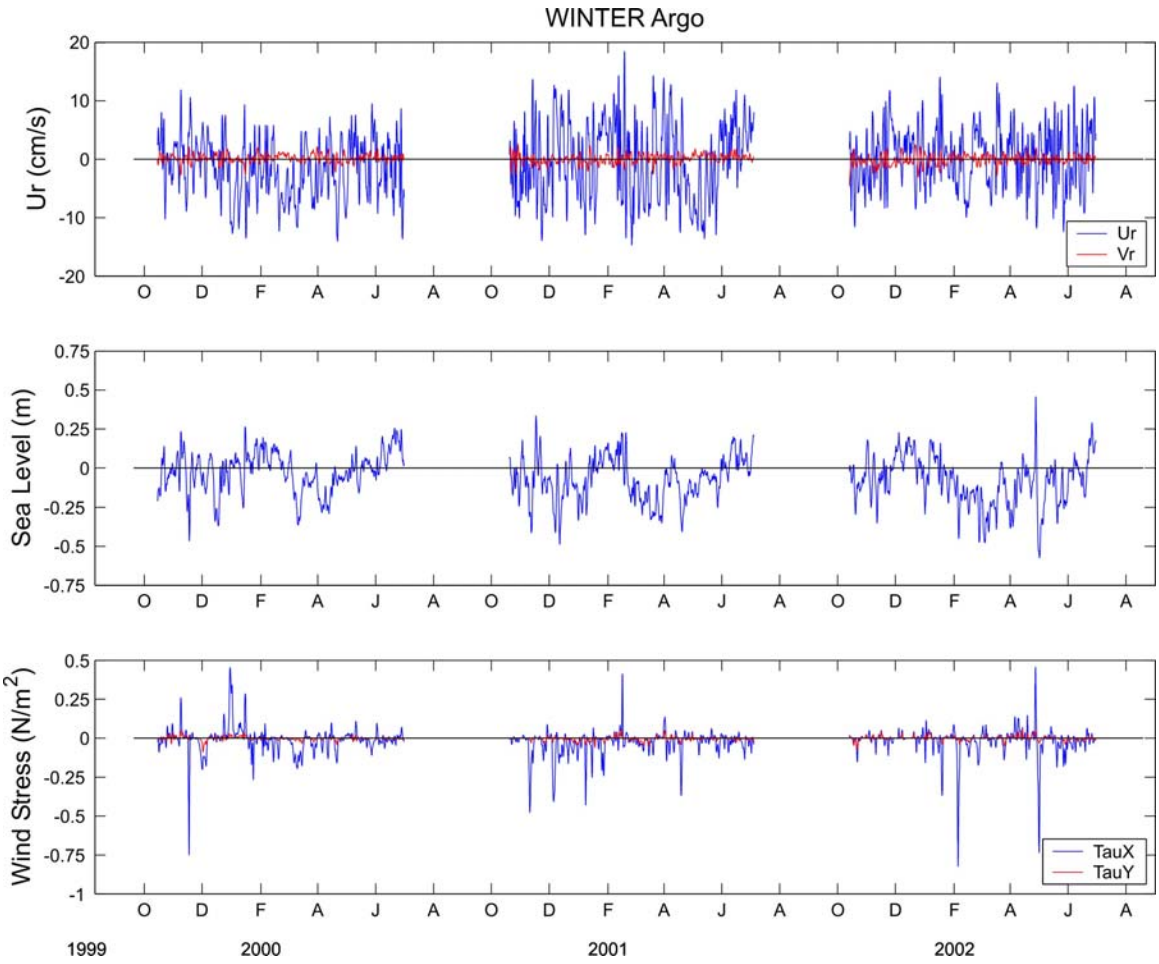

Figure 12. Time series of currents, demeaned sea level, and along- and cross-shore component of wind stress at ARGO for all landfast ice periods.

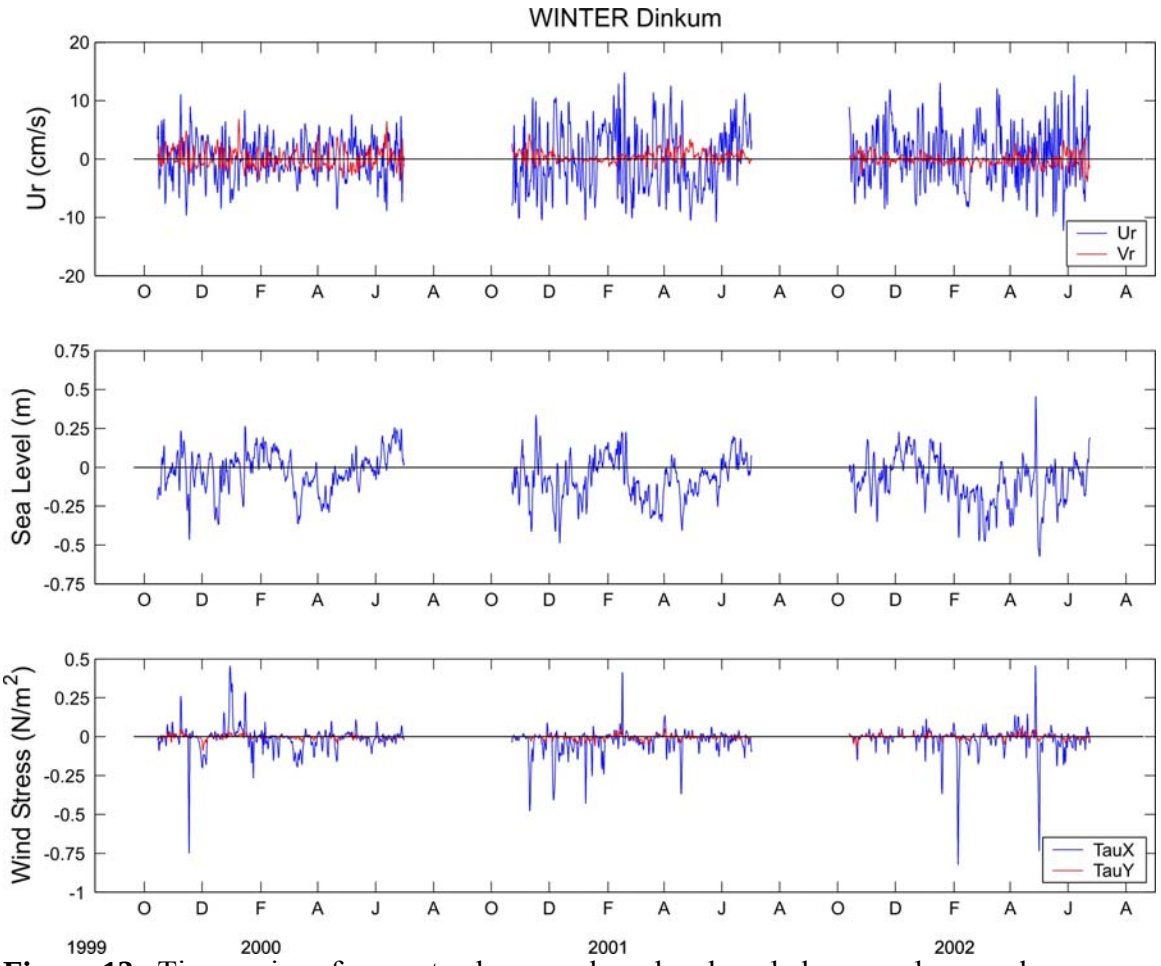

Figure 13. Time series of currents, demeaned sea level, and along- and cross-shore component of wind stress at DINKUM for all landfast ice periods between 1999 and 2002.

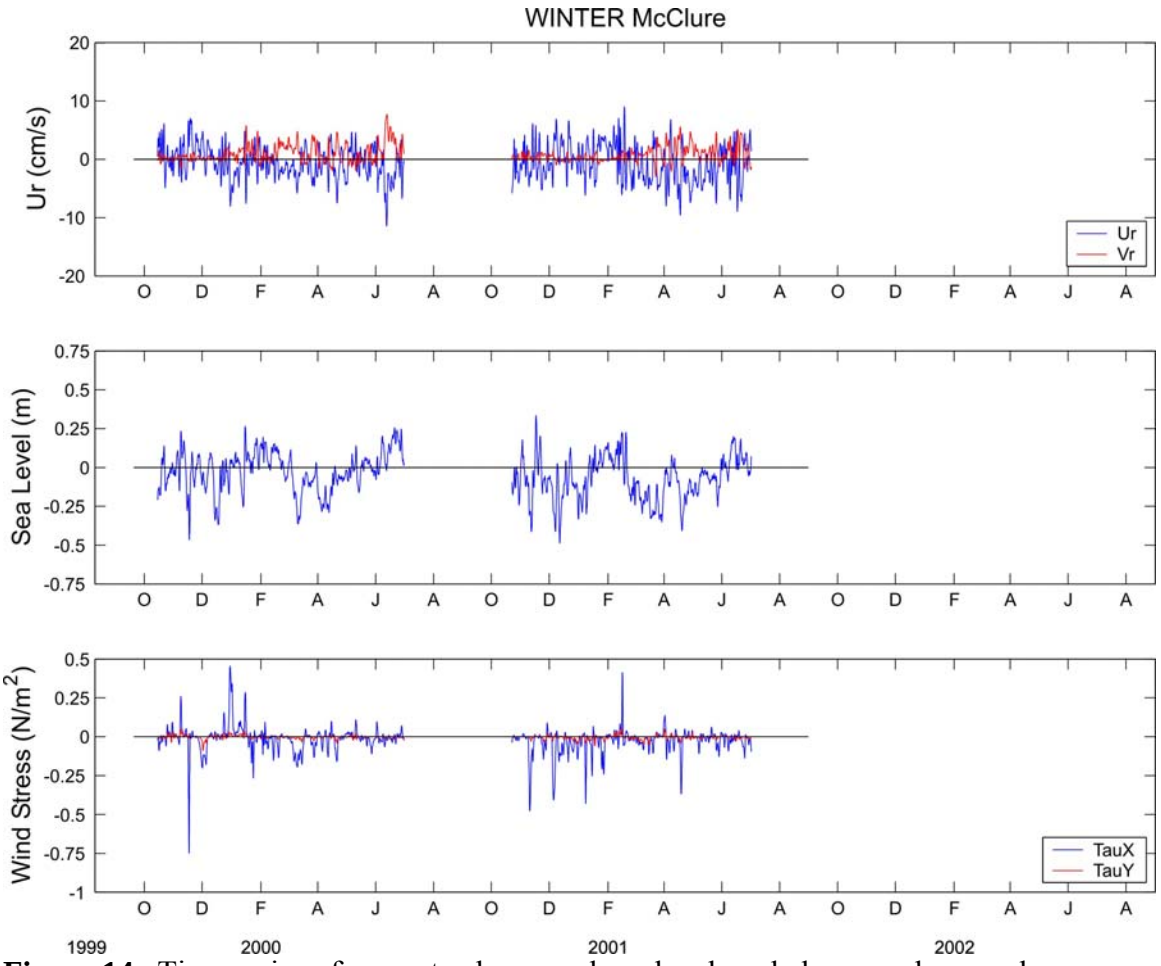

Figure 14. Time series of currents, demeaned sea level, and along- and cross-shore component of wind stress at McCLURE for the 1999-2000 and 2000 – 2001 landfast ice periods.

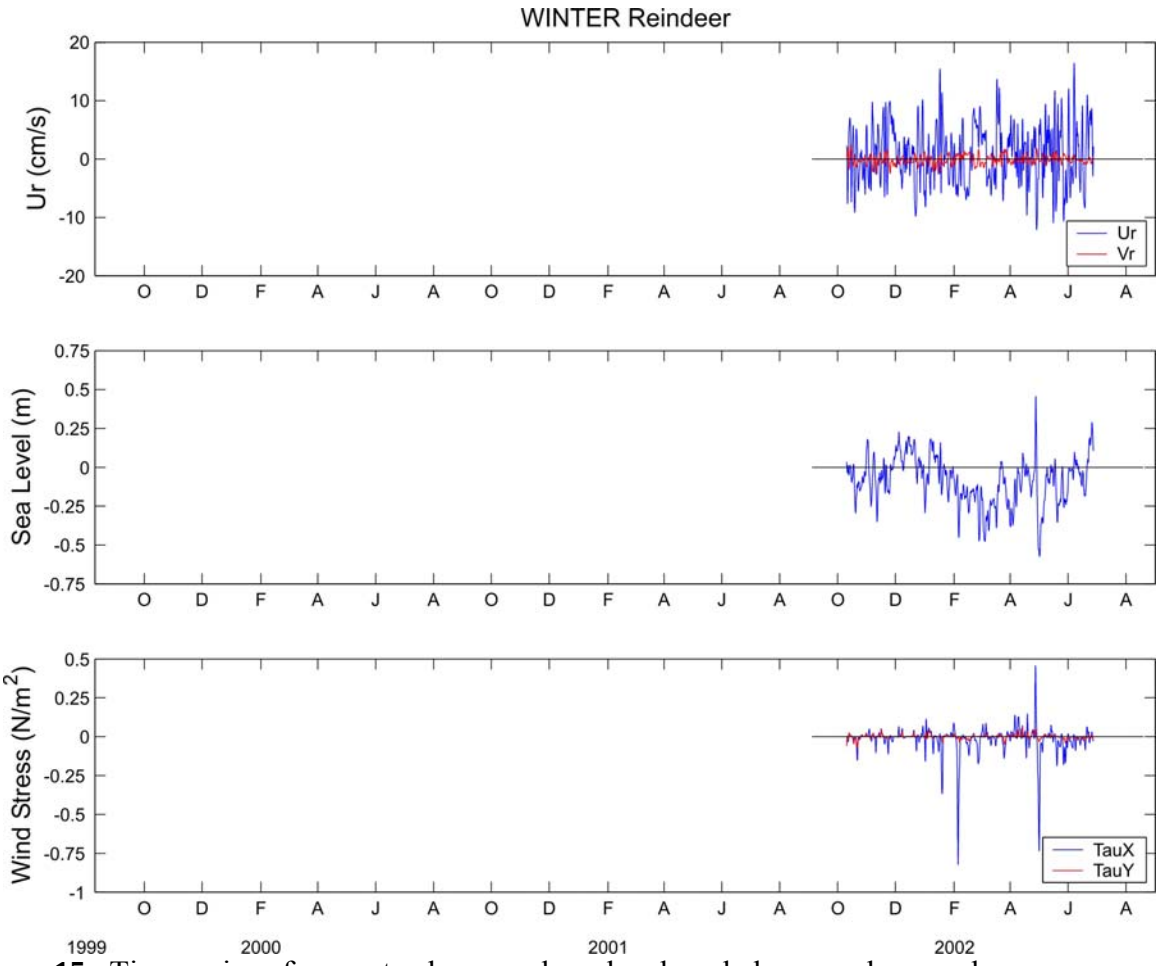

Figure 15. Time series of currents, demeaned sea level, and along- and cross-shore component of wind stress at REINDEER for the 2001 – 2002 landfast ice period

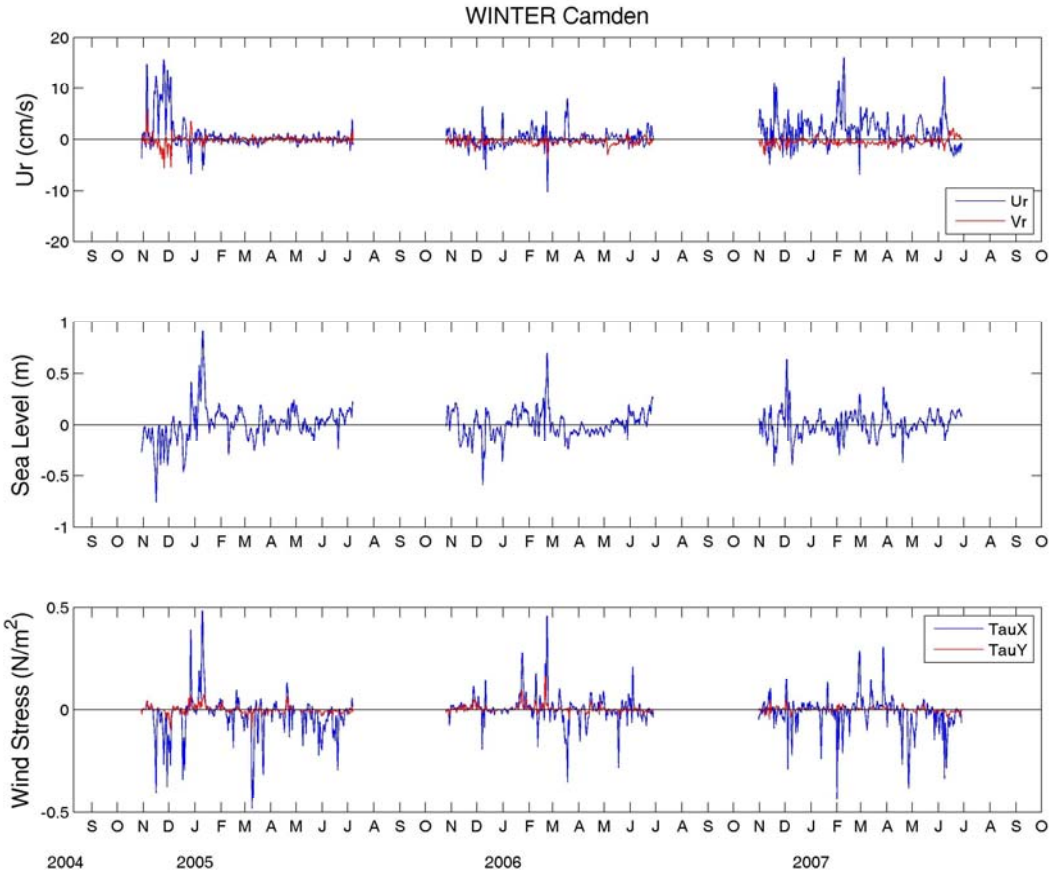

Figure 16. Time series of currents, demeaned sea level, and along- and cross-shore component of wind stress at CAMDEN for the 2004 – 2007 landfast ice periods.

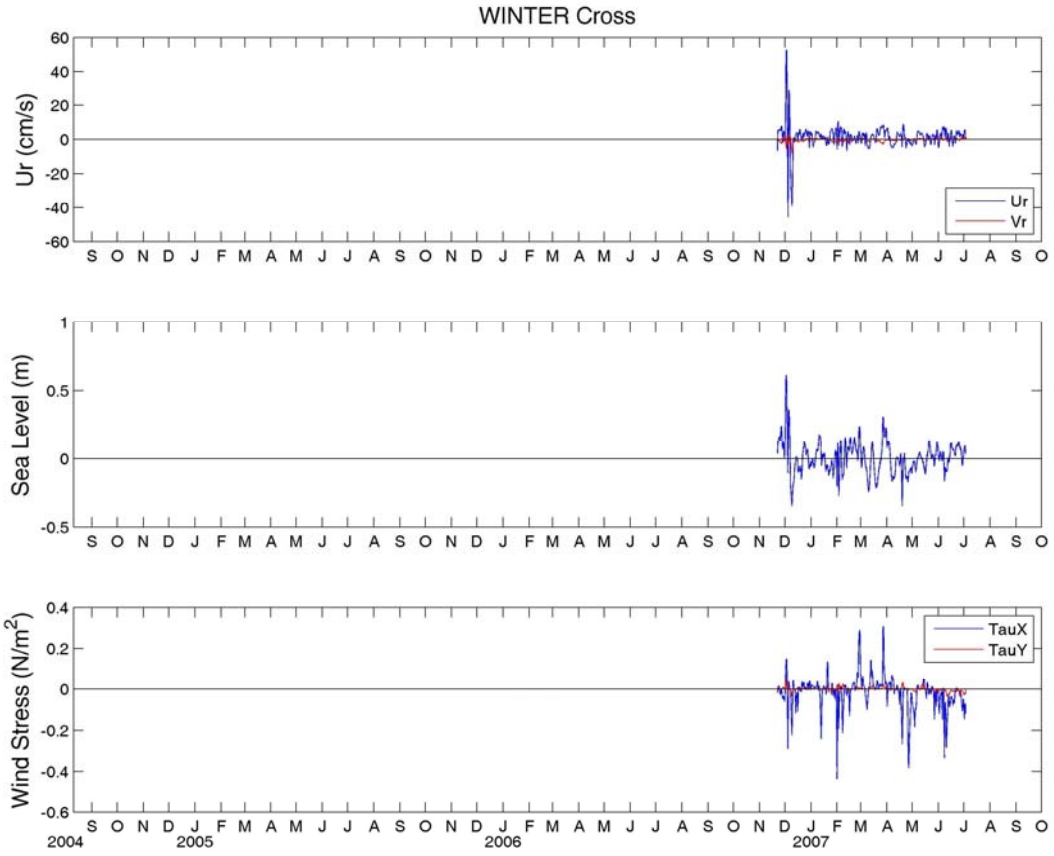

Figure 17. Time series of currents, demeaned sea level, and along- and cross-shore component of wind stress at CROSS for the 2006 – 2007 landfast ice periods.

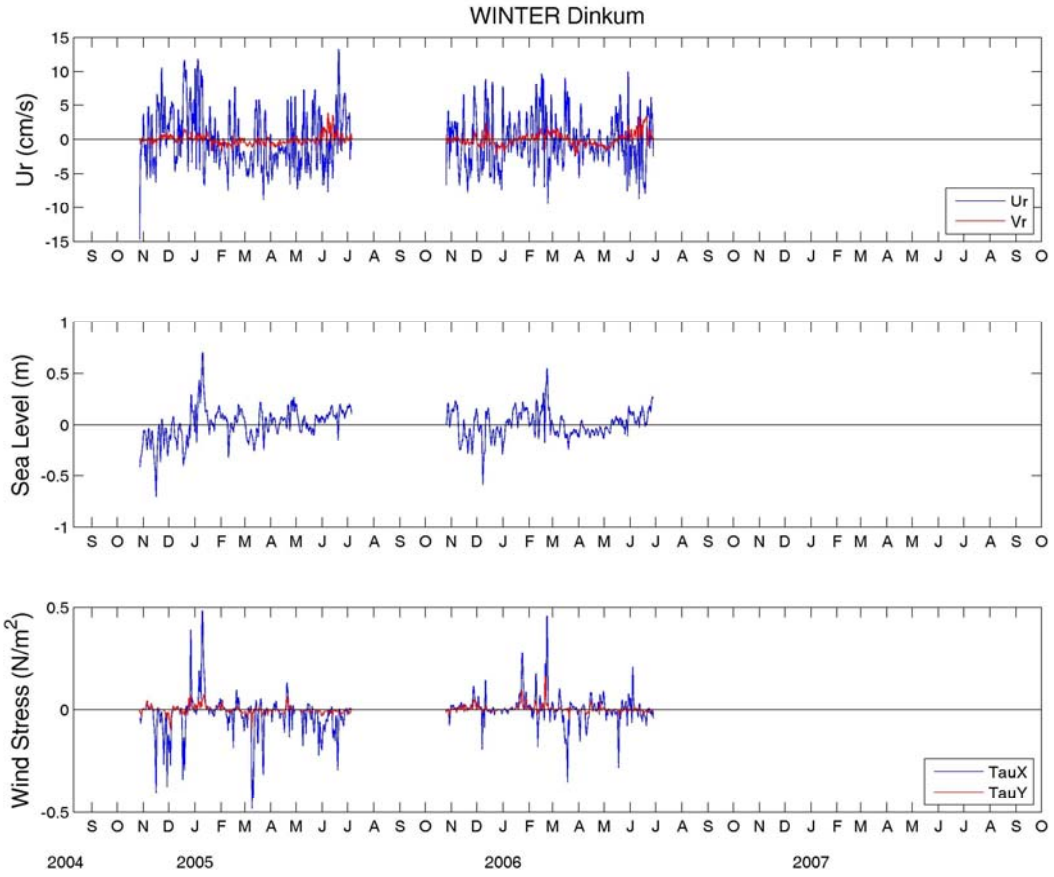

Figure 18. Time series of currents, demeaned sea level, and along- and cross-shore component of wind stress at DINKUM for the 2004-2006 landfast ice periods.

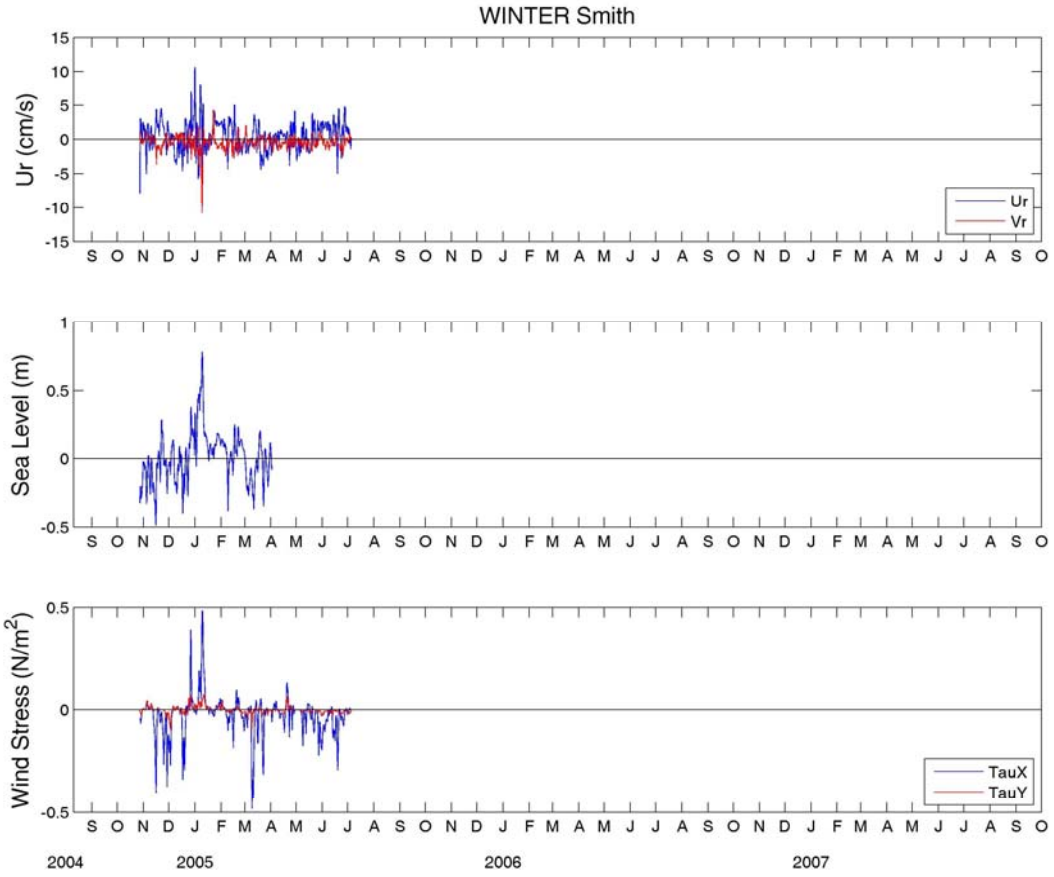

Figure 19. Time series of currents, demeaned sea level, and along- and cross-shore component of wind stress at SMITH for the 2004-2005 landfast ice period.

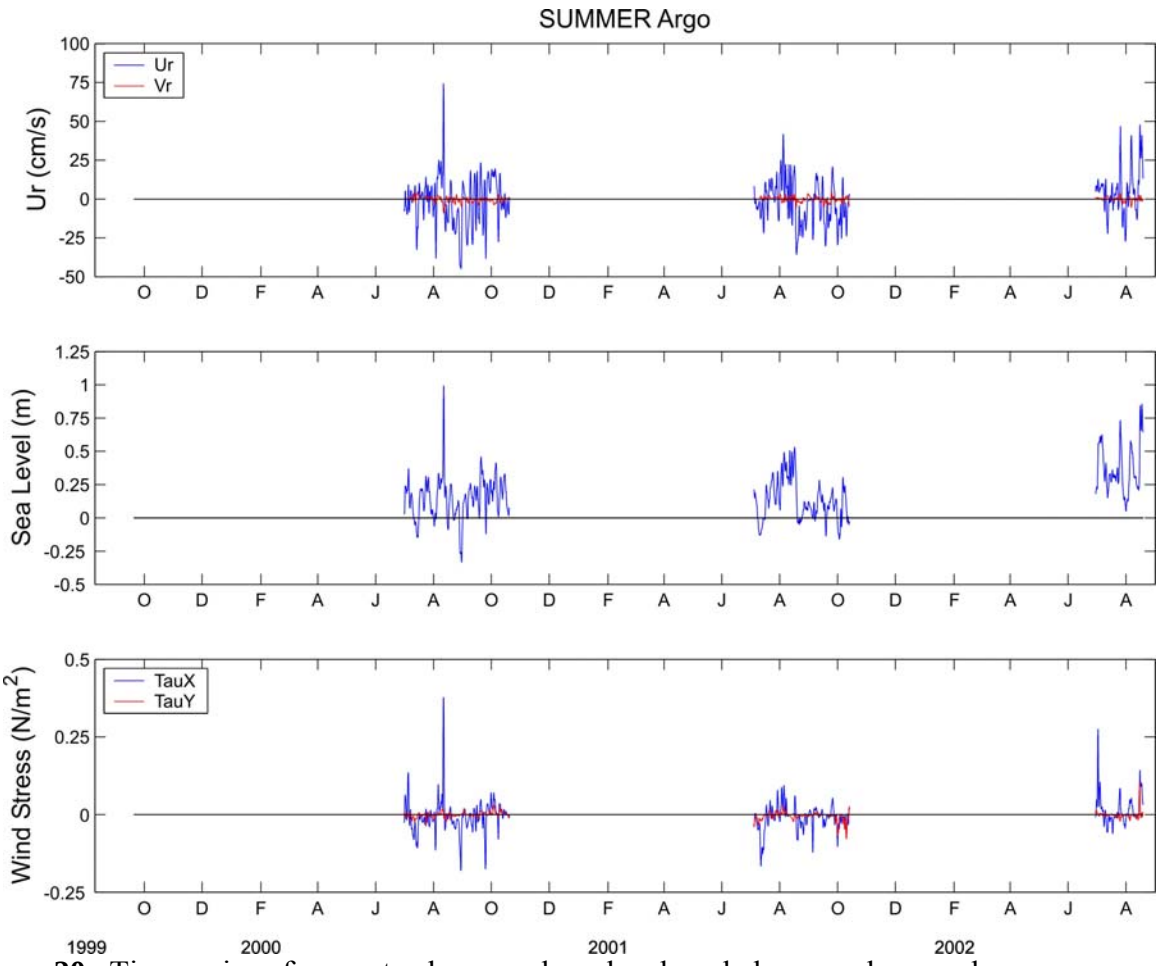

Figure 20. Time series of currents, demeaned sea level, and along- and cross-shore component of wind stress at ARGO for all open water periods.

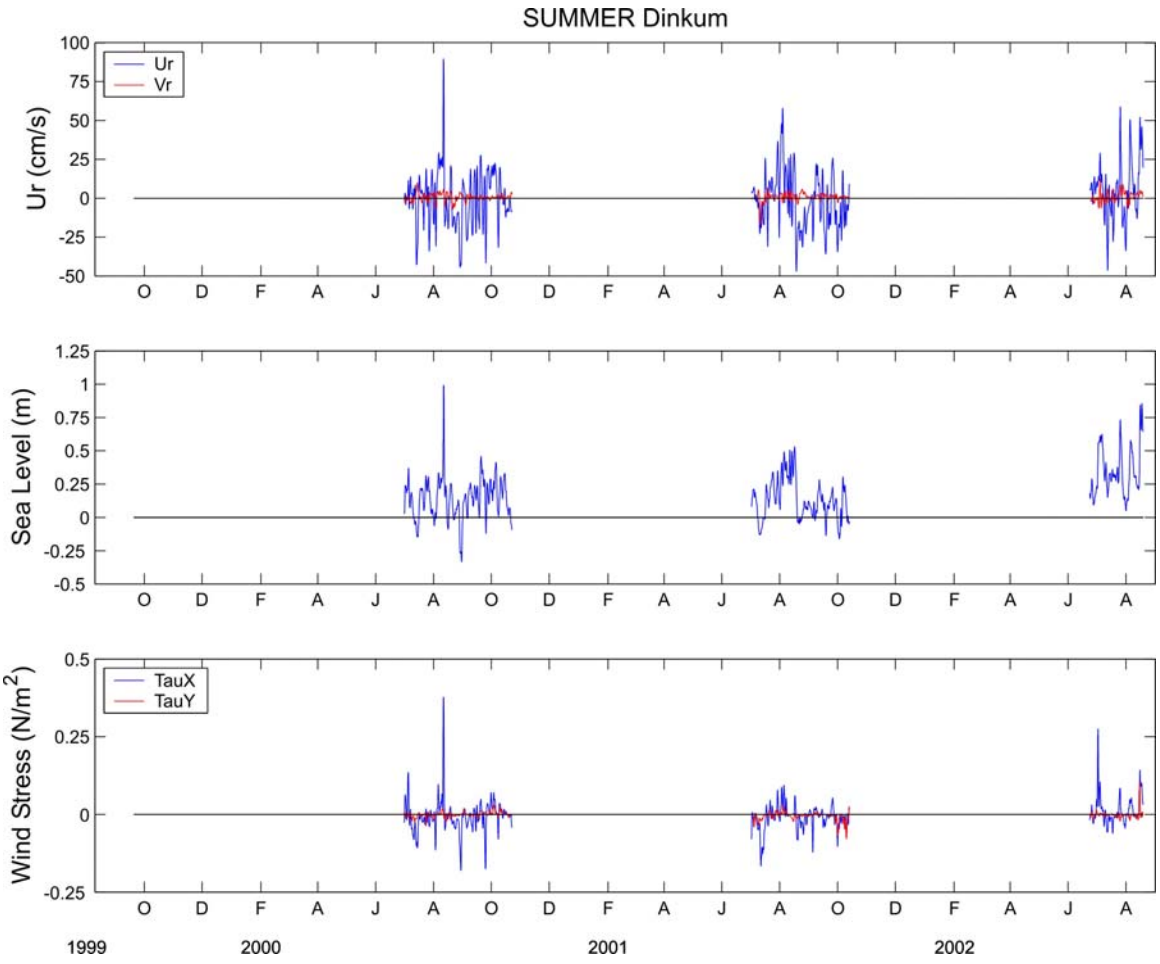

Figure 21. Time series of currents, demeaned sea level, and along- and cross-shore component of wind stress at DINKUM 1999-2002 for all open water periods.

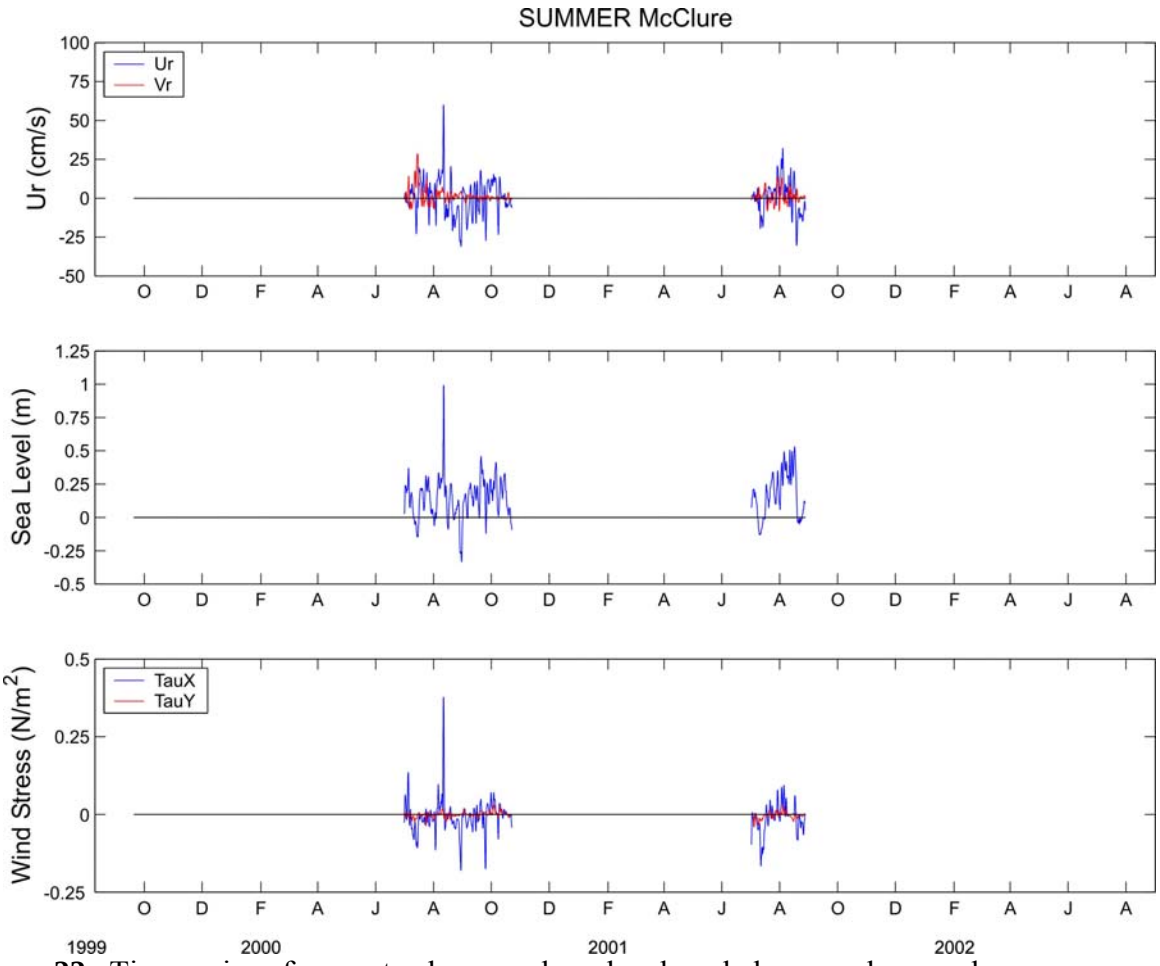

Figure 22. Time series of currents, demeaned sea level, and along- and cross-shore component of wind stress at MCCLURE for the open water periods of 2000 and 2001.

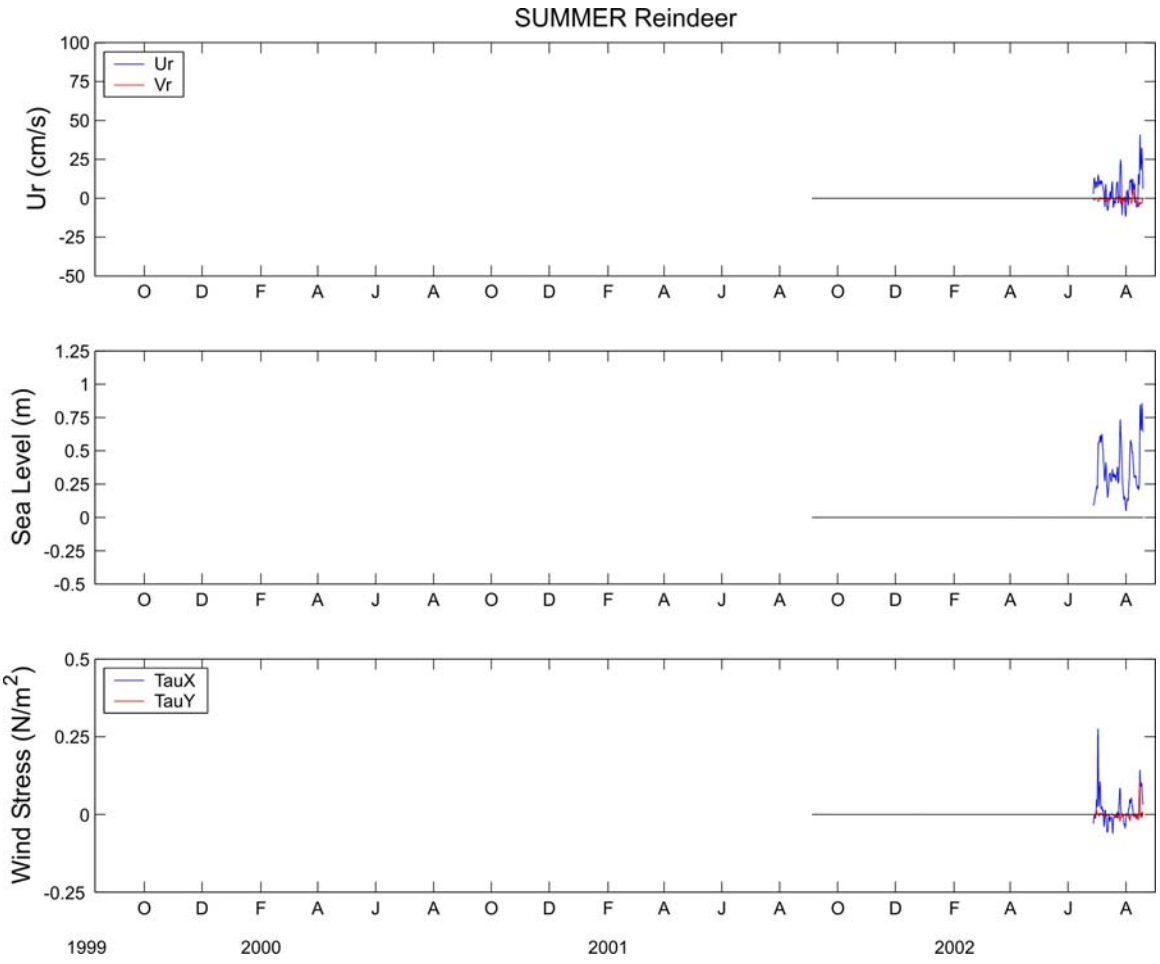

Figure 23. Time series of currents, demeaned sea level, and along- and cross-shore component of wind stress at REINDEER for the open water period of 2002.

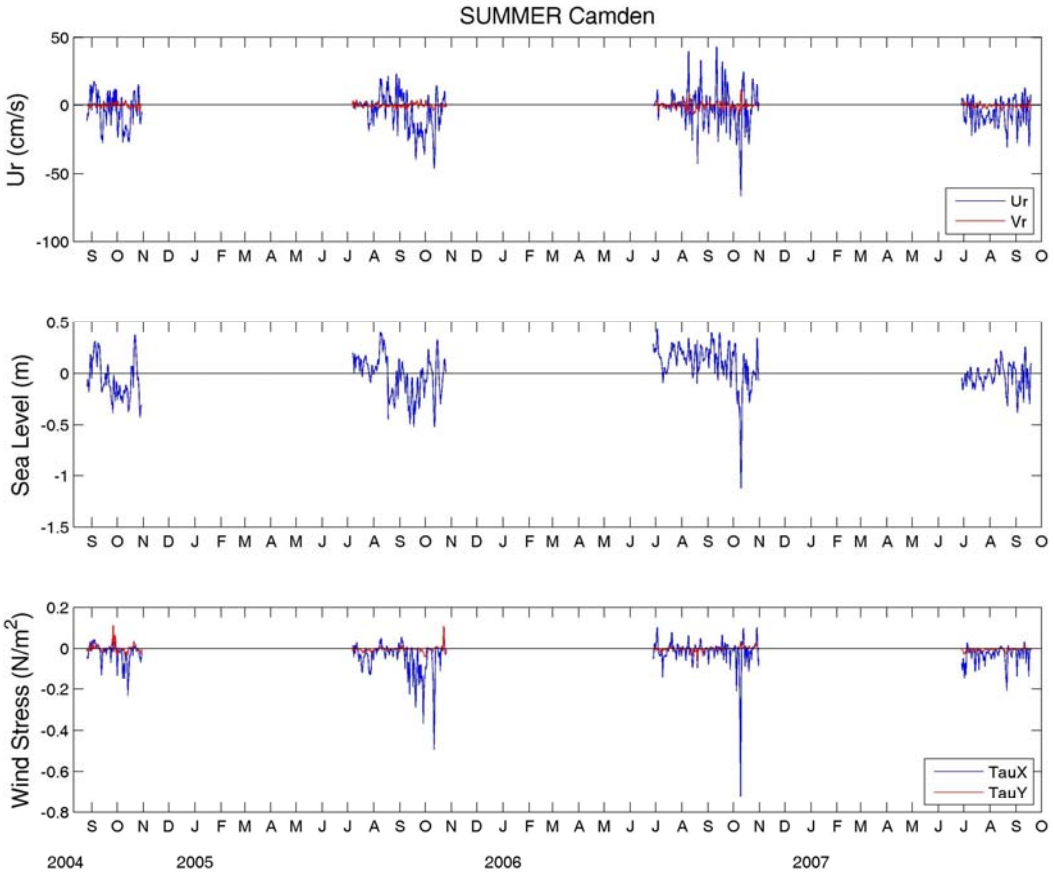

Figure 24. Time series of currents, demeaned sea level, and along- and cross-shore component of wind stress at CAMDEN for the open water periods of 2004-2007.

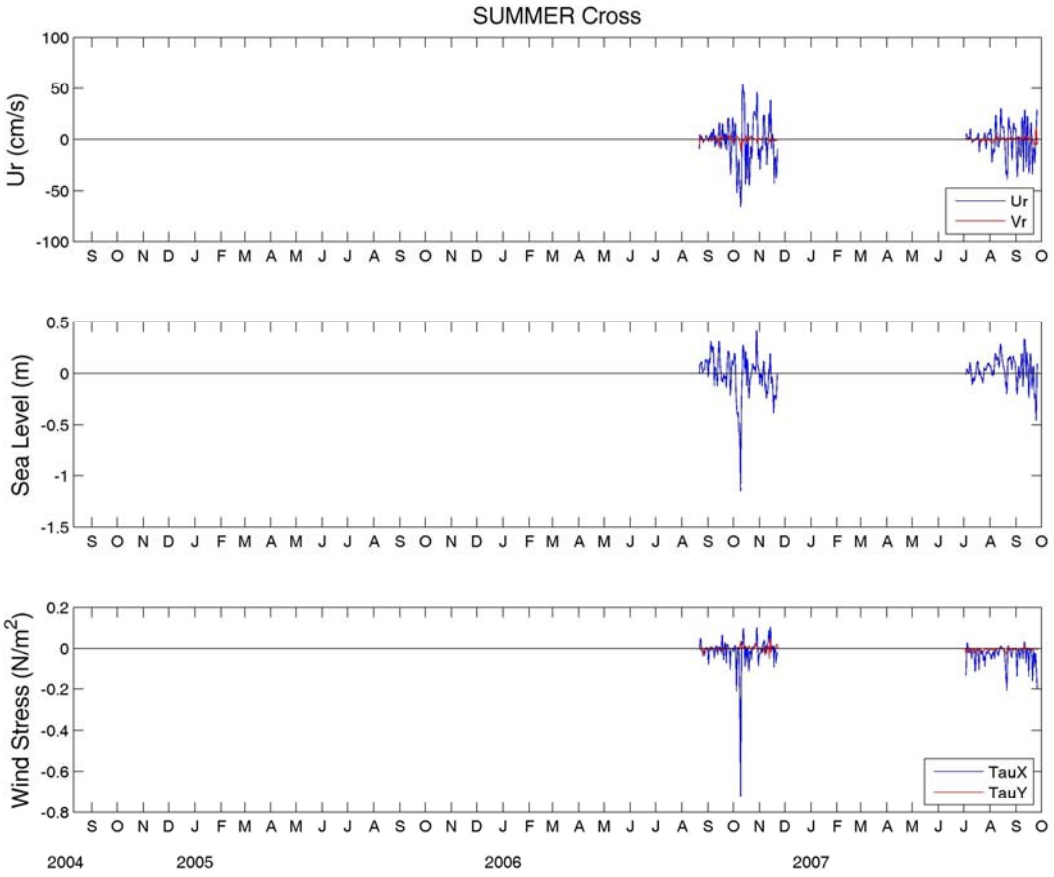

Figure 25. Time series of currents, demeaned sea level, and along- and cross-shore component of wind stress at CROSS for the open water periods of 2006 - 2007.

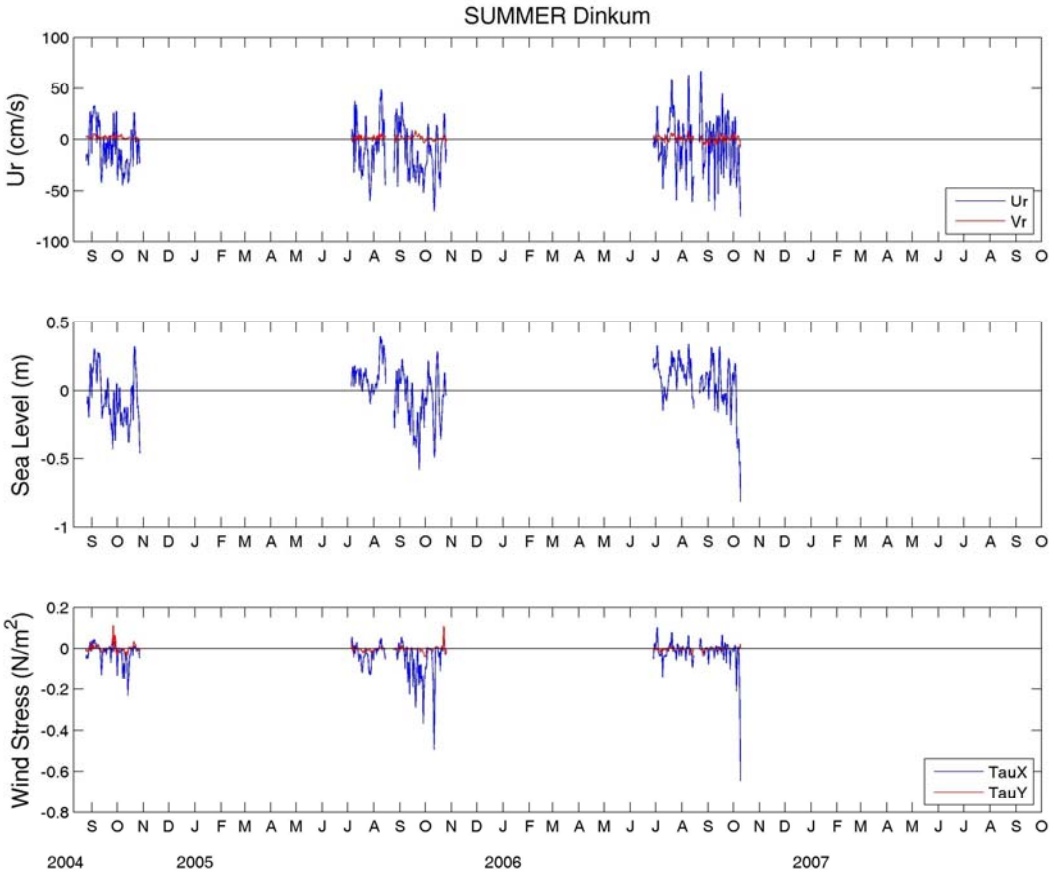

Figure 26. Time series of currents, demeaned sea level, and along- and cross-shore component of wind stress at DINKUM 2004-2007 for all open water periods.

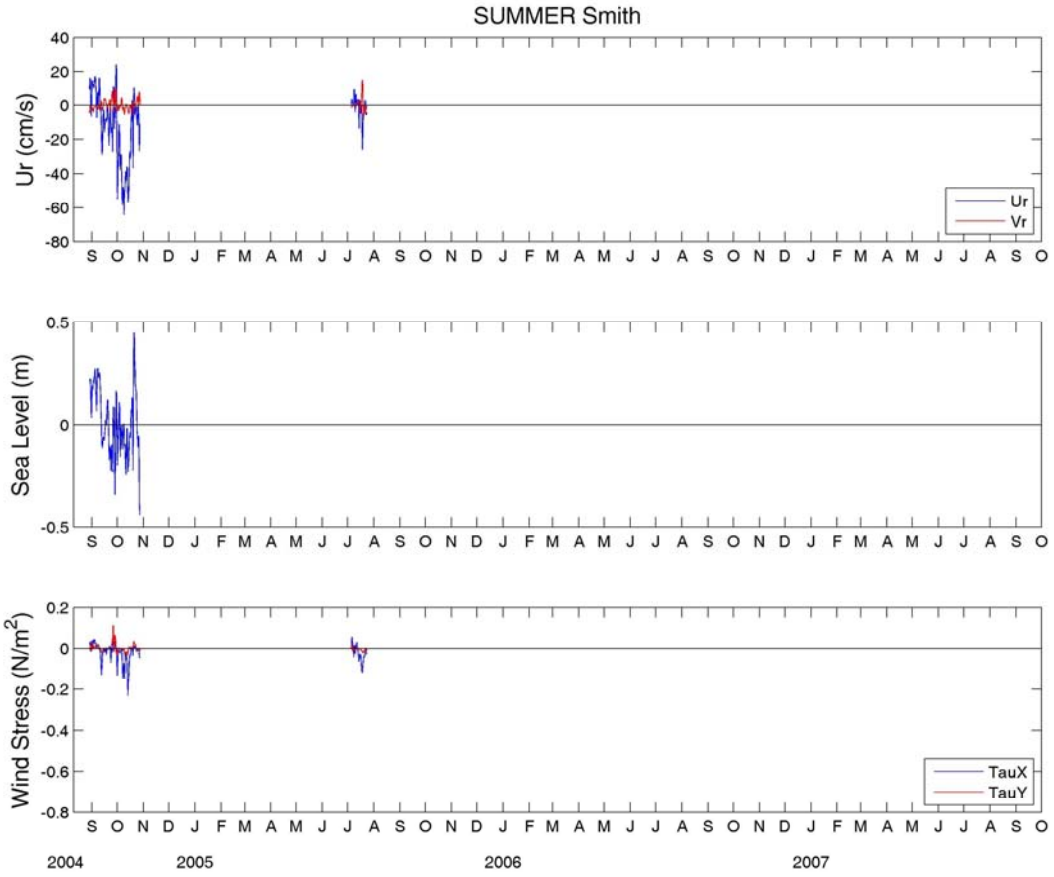

Figure 27. Time series of currents, demeaned sea level, and along- and cross-shore component of wind stress at SMITH for the open water periods of 2004-2005.

Summary statistics for the currents and winds for each year and season are listed in **Tables 11 – 16** as a function of record length and season (landfast versus open water) as defined by the ADCP parameters. The current meter data were filtered prior to computing the statistics in order to focus on the subtidal properties of the flow field. The tidal properties are discussed separately later. Statistical significance is based on 95% confidence limits (listed in the tables) using the effective number of degrees of freedom (N_{eff}), computed as $N_{eff} = N\Delta t/\tau$. Here Δt is the sampling interval, N is the number of data points in the time series, and τ is the integral time scale of the currents or winds. The integral time scale is the decay time scale for a current or wind event and is the time required to obtain a new independent observation in an auto-correlated time series.

The winds are weakly westward with record-length averages ranging from 1 – 3 m s^{-1} (depending upon deployment period) and statistically different from zero at the 95% confidence level. However, mean westward winds do not prevail throughout the year. For example, the mean wind was westward during the open water period of 1999-2000, but not significantly different from zero during the landfast ice period during that same period. In contrast in 2000-2001 and 2001-2002, mean winds were westward during the landfast ice period, but not significantly different from zero during these two open water seasons. From 2005 – 2007, open water season winds were westward (and significantly different from zero) in all years, whereas only winds during the 2004-05 landfast ice period were westward on average. The open water seasonal mean along-shelf wind, averaged over all years, is ~2 m-s^{-1} and thus smaller than the ~3.5 m-s^{-1} mean wind speed indicated for summer along the Beaufort coast in the climatology of *Brower et al.* [1988]. There is also very little difference in the wind variances among the deployment years and

between seasons. The lack of a distinct annual cycle in Deadhorse winds contrasts with the prominent annual cycle in winds based on the Barrow wind record (**Figure 2**) It also differs from winds computed over the southern Canada Basin using synoptic forecast fields [*Furey*, 1998]. He found that the winds are westward on average from fall through spring, but weakly eastward in summer. He also observed a distinct annual cycle in wind variance, especially in the zonal velocity component, with the variance being three times greater in winter than in summer. Although the data sets and time periods used in comparing these annual cycles differ, this discussion suggests that there might be a cross-shelf gradient in wind stress. Mesoscale effects could be responsible for cross-shelf shears in the wind field. For example, sea-breezes (open water season only) promote westward coastal winds with this influence limited to the innermost 25 km of the shelf according to *Kozo's* [1982b] model results. In winter, the mountain barrier effect might influence winds at Deadhorse [*Kozo*, 1984] with this phenomenon occurring when atmospheric pressure systems force cold, polar air masses southward towards the Brooks Range. *Kozo* [1984] estimated that this baroclinic effect occurs up to 20% of the time during winter. However, Kozo's estimates were based on limited observations conducted during the 1970s. The frequency in which the mountain barrier baroclinic effect occurs should vary interannually in association with year-to-year differences in the large scale atmospheric pressure field over the arctic.

For most moorings and deployment periods the mean current vectors are not significantly different from zero, and when significant, they are small with mean alongshore velocities being <3 cm-s^{-1}. In fact, the largest mean values occurred during the open water periods in 1999 when a statistically significant mean westward flow was

observed at all sites except MCCLURE. During Phase II, the mean currents were more consistently westward during the open water season only. In general, the mean currents during the landfast ice season are < 1 cm-s^{-1}, often insignificant, but when significant, do not show a consistent pattern of eastward or westward flow. Our mean values are somewhat surprising given the general belief that the mean flow is westward and downwind [*Barnes and Reimnitz*, 1974; *Wiseman et al*., 1974]. This appears to hold only for the open water season when the along-shore winds are westward and significantly different from zero.

Although the mean currents are small or negligible, the variability is large. Most of the current variance is contained in the along-shore velocity component with >~90% of the current variability associated with this principal axis. For each mooring these axes are oriented approximately parallel to the coast (e.g., northwest to southeast). Similarly, the winds blow primarily alongshore such that >85% of the wind variance is aligned along the east-west axis. As evident in the current time series in the lowest panels of **Figures 6 - 11**, the current velocity variance changes seasonally, with the variance during the landfast ice period being roughly an order of magnitude smaller than the variance of the open water season. Along-shore current variances do not change significantly throughout the landfast ice season. This contrasts with findings on the Chukchi Sea shelf [*Aagaard and Roach*, 1990; *Weingartner et al*., 1998; *Weingartner et al.,* 2005] where current variance is generally much higher from November through January than from February through April.

Table 11. Current and wind statistics 1999 – 2000. The direction toward which the mean velocity vector points is Θ_M. For the principal axis, % refers to the percentage of the velocity variance accounted for by the component projected onto the axis with orientation Θ_P. The mean north-south <V> and east-west <U> velocity components and ± the 95% confidence limits are listed. The latter are computed using N_{eff} based on the integral time scale (τ) determined from the first zero crossing of the autocorrelation function. Values significantly different from zero are italicized. The variances (s^2) of the V and U are given along with the ratio of the subtidal variance to the total variance, which is the variance of the filtered data divided by the variance of the unfiltered (which includes the semi-diurnal and diurnal tides) data.

Mooring	**Mean Velocity**		**Principal Axis**								
	Speed (cm s^{-1})	Θ_M	%	Θ_P	Max Speed (cm s^{-1})	τ (days)	<V> (cm s^{-1})	s^2_V	<U> (cm s^{-1})	s^2_U	$\frac{s^2_{subtidal}}{s^2_{total}}$
Full Record											
Argo	3.4	277	99	96	111	4.5	*0.4 ± 0.3*	4	*-3.4 ± 2.0*	172	0.87
Dinkum	2	307	98	119	110	4	1 ± 1	49	*-2 ± 1.4*	155	0.88
McClure	2.2	3	92	151	68	5.5	*2.2 ± 1.6*	87	0.1 ± 1.0	34	0.84
Winds (m s^{-1})	1.3	250	90	77	25	3	*-0.5 ± 0.3*	6	*-1.3 ± 1.1*	36	-
Landfast Ice Period											
Argo	1.6	283	98	99	24	2.5	*0.4 ± 0.1*	1	*-1.6 ± 0.7*	23	0.71
Dinkum	0	-	94	141	20	2	0 ± 0.3	8	0 ± 0.3	54	0.54
McClure	1.1	29	89	176	14	3	*1 ± 0.6*	9	*0.6 ± 0.2*	1	0.43
Winds (m s^{-1})	0.8	249	91	75	25	3.5	-0.3 ± 0.4	6	-0.8 ± 1.3	34	-
Open Water Period											
Argo	7.3	273	99	96	111	4.5	0.4 ± 0.8	5	*-7.3 ± 5.9*	205	0.90
Dinkum	6	306	99	117	110	4	*4 ± 1.4*	126	*-5 ± 3.0*	454	0.91
McClure	4.8	350	93	149	68	5.5	*4.7 ± 4.6*	244	-0.8 ± 2.9	102	0.88
Winds (m s^{-1})	2.8	251	89	83	20	3	*-0.9 ± 0.4*	5	*-2.6 ± 2.1*	39	-

Table 12. Current and wind statistics 2000 - 2001.

Mooring	**Mean Velocity**		**Principal Axis**								
	Speed (cm s^{-1})	Θ_M	%	Θ_P	Max Speed (cm s^{-1})	τ (days)	<V> (cm s^{-1})	s^2_V	<U> (cm s^{-1})	s^2_U	$\frac{s^2_{subtidal}}{s^2_{total}}$
Full Record											
Argo	0.4	277	99	98	51	4	0.0 ± 0.2	3	-0.4 ± 1.4	89	0.83
Dinkum	0.5	50	98	120	58	4.5	0.3 ± 1	30	0.4 ± 1.0	85	0.83
McClure	0.8	11	81	136	60	4.5	*0.8 ± 0.7*	24	0.2 ± 0.8	23	0.71
Winds (m s^{-1})	2.0	250	87	74	24	2.5	*-0.7 ±0.2*	6	*-1.9 ± 0.8*	27	
Landfast Ice Period											
Argo	0.2	303	99	98	22	3	0.1 ± 0.3	2	-0.2 ± 1.4	42	0.81
Dinkum	0.5	47	98	125	15	5	0.3 ± 1	10	0.3 ± 1.0	19	0.74
McClure	1.0	4	94	154	11	4	*1.0 ± 0.8*	9	0.1 ± 0.3	3	0.52
Winds (m s^{-1})	-2.6	250	88	73	24	1	*-0.9 ± 0.4*	6	*-2.5 ± 1.5*	27	-
Open Water Period											
Argo	0.9	261	99	97	51	4	-0.1 ± 0.5	5	-0.9 ± 4.0	205	0.84
Dinkum	1	57	98	119	58	4.5	0.4 ± 1.5	78	0.6 ± 4.5	242	0.85
McClure	0.5	43	80	131	60	3.5	0.4 ± 1.9	60	0.4 ± 2.5	71	0.78
Winds (m s^{-1})	0.9	249	84	76	17	2.5	-0.3 ± 0.6	6	-0.8 ± 1.3	24	-

Table 13. Current and wind statistics 2001 - 2002.

Mooring	**Mean Velocity**		**Principal Axis**								
	Speed (cm s^{-1})	Θ_M	%	Θ_P	Max Speed (cm s^{-1})	τ (days)	<V> (cm s^{-1})	s^2_V	<U> (cm s^{-1})	s^2_U	$\frac{s^2_{subtidal}}{s^2_{total}}$
Full Record											
Argo	0.4	115	98	101	71	2.5	-0.2 ± 0.2	4	0.4 ± 1.0	70	0.82
Dinkum	0.9	115	97	126	102	3	-0.4 ± 0.7	39	0.8 ± 1.0	70	0.82
Reindeer	1	120	96	104	79	3	*-0.7 ± 0.3*	4	*1.2 ± 0.7*	41	0.79
Winds (m s^{-1})	0.8	245	85	73	25	1.5	-0.3 ± 0.3	7	*-0.7 ± 0.6*	26	-
Landfast Ice Period											
Argo	0.4	110	98	106	23	2.5	-0.1 ± 0.2	3	0.3 ± 0.6	22	0.71
Dinkum	0.7	136	97	132	14	2	*-0.5 ± 0.3*	10	*0.5 ± 0.4*	12	0.63
Reindeer	0.9	112	98	109	20	2	*-0.3 ± 0.2*	3	*0.8 ± 0.5*	22	0.77
Winds (m s^{-1})	0.9	268	88	72	25	1.5	0.0 ± 0.4	7	*-0.9 ± 0.8*	29	-
Open Water Period											
Argo	0.6	124	99	100	71	2.5	-0.3 ± 0.6	9	0.5 ± 3.6	207	0.87
Dinkum	1.6	90	98	125	102	3	0.0 ± 2.5	113	1.6 ± 3.6	220	0.86
Reindeer	2.7	127	95	99	79	2.5	*-1.6 ± 0.6*	7	2.2 ± 2.2	95	0.78
Winds (m s^{-1})	0.9	197	80	76	20	1.5	*-0.9 ± 0.4*	6	-0.3 ± 0.9	19	-

Table 14. Current and wind statistics 2004 - 2005.

Mooring	**Mean Velocity**		**Principal Axis**								
2004-2005	Speed (cm s^{-1})	Θ_M	%	Θ_P	Max Speed (cm s^{-1})	τ (days)	<V> (cm s^{-1})	s^2_V	<U> (cm s^{-1})	s^2_U	$\frac{s^2_{subtidal}}{s^2_{total}}$
Full Record											
Camden	0.3	262	94.7	115	34.4	2.8	0+/-0.6	11	-0.3+/-1.1	39	0.88
Dinkum	2.4	308	97.1	119	69.9	2.9	*1.5+/-1.2*	45	-1.9+/-1.9	135	0.87
Smith	2.6	269	93.8	98	75.6	4.6	-0.1+/-0.2	10	-2.6+/-3.6	123	0.90
Winds (m s^{-1})	2.4	258	88.5	70	22.0	2.4	*-.5+/-0.4*	7.9	*-2.3+/-0.9*	30.8	
Landfast Ice Period											
Camden	0.8	126	85.4	122	24.3	5.9	-0.5+/-0.6	4	0.6+/-0.9	8	0.81
Dinkum	0.2	280	88.9	118	17.3	1.8	0+/-0.2	7	-0.2+/-0.9	17	0.74
Smith	0.6	156	59	105	24.1	0.3	*-0.6+/-0.1*	5	*0.3+/-0.2*	7	0.47
Winds (m s^{-1})	2.4	259	90.8	70	22	4.8	-0.5+/-0.8	8.3	*-2.4+/-1.6*	36.6	
Open Water Period											
Camden	2.8	290	96.5	114	34.4	2.1	0.9+/-1.4	25	-2.6+/-2.9	105	0.88
Dinkum	7.9	310	98.2	118	69.9	1.9	*5.1+/-2.9*	122	*-6+/-5.5*	404	0.87
Smith	12.2	278	95.3	97	75.6	2.5	*1.7+/-0.8*	25	*-12+/-9.5*	390	0.91
Winds (m s^{-1})	2.3	256	81.8	69	14.3	1.7	*-0.6+/-0.5*	7.2	*-2.2+/-1.1*	20.1	

Table 15. Current and wind statistics 2005 - 2006.

Mooring	**Mean Velocity**		**Principal Axis**								
2005-2006	Speed (cm s^{-1})	Θ_M	%	Θ_P	Max Speed (cm s^{-1})	τ (days)	<V> (cm s^{-1})	s^2_V	<U> (cm s^{-1})	s^2_U	$\frac{s^2_{subtidal}}{s^2_{total}}$
Full Record											
Camden	1.6	286	95.2	122	79.4	6.3	0.5+/-1.2	21	-1.5+/-1.8	50	0.88
Dinkum	3.5	303	97.6	119	84.8	4.3	*1.9+/-1.7*	59	*-2.9+/-2.7*	174	0.92
Winds (m s^{-1})	0.7	265	88.3	73	21.6	4.5	-0.1+/-0.5	6.5	-0.7+/-1.2	29.4	
Landfast Ice Period											
Camden	0.5	199	70.7	114	12.5	0.5	*-0.4+/-0.1*	2	-0.1+/-0.2	3	0.62
Dinkum	0.5	294	84.8	120	16.4	0.5	0.2+/-0.2	6	*-0.5+/-0.4*	13	0.69
Winds (m s^{-1})	0.7	49	88.8	71	21.6	2.2	0.5+/-0.5	6.6	0.5+/-0.9	27.2	
Open Water Period											
Camden	4.9	297	95.9	122	79.4	4.9	2.2+/-3.0	56	-4.4+/-4.5	134	0.89
Dinkum	10.3	305	98.3	119	84.8	1.9	*5.8+/-3.3*	156	*-8.5+/-5.6*	493	0.93
Winds (m s^{-1})	3	251	85.5	80	18.5	1.6	*-1+/-0.3*	5.1	*-2.9+/-1.3*	25.9	

Table 16. Current and wind statistics 2006 – 2007.

Mooring	**Mean Velocity**		**Principal Axis**								
2006-2007	Speed (cm s^{-1})	Θ_M	%	Θ_P	Max Speed (cm s^{-1})	τ (days)	<V> (cm s^{-1})	s^2_V	<U> (cm s^{-1})	s^2_U	$\frac{s^2_{subtidal}}{s^2_{total}}$
Full Record											
Camden	1.4	282	96.7	119	80.9	3.3	0.3+/-0.8	25	-1.4+/-1.6	74	0.89
Cross	0.6	274	97	114	104.8	0.8	0+/-0.5	37	-0.6+/-1.2	161	0.90
Winds (m s^{-1})	1.7	258	87	82	21.9	7.2	-0.3+/-0.7	5.1	*-1.6+/-1.1*	29.9	
Landfast Ice Period											
Camden	1.5	135	88	125	18.4	1.8	*-1.1+/-0.3*	4	*1.1+/-0.5*	7	0.78
Cross	1.2	131	95.5	113	60.4	0.7	*-0.8+/-0.3*	11	*0.9+/-0.8*	46	0.87
Winds (m s^{-1})	1	-87	89	82	19.6	4.1	0+/-0.6	4.9	-1+/-1.5	34.4	
Open Water Period											
Camden	5.8	295	97	119	80.9	0.7	*2.4+/-0.9*	50	*-5.2+/-1.7*	152	0.88
Cross	2.7	293	97.2	114	104.8	0.9	1.1+/-1.1	68	*-2.5+/-2.5*	301	0.90
Dinkum	6.9	292	98	114	78.5	0.6	*2.6+/-2.5*	148	*-6.5+/-5.9*	676	0.88
Winds (m s^{-1})	2.8	250	82.3	84	21.9	2.5	*-1+/-0.7*	4.7	-2.7+/-0.7	21	

Figures 28 and 29 show the mean velocity profiles projected along the major and minor principal axis for the landfast ice period at Reindeer for all eastward and westward

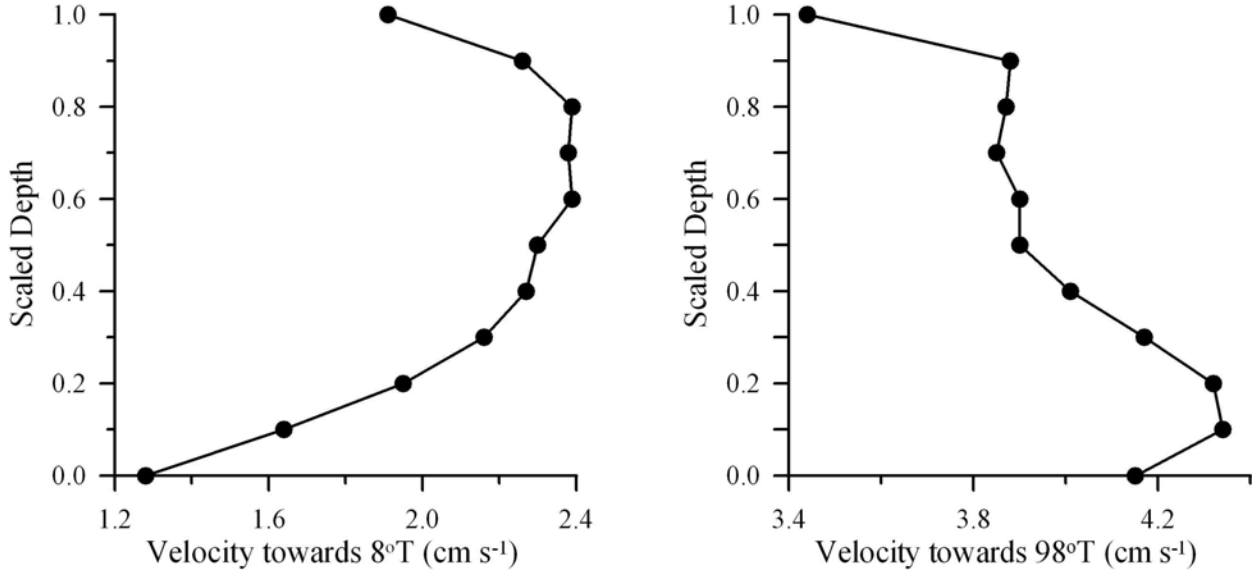

Figure 28. Mean velocity profiles for the cross-shore (left) and alongshore (right) velocity components during eastward flow conditions at REINDEER for the landfast ice season.

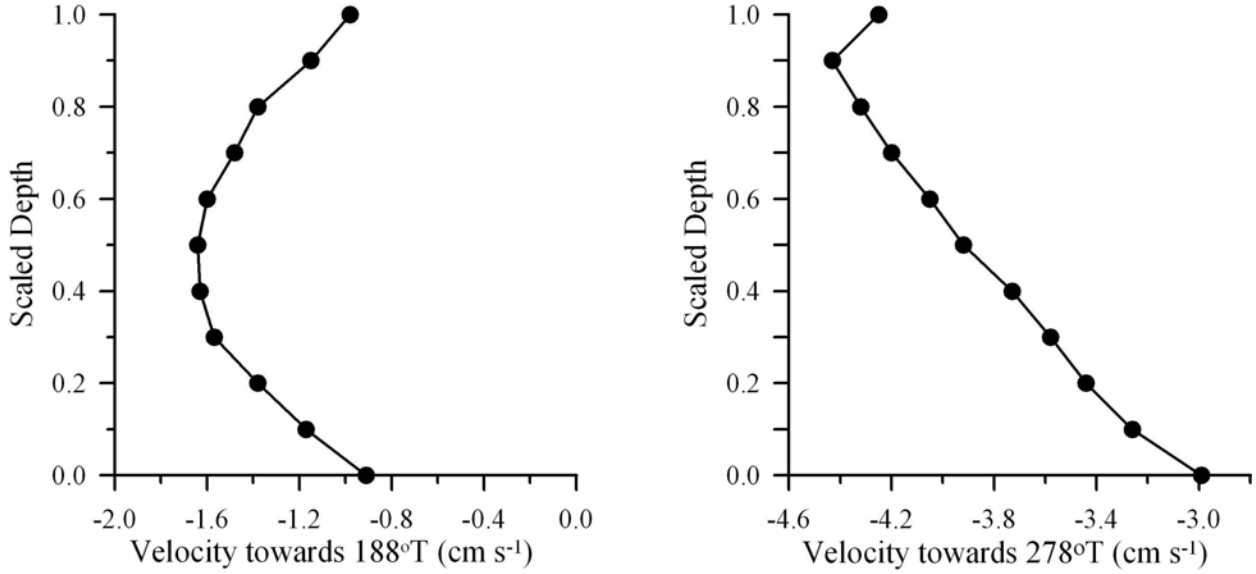

Figure 29. Mean velocity profiles for the cross-shore (left) and alongshore (right) velocity components during westward flow conditions at REINDEER for the landfast ice season.

flow events. The depth axis is the scaled depth which varies from 0 for the bin closest to the ADCP transducer to 1 for the bin nearest to the ice. (The scaling takes into account the changing depth of the water column due either to ice growth or sea level fluctuations.) In both cases the mean velocity varies by ~1 cm s^{-1} over the depth of the water column. The small vertical shear is typical of the landfast ice season at all moorings, except for CROSS (discussed in section 6). The open water season velocity profiles are also considerably different under eastward and westward flows due to the stratifying influence of freshwater runoff. These profiles will be discussed in Section V.

These seasonal current speed differences are also reflected in the summary speed histograms constructed from the unfiltered data for all years (**Figures 30 and 31**). Less than 2% of all current speeds exceed 15 cm s^{-1} during the landfast ice period, while more

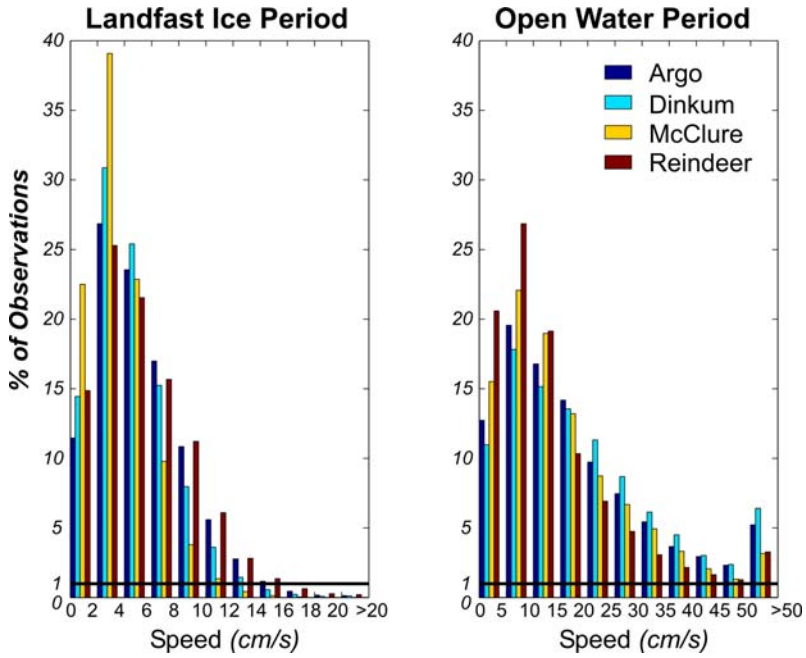

Figure 30. Histograms of unfiltered current speeds for the landfast ice and open water period at all moorings between 1999-2002. The solid horizontal line indicates the 1% level.

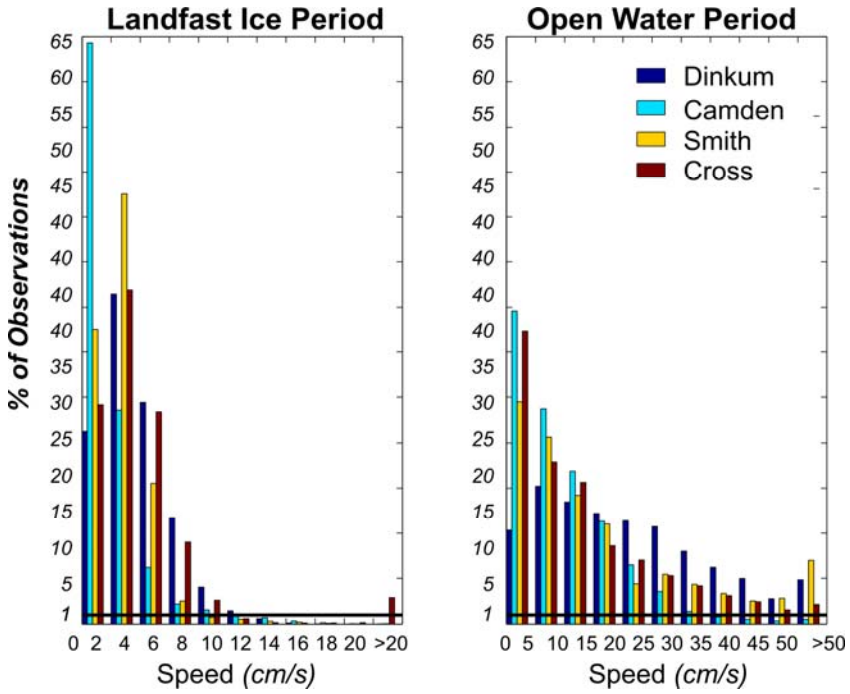

Figure 31. Histograms of unfiltered current speeds for the landfast ice and open water period at all moorings between 2004-2007. The solid horizontal line indicates the 1% level. Note the difference in vertical scale between Figures 30 and 31.

than 50% of the observations exceed this speed during the open water season. The one exception is that ~3% of the currents exceeded 20 cm s^{-1} at CROSS during the landfast ice season. This is discussed in more detail later, but these high currents occurred in November 2007, early in the landfast ice season and occurred as the ice advanced and retreated over this mooring over a period of several days. Our direct measurements during the landfast ice period thus agree with *Aagaard's* [1984] findings that currents under the landfast ice are small and suggest that *Matthews'* [1981] inferences that current speeds could be as large as 35 cm s^{-1} are highly unlikely (except possibly in channels between the barrier islands). Speeds of this magnitude were never observed under the landfast ice except once at ARGO where the maximum speed was 25 cm-s^{-1}. In summary ~90% of the underice current speeds are $\leq$10 cm s^{-1}.

The ratio of the subtidal to the total variance was calculated by comparing the variance from the filtered data to the unfiltered data. Subtidal variance accounts for from 50 – 80% of the total variance during the land fast ice period and for more than ~80% of the total variance during the open water period. There are differences in these ratios among years and sites, however. For example, the ratios at McCLURE are generally smaller than elsewhere, although not because of smaller tidal current amplitudes, which as shown later, are similar at all locations. More likely these differences reflect the geometry of Stefansson Sound, which broadens from west to east. Current variations are consequently larger in the western and central portions of the sound (e.g., DINKUM, ARGO) than in the eastern sound (e.g., McCLURE). There are also interannual differences in this ratio. For example, at DINKUM the subtidal variance ranges between 54% and 74% of the total variance for each landfast ice period. Interannual variations in these ratios reflect differences in the subtidal current variance and the differences between years are statistically significant at the 95% significance level based on the *F*-statistic. Although the subtidal variances differ significantly among years, there are no corresponding significant year-to-year differences in wind variances. This suggests little coupling between local winds and the underice currents, a point which we will return to later.

2. Progressive Vector Diagrams

In this section we examine seasonal and spatial differences in current speeds using modified Progressive Vector Diagrams (PVD) to examine the probabilistic distribution of water parcels released at the various mooring sites. PVDs involve integrating the path that a hypothetical particle would follow if released at the mooring site and then subsequently carried by the ocean currents. The calculations assume that currents are

spatially homogeneous, e.g., the observed currents at any instant in time are identical throughout the region considered. The main utility of this approach is that provides guidance on how (and the probability of where) oil may spread in different seasons and over specified durations.

The modified PVD calculation proceeds as follows. For the measurement interval Δt (=1200 to 1800 seconds), analysis period $T=n\Delta t$ (n is an integer), zonal flow $u(t)$ and meridional flow $v(t)$, the particle's x- and y- (eastward and northward) displacements at the end of the integration period are given by:

$$X(n) = \sum_{t=1}^{n} \Delta t \cdot u(t)$$
$$Y(n) = \sum_{t=1}^{n} \Delta t \cdot v(t) \qquad (1)$$

An example PVD plot, which spans 96 hours, shows the position after each Δt (**Figure 32**). After making a clockwise loop over the first 64 hours, the particle drifted to the south-east for the final 32 hours. The ending location is described by the integration endpoints $X(N)=21.6$ and $Y(N)=-11.6$. In this example, the maximum distance attained by the particle (measured from the start location) is the same as the final distance.

Instead of showing each PVD, our modified PVDs simply show the endpoints of each PVD calculation for T= 4 and T = 12 days (e.g., n = 288 and 864, respectively). (Other integrations were performed at 2 and 8 days and these can be found in Danielson and Weingartner, 2007 or at http://www.ims.uaf.edu/beaufort/index3.html.) Particles are initialized daily at midnight, so the number of particles given in the figures below is the same as the total number of days of observations at the mooring site. For integrations that cross the boundary between the two seasons, the results are assigned to the open

water and free drift season. Currents measured during mid-winter landfast ice breakout events (rare at most of our sites) are considered to be within the landfast ice season.

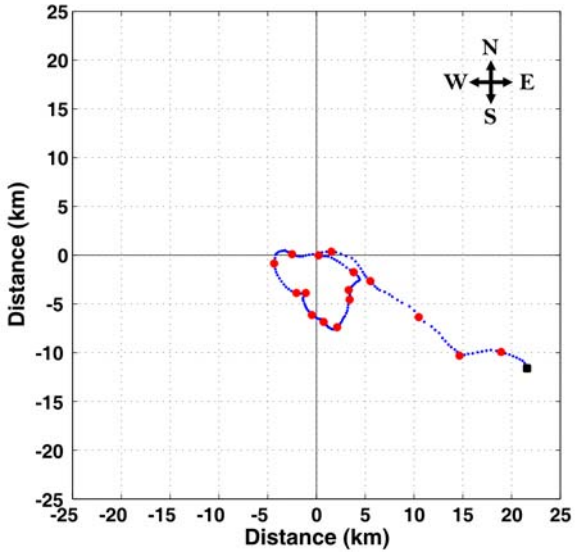

Figure 32. An example 4-day PVD from the Argo site initialized at midnight August 15, 1999 at the center point (0, 0). Measurements were made every 30 minutes. The blue dots are the particle positions plotted at every time step and the red dots are plotted every 6 hours. The final position is plotted in black.

The PVD analysis assumes that the flow field is spatially homogenous, e.g., velocities are everywhere equal to that measured at a specified time at the mooring site. For analyses in which the particle does not move very far from the starting location, this assumption is generally valid. Thus the calculations are probably reasonable for the landfast ice period when displacements are relatively small. Nevertheless, the approach is probably reasonable when considered in terms of potential dispersion characteristics of a contaminant rather than as exact trajectories.

The integral time scales (de-correlation time scale) for the currents are approximately 2-5 days in the winter and 3-6 days in the summer. Thus, these overlapping analyses are not fully independent samples, resulting in fewer degrees of freedom than the total number of PVD iterations run. Additionally, it means that the

longer 8 and 12 day integrations amount to 2 – 6 independent measurements. Nonetheless, this method yields a similar distribution of particles as would a smaller ensemble of completely independent samples. Although there are several ways to construct the modified PVDs, we believe that starting the integration only once per day is a conservative approach that provides a good balance between keeping the integrations quasi-independent while still providing a reasonably clear picture of particle dispersion over both seasons.

There are several caveats associated with the modified PVDs that need to be borne in mind when examining these figures:

1. Spilled oil can be absorbed into the ice matrix. Upon breakup the landfast ice is mobile so the location where the ice subsequently melts may be far removed from the location where the oil was entrained.
2. The underice bathymetry is not known, but could channel or funnel oil in pathways different than suggested by the modified PVDs. Concave topographic features may act to trap oil in thicker pools.
3. The modified PVDs are all from shallow water sites located close to shore and under landfast ice in the winter. The PVD analysis endpoint locations were primarily found to be within this same domain. Our results are unlikely to apply to locations farther seaward, including at the landfast ice edge or in the pack ice.
4. Circulation offshore from major rivers will likely behave differently than at the sites in this study, including regions near the Colville, Kuparuk and Canning rivers. In particular, the period following maximum river discharge is a critical time period. The fresh river plume could disperse oil in the offshore direction, as opposed to the normally along shore flow observed at our mooring sites.
5. Although the ADCP measurements are taken from the uppermost bin with good data, the ADCP measurements are contaminated in the bin actually closest to the sea surface or the ice bottom. Thus, our measurements are located below the depth where oil is likely to float. During the spring river freshet, the currents in this thin topmost layer could be quite strong and possibly different than in the ADCP bin with good data that is closest to the surface. During the winter, when there is presumably little stratification, the currents are vertically uniform, with some suggestion of a decrease in current speed near the surface.
6. At the sites occupied in this study, landfast ice breakout events (detachment of a portion of the landfast ice canopy) are unusual. Landfast ice breakout events may be more common at other locations. We expect higher under-ice currents and

farther particle displacements at and near breakout events. The Smith Bay mooring was deployed beneath and sampled during one landfast ice breakout event.

7. River discharge and summer storms can create high levels of turbidity (suspended sediment) in the water column. Sediment entrained into oil plumes will change its density and may affect where in the water column the oil will be found. Moreover, sediments are incorporated into landfast ice during its fall formation. Oil covered sediments within the ice matrix might subsequently be released after breakup and melt back into the water. This may occur far from the location in which incorporation occurred.

Table 17 contain the seasonal summary statistics for the open water and freely drifting ice season. **Table 18** summarizes the statistics for the landfast ice period. The following notes pertain to these tables:

1. All distances are given in km, measured from the mooring site. All integrations began at position (0, 0) and were initialized daily at midnight.
2. The *Analysis Length* indicates the PVD integration period in days.
3. *M* is the number of PVD integrations.
4. The *Maximum Displacement* columns refer to the particle's farthest displacement attained within the integration period.
5. The *Final Displacement* columns refer to the particle position at the end of the integration period.
6. The *Greatest Maximum and Final Displacement* columns describe the single farthest displacement observed within each set of integrations given in the *Maximum* and *Final Displacement* columns.
7. The *Mean Final Zonal and Meridional Displacement* (east-west/north-south) columns describe the central point of all ending particle locations. Negative values indicate westward or southward displacements; positive values indicate eastward or northward displacements. The winter values are small and negative, indicating that nearly as many particles travel east (north) as those that travel west (south), but with a slight bias to the west and to the south at most sites. Summer values are more commonly westward and northward.
8. The total number of seasonal observations and weighted mean values (based on number of observations per site) are given in red.
9. The largest mean maximum, greatest maximum and mean final displacements for each integration period are highlighted in yellow.

Table 17. PVD Summary Statistics for the Open Water and Freely Drifting Ice Period

Mooring	Analysis Length (days)	N	Mean Maximum Displacement (km)	Maximum Displacement Std. Dev. (km)	Greatest Maximum Displacement (km)	Mean Final Displacement (km)	Mean Final Distance Std. Dev. (km)	Greatest Final Displacement (km)	Mean Final Zonal Displacement (km)	Mean Final Meridional Displacement (km)
Argo	2	318	33.8	25.4	140.3	32.5	26.3	140.3	-8.3	2.3
Dinkum	2	541	37.9	26.9	134.4	36.2	28	134.4	-8.2	7.4
McClure	2	232	29.8	22.6	109.7	28.6	23.4	109.7	-0.3	4.4
Reindeer	2	90	44.5	31.9	114.6	43.5	32.1	114.6	-11.7	-8.6
Camden Bay	2	224	19.2	15.2	72.6	18.3	15.6	72.6	-7	3.8
Smith Bay	2	77	29.5	28.5	101	29	28.8	101	-22.4	5.3
MEAN	**2**	**1482**	**32.9**	**24.5**	**119.5**	**31.6**	**25.3**	**119.5**	**-7.8**	**4.2**
Argo	4	318	58.1	44.0	250.2	53.5	45.8	250.2	-16.0	4.5
Dinkum	4	541	65.9	46.7	235.5	60.5	49.4	235.5	-16.0	14.5
McClure	4	232	51.0	40.5	196.0	46.6	42.5	196.0	-0.2	8.3
Reindeer	4	90	75.5	53.9	170.4	72.2	54.5	170.4	-23.6	-16.7
Camden Bay	4	222	33.8	26.9	117.8	31.1	27.8	117.8	-14.3	8.0
Smith Bay	4	77	56.3	54.3	199.0	55.6	54.7	199.0	-44.9	10.8
MEAN	**4**	**1480**	**57.2**	**43.0**	**209.0**	**52.9**	**44.9**	**209.0**	**-15.2**	**8.3**
Argo	8	318	96.6	75.4	437.4	86	78.4	437.4	-30.5	8.6
Dinkum	8	541	110.7	79.2	398.5	100.6	82.5	398.5	-32.3	29
McClure	8	232	85.5	72.2	339.2	77.7	74.1	339.2	0.8	15
Reindeer	8	90	112.5	77.7	291.2	102.8	77	290.1	-53	-33.1
Camden Bay	8	218	58.9	47.5	181.6	53.5	49.6	181.6	-29.6	17
Smith Bay	8	77	105.4	104.9	370.9	103.9	105.7	370.9	-89.7	21.3
MEAN	**8**	**1476**	**95.9**	**73.6**	**356.6**	**87.0**	**76.1**	**356.5**	**-30.5**	**16.4**
Argo	12	318	123.5	97.1	588.9	107.2	99.4	588.9	-41.1	11.7
Dinkum	12	541	145.8	103.1	522.7	130	106.3	522.7	-47	42.2
McClure	12	232	112.3	92.6	445.3	100	94.6	445.3	4	18.1
Reindeer	12	90	142.6	96.5	308.3	130.4	95	308.3	-80.2	-47.9
Camden Bay	12	214	79.5	68.8	281.1	71.3	72.2	281.1	-46.7	27.1
Smith Bay	12	77	151.3	150.3	515.6	148	152.2	515.6	-134.8	31.8
MEAN	**12**	**1472**	**126.2**	**96.7**	**473.6**	**112.2**	**99.2**	**473.6**	**-44.0**	**23.4**

Table 18.: PVD Summary Statistics for the Landfast Ice Period

Mooring	Analysis Length (days)	N	Mean Maximum Displacement (km)	Maximum Displacement Standard Deviation (km)	Greatest Maximum Displacement (km)	Mean Final Displacement (km)	Mean Final Distance Standard Deviation (km)	Greatest Final Displacement (km)	Mean Final Zonal Displacement (km)	Mean Final Meridional Displacement (km)
Argo	2	760	5.3	3.5	20.7	4.9	3.7	20.7	-0.7	0.1
Dinkum	2	1252	4.9	2.9	17.8	4.6	3	17.8	-0.3	-0.4
McClure	2	509	3.9	2.4	12.9	3.7	2.6	12.9	-0.5	1
Reindeer	2	258	4.5	2.9	17.6	4.1	3	17.6	-1.4	-0.5
Camden Bay	2	492	2.4	2.7	23.5	2.3	2.7	23.5	-0.3	-0.6
Smith Bay	2	249	2.7	1.7	12.3	2.6	1.7	12.3	-0.8	-1.2
MEAN	**2**	**3520**	**4.3**	**2.8**	**18.1**	**4.0**	**3.0**	**18.1**	**-0.5**	**-0.2**
Argo	4	750	9.2	6.0	35.6	8.2	6.3	35.6	-1.4	0.1
Dinkum	4	1242	8.5	4.8	34.1	7.6	5.1	34.1	-0.5	-0.8
McClure	4	505	6.9	4.4	23.7	6.3	4.6	23.7	-1.0	2.1
Reindeer	4	256	7.5	4.5	23.1	6.7	4.7	23.1	-2.8	-1.1
Camden Bay	4	488	4.4	4.7	30.9	4.3	4.8	30.9	-0.6	-1.2
Smith Bay	4	247	4.9	2.5	16.0	4.7	2.5	16.0	-1.6	-2.4
MEAN	**4**	**3488**	**7.5**	**4.8**	**30.4**	**6.8**	**5.0**	**30.4**	**-1.0**	**-0.4**
Argo	8	730	15.8	10.2	43.8	14.1	10.7	43.8	-3.0	0.3
Dinkum	8	1222	14.5	8.0	44.1	13.0	8.6	44.1	-1.1	-1.7
McClure	8	497	12.4	7.6	35.7	11.6	8.0	35.7	-2.1	4.2
Reindeer	8	252	12.6	6.8	34.9	11.2	7.1	34.9	-5.9	-2.3
Camden Bay	8	480	8.2	8.3	48.8	7.9	8.3	48.8	-1.3	-2.5
Smith Bay	8	243	8.8	4.0	18.5	8.5	4.2	18.5	-3.4	-4.8
MEAN	**8**	**3424**	**13.0**	**8.1**	**41.0**	**11.9**	**8.5**	**41.0**	**-2.2**	**-0.8**
Argo	12	710	21.6	14.4	62.8	19.3	15.1	62.8	-4.6	0.4
Dinkum	12	1202	19.9	11.0	61.6	17.7	11.8	61.6	-1.8	-2.6
McClure	12	489	17.6	10.8	48.6	16.6	11.3	48.6	-3.4	6.5
Reindeer	12	248	16.8	8.6	41.9	14.5	8.8	41.9	-9.0	-3.6
Camden Bay	12	472	11.7	11.7	75.5	11.4	11.7	75.5	-2.1	-3.7
Smith Bay	12	239	12.5	5.3	25.3	12.2	5.5	25.3	-5.2	-7.4
MEAN	**12**	**3360**	**18.0**	**11.2**	**57.9**	**16.4**	**11.7**	**57.9**	**-3.4**	**-1.2**

Figures 33 – 37 are summary plots for the 4-day analysis at the Dinkum site, the mooring site with the largest data set. (Modified PVD plots for the other sites and the 12-day integrations can be found in *Danielson and Weingartner*, 2007) While the data used in these plots are identical, the various plots display the data in different ways. Thus **Figures 33 and 34** are scatter plots, **Figures 35 and 36** are polar plots, with the endpoints binned into discrete angular bins, and **Figure 37** contains probability distributions. One potential use for these plots is to compare with model simulations. A second is for oil-spill response planning. For instance, if it takes 4 days to mobilize for a spill, the plots show the likely spatial distribution of 80% of the oil in a 4-day period. During the landfast ice season the results suggest that 80% of all the oil spilled at Dinkum would remain within a 20 km alongshore and a 10 km cross-shore band. During the open water season these distances increase to 150 km and 25 km respectively.

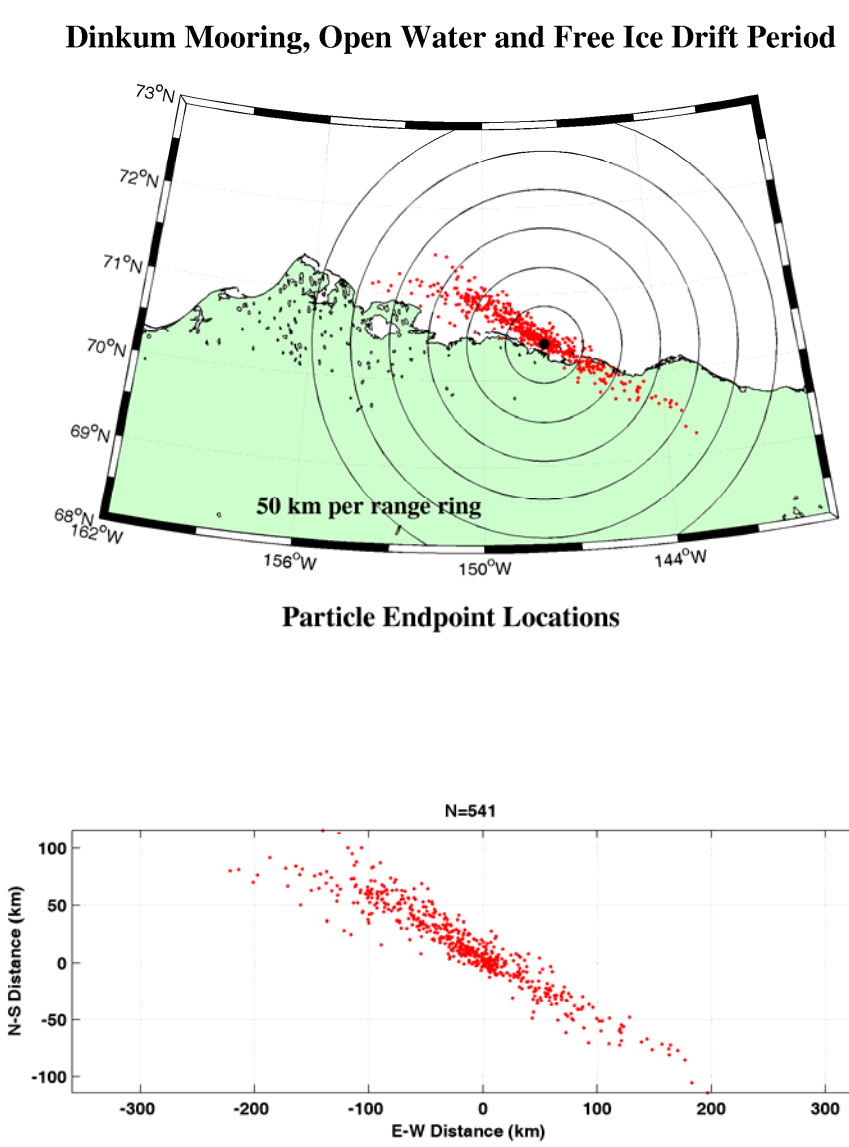

Figure 33. Particle endpoint locations (red dots) for all PVD 4-day integrations plotted on a map (upper panel) and in Cartesian space (lower panel) during the open water and free ice drift period. N indicates the number days in the analysis. The black dot in the map is the mooring location and is at co-ordinates (0, 0). Range rings provide distance references from the mooring site.

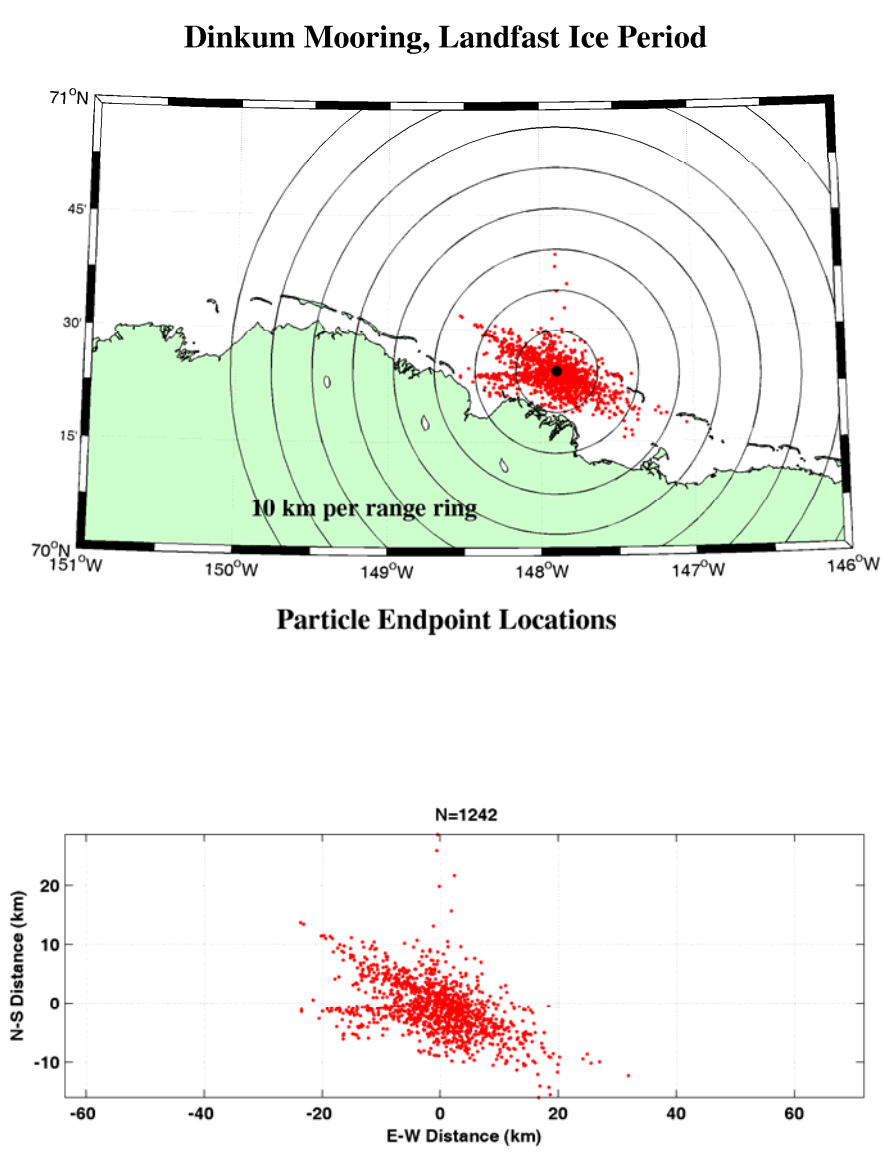

Figure 34. As in Figure 33 for Dinkum except for the landfast ice period.

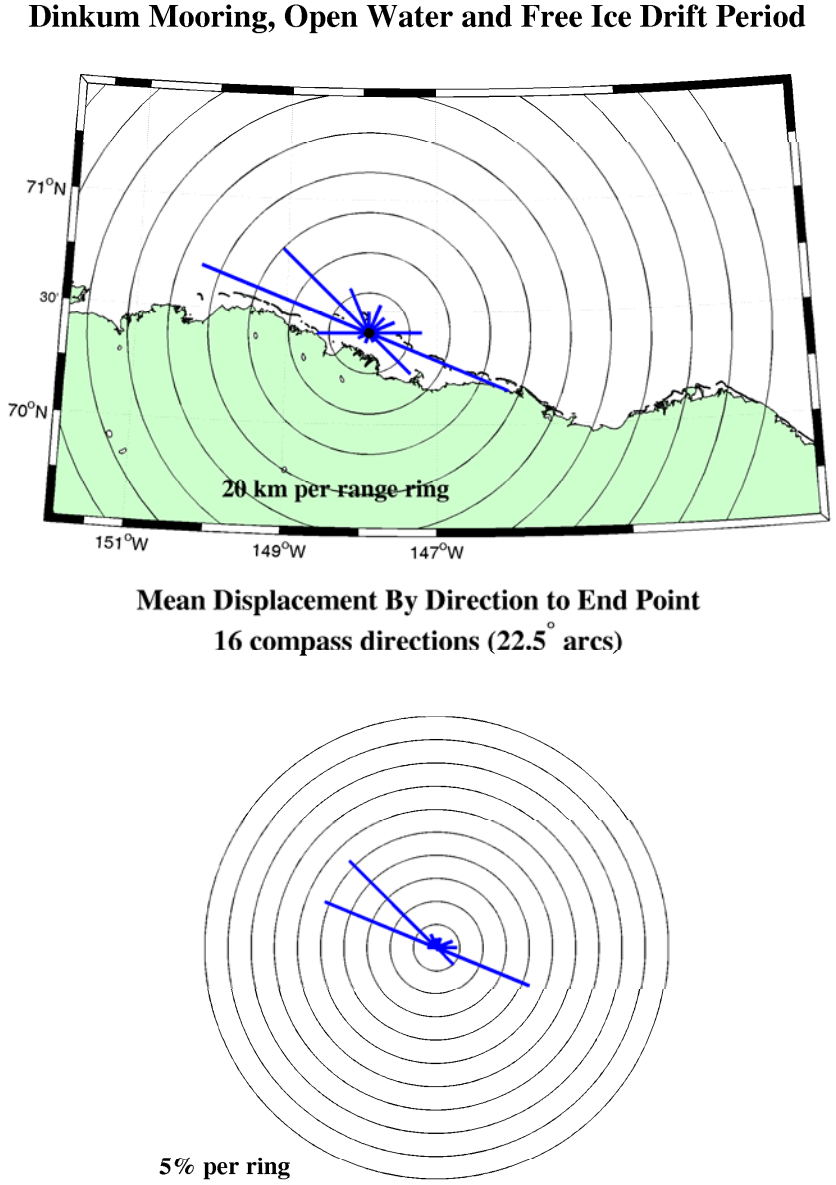

Figure 35. Average particle displacement based on the direction from the Dinkum mooring to the particle end location (upper panel). The plots are the mean PVD endpoint locations of all 4 day iterations (initialized daily) from the open water and free ice drift period. Directions were binned into 16 compass directions (22.5º arcs). Thus. bars indicating northward motion includes all endpoints located between compass directions from 348.75ºT to 11.25ºT. The lower plot shows the percentage of all particle endpoints in each of the 16 directions. Each ring represents 5% of the total number of particles released. West is to the left, north to the top of the page.

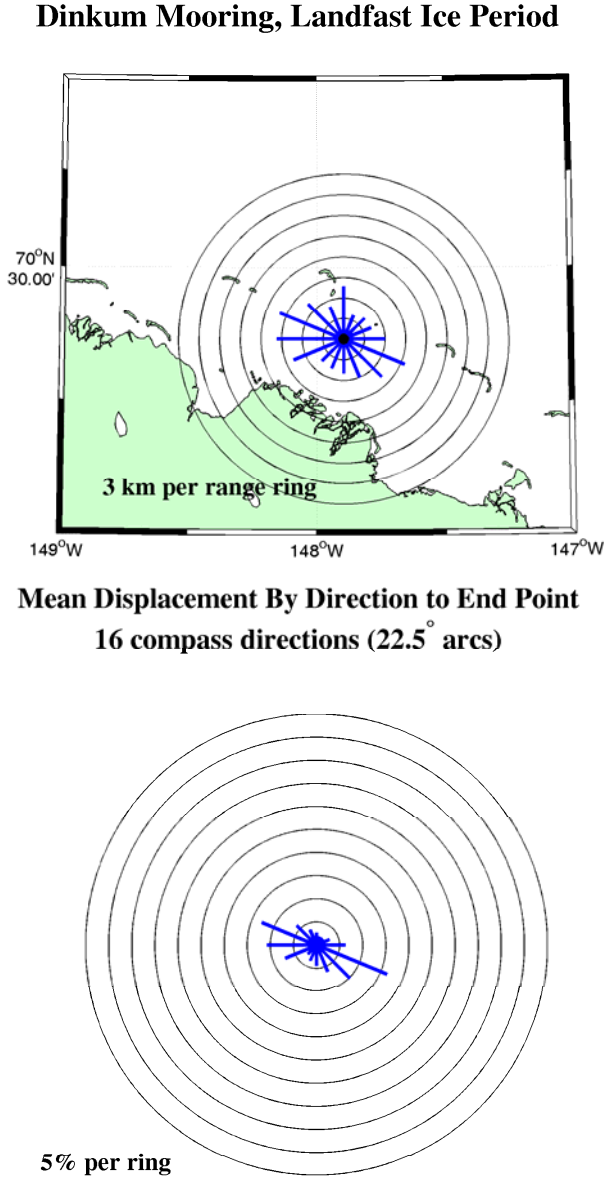

Figure 36. Same as Figure 35 except for Dinkum during the landfast ice season.

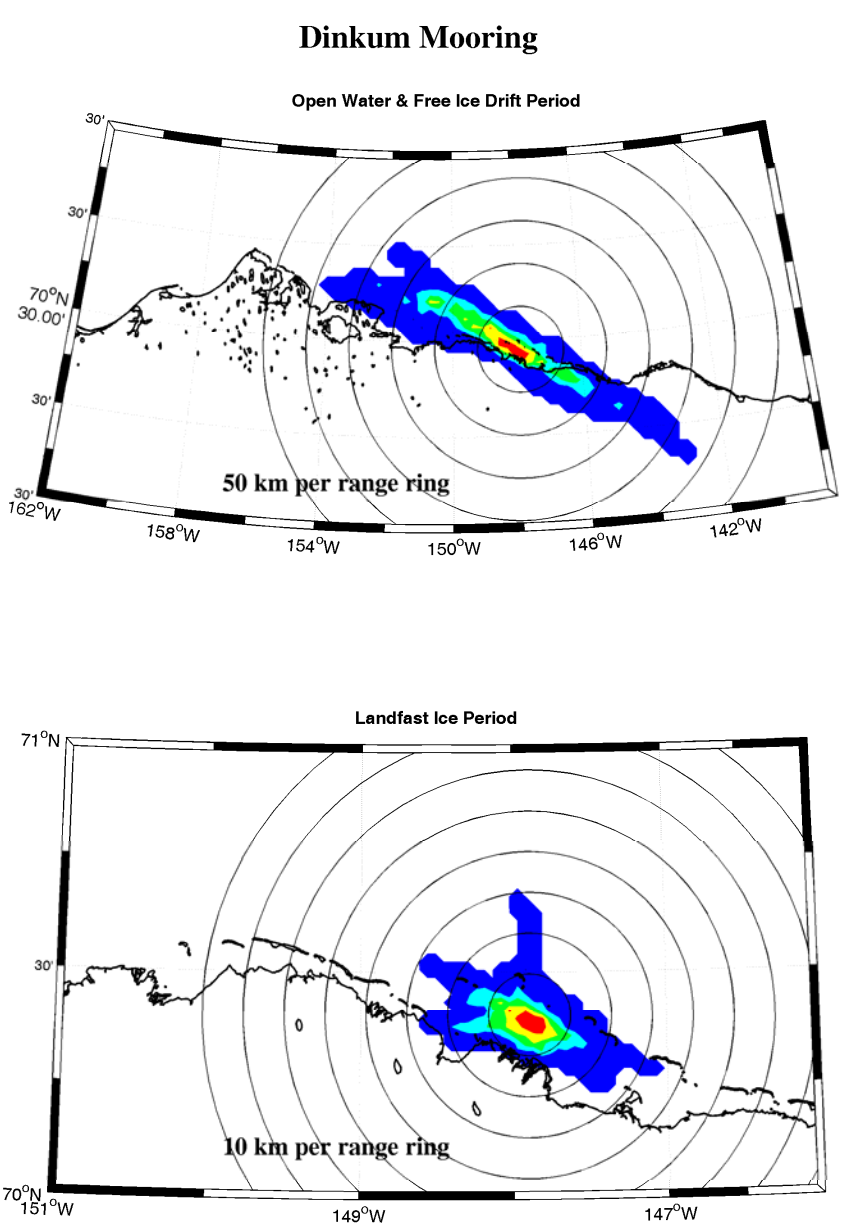

Figure 37. Particle dispersion extent and density. The red (blue) areas have the highest (lowest) endpoint density. Colors vary by increments of 20%, with 0% indicated by white; 20% of all particle endpoint locations fall within the red area and the remaining 80% of all particles are found within the dark blue, cyan, green and yellow areas. Conversely, 80% of all particle endpoints fall within the cyan, green, yellow and red areas, with the remaining 20% in the dark blue area. To reduce noise, the PVD analysis was re-run for these plots with one analysis begun each *hour*, rather than once per day. Plots that depict gappy distributions (typically summer plots with only 1 or 2 years worth of data and long integration periods) do not have enough data to adequately describe the likely distribution extent or probabilities for any particular area.

Figure 38 summarizes these results by plotting the cumulative displacement frequency as a function of the displacement distance for all sites and by season and includes results from the 2-, 4-, 8- and 12-day integrations. These are based on concentric circles about the mooring site whose radii are given by the distances on the horizontal axis. The vertical axis describes the fraction of all particle endpoint locations found within each circle. The results suggest that:

1. For the 2- to 12-day integrations considered, oil spill displacement will be relatively small during the landfast ice season (10s of kilometers) and relatively large during the open water and drifting ice season (100s of kilometers).
2. Transport in the summer is highly dependent upon the wind speed and direction.
3. In both seasons, transport of oil in the alongshore (east-west) direction is substantially greater than transport in the cross-shore (north-south) direction.
4. Over a 12 day period, an oil spill at the mooring locations during the landfast ice season would, *on average,* be confined to within 18 km of the spill site. In contrast, during the open water season, the average displacement would be 126 km. Over a 4 day period, the average oil spill displacement for the two seasons is 8 km and 57 km respectively.
5. On average the average oil slick leading edge would move 1.5 - 2 km per day under the landfast ice and 10-15 km per day in the open water season. In rare cases, oil could move 6 km/day in winter and 60 km/day in the summer.

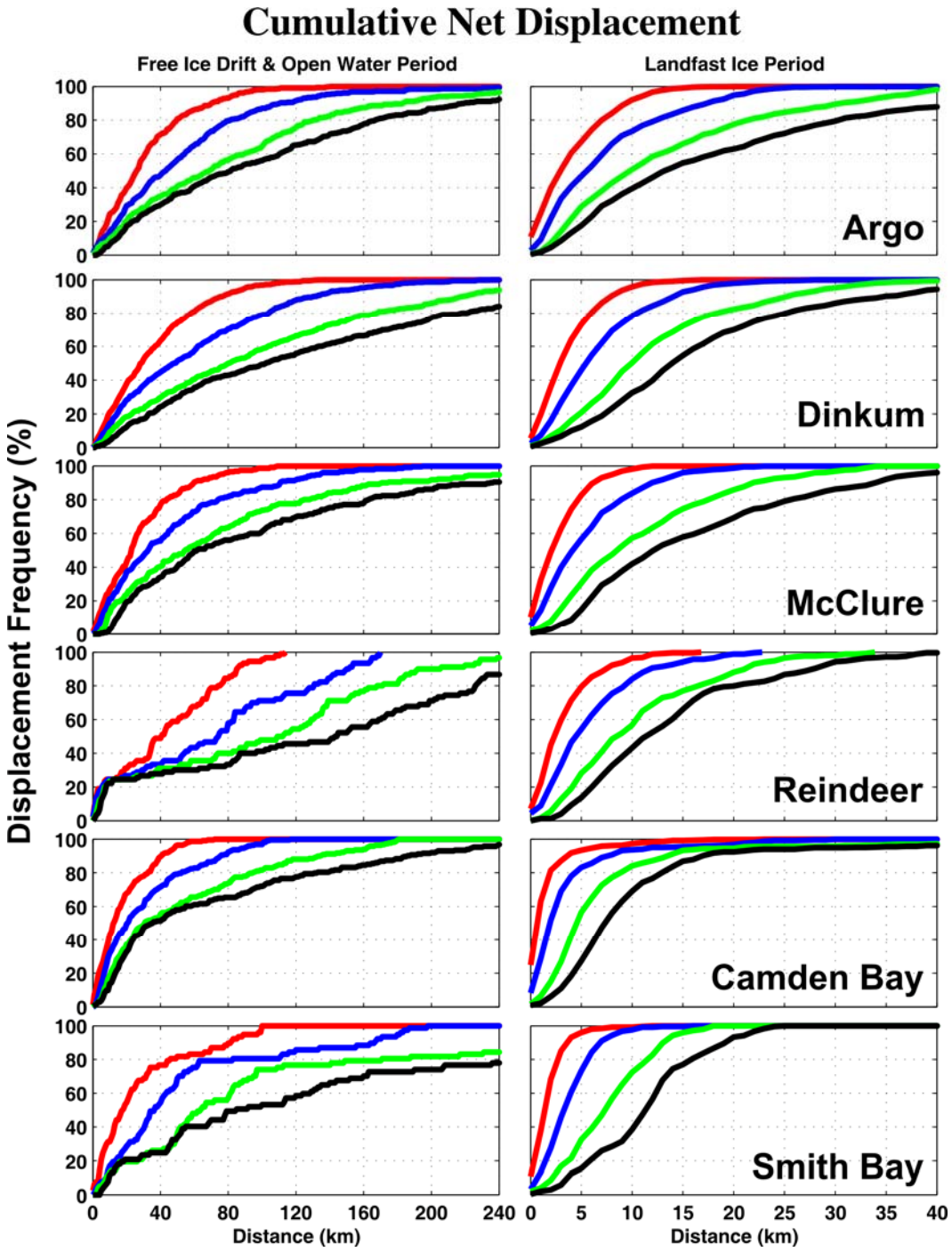

Figure 38. Cumulative displacement frequency at all six mooring sites during the summer (left) and winter (right). The colors red, blue, green and black are associated with the 2, 4, 8 and 12 day analyses, respectively.

3. Tidal properties

Tidal current properties were estimated for each current meter record following *Foreman* [1978] and *Pawlowicz et al.* [2002]. The four largest constituents and periods (T_p) are the semi-diurnal, M_2, (lunar, T_{M2} = 12.42) and S_2 (solar T_{S2} = 12.00) and the diurnal O_1 (luni-solar, T_{O1} = 25.82 hrs) and K_1 (lunar, T_{K1} = 23.93 hrs). Tidal hodograph analyses are summarized in **Tables 19 and 20. Figure 39** illustrates the various meaning of the terms that describe the hodograph. The M_2 constituent has the largest current amplitudes (~2 –3 cm s^{-1}), while the other species have amplitudes of $\leq$1 cm s^{-1}. The semi-diurnal tides execute nearly circular tidal motions and rotate anticyclonically, while the diurnal tides are nearly rectilinear (flattened ellipses) and oriented alongshore. Their rotational sense is ill-defined because the semi-minor axis is not significantly different from zero.

The semi-major axis, semi-minor axis, ellipse orientation, and Greenwich phase lag, calculated from successive 29-day overlapping segments of the current records at each mooring and for all years are shown in **Figures 40 – 43** for the four largest tidal constituents at Dinkum. Hodograph parameters vary throughout the year, particularly for the semi-diurnal species because of seasonal changes in ice thickness and extent, and possibly because the larger-scale underice topography that affects frictional stresses between the propagating tidal wave and sea-ice, and stratification.

Although these seasonal variations are generally small, those associated with the spring freshet are substantial. Consider for example, the variation in the hodograph parameters of the M_2 tide at DINKUM (**Figure 40**). The semi-major axis varies seasonally and with depth but is a maximum of 5 cm s^{-1} in July 2001 beneath the ice during river breakup and a minimum of about 1.5 cm s^{-1} shortly thereafter near the bottom. Depth variations in tidal properties indicate either

generation of an internal tide associated with stratification or vertical variations in eddy viscosity [*Danielson and Kowalik*, 2006] associated with the strong pycnocline established as the spring

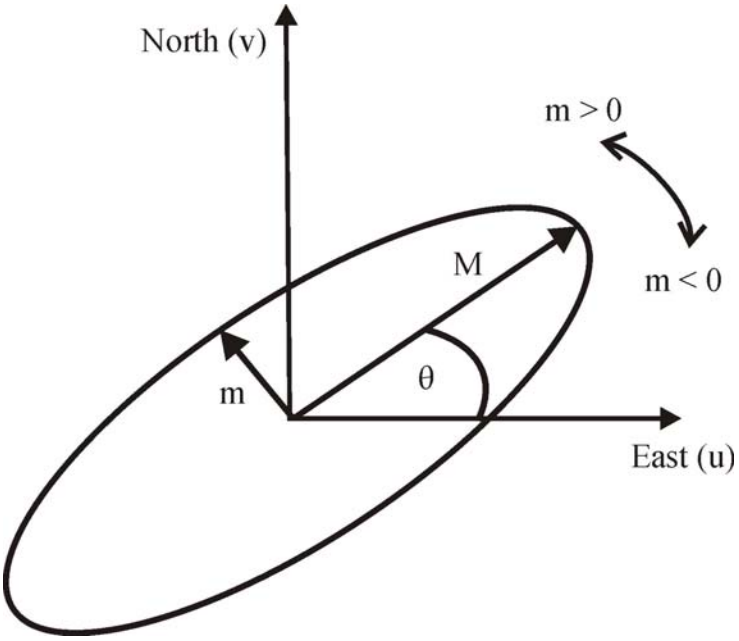

Figure 39. A definition sketch of a tidal ellipse (or hodograph) illustrating the terms associated with the tidal ellipse parameters: *M*, the semi-major axis, *m*, the semi-minor axis, and θ, the angle of inclination (from east). The tidal velocity vector rotates cyclonically (counterclockwise if $m>0$) and anticyclonically (clockwise) if $m<0$.

freshet flows beneath the landfast ice as discussed later. Tidal velocity shears are also small being ~0.003 s^{-1} at most and are not an important source of kinetic energy for mixing (as shown later). The tidal analyses suggest that hodograph properties vary seasonally throughout the landfast portions of all arctic shelves. While these variations are unlikely to be dynamically significant in the Alaskan Beaufort Sea, they might be important in the landfast ice zones of the Laptev and Kara seas, where tides are much more energetic [*Kowalik and Proshutinsky*, 1994].

Furthermore, the results suggest caution should be exercised when comparing tidal hodographs from short-term observations in the landfast ice zone with those from numerical tidal models. Differences between the two might not necessarily indicate model deficiencies but instead be due to seasonal variations in the tidal structure masked by short-duration

measurements. We also note that the effect of landfast ice should have a strong influence on the structure of the super-inertial tidal (M_2 and S_2) currents. The boundary layers associated with these constituents might overlap in shallow water and promote mixing (assuming sufficient tidal energy dissipation). As the water depth increases the tidal boundary layers will separate, possibly allowing a stratified layer to be maintained in the middle of the water column. Conceivably this might lead to the development of a tidal front further offshore, but inshore of the landfast ice edge. Such fronts are capable of supporting an along-shore flow, and if present, likely to be found in the Laptev or Kara Sea where tidal velocities are substantially greater.

Table 19. 1999-2001 tidal ellipse parameters (based on the vertically averaged current component) for major tidal constituents at each site and year. Major (**M**) is the semi-major axis of the current ellipse and minor (**m**) is the semi-minor axis (negative values imply clockwise rotation of the velocity vectors and positive values imply counterclockwise rotation). The inclination (θ) is the angle **M** makes from the east. (Figure 31 illustrates the geometrical meaning of these terms.) The Greenwich phase lag is the time of the maximum constituent velocity relative to Greenwich. Values in parenthesis are the 95% confidence limits for each estimated parameter.

Luni-solar diurnal K_1 (Period = 23.93 hours)					
Name	**Year**	**Major**	**Minor**	**Inclination**	**Greenwich Phase Lag (degrees)**
		(M; cm s^{-1})	**(m; cm s^{-1})**	**(degrees from east)**	
Argo	1999	0.9 (0.2)	-0.1 (0.1)	187.1 (4.6)	93.2 (11.8)
Argo	2000	0.7 (0.2)	-0.1 (0.1)	180.6 (6.4)	91.6 (19.5)
Argo	2001	1.0 (0.3)	-0.1 (0.1)	173.8 (5.6)	83.6 (14.2)
Dinkum	1999	0.5 (0.1)	-0.1 (0.1)	199.6 (15.7)	59.3 (17.7)
Dinkum	2000	0.6 (0.2)	-0.2 (0.2)	170.1 (19.9)	79.5 (27.0)
Dinkum	2001	0.7 (0.2)	-0.3 (0.1)	170.1 (14.5)	83.3 (18.2)
McClure	1999	0.3 (0.1)	-0.1 (0.1)	237.2 (20.6)	58.0 (22.9)
McClure	2000	0.5 (0.1)	-0.1 (0.1)	260.7 (13.4)	74.6 (12.8)
Reindeer	2001	0.8 (0.2)	-0.0 (0.1)	162.1 (8.7)	101.4 (14.7)
Principal lunar diurnal O_1 (Period = 25.82 hours)					
Argo	1999	1.1 (0.2)	-0.2 (0.1)	182.1 (4.4)	130.4 (10.6)
Argo	2000	1.0 (0.2)	0.1 (0.1)	179.6 (4.4)	121.8 (14.4)
Argo	2001	1.2 (0.2)	0.1 (0.1)	177.6 (4.2)	82.3 (10.6)
Dinkum	1999	0.5 (0.2)	-0.1 (0.1)	199.7 (16.5)	124.6 (20.5)
Dinkum	2000	0.8 (0.2)	0.1 (0.2)	170.8 (11.5)	99.9 (14.1)
Dinkum	2001	0.9 (0.2)	0.2 (0.1)	167.1 (11.1)	80.1 (12.3)
McClure	1999	0.4 (0.1)	0.0 (0.1)	49.4 (16.8)	297.7 (16.5)
McClure	2000	0.4 (0.1)	0.2 (0.1)	38.9 (24.5)	314.0 (22.8)
Reindeer	2001	1.0 (0.2)	0.0 (0.1)	163.2 (7.6)	80.5 (11.8)
Principal lunar semi-diurnal M_2 (Period = 12.42 hours)					
Argo	1999	1.8 (0.1)	-1.3 (0.1)	28.4 (6.2)	62.4 (6.9)
Argo	2000	1.7 (0.1)	-1.3 (0.1)	27.0 (8.4)	81.5 (8.8)
Argo	2001	1.6 (0.1)	-1.3 (0.1)	35.4 (11.7)	55.0 (13.1)
Dinkum	1999	2.0 (0.1)	-0.6 (0.1)	93.0 (3.1)	18.5 (2.5)
Dinkum	2000	1.7 (0.1)	-1.2 (0.1)	78.0 (10.3)	34.8 (10.0)
Dinkum	2001	2.0 (0.1)	-1.0 (0.1)	81.6 (5.5)	17.8 (5.6)
McClure	1999	2.2 (0.1)	-0.2 (0.1)	78.9 (1.9)	28.5 (1.9)
McClure	2000	2.2 (0.2)	-0.4 (0.1)	94.8 (3.2)	53.4 (4.0)

Reindeer	2001	1.4 (0.1)	-0.8 (0.1)	319.4 (5.3)	141.1 (5.8)
Principal solar semi-diurnal S_2 (Period = 12.00 hours)					
Argo	1999	0.8 (0.1)	-0.6 (0.1)	39.5 (17.7)	70.0 (17.1)
Argo	2000	1.0 (0.1)	-0.6 (0.1)	23.5 (10.8)	78.6 (10.6)
Argo	2001	0.8 (0.1)	-0.6 (0.1)	25.5 (16.6)	76.2 (16.0)
Dinkum	1999	0.9 (0.1)	-0.3 (0.1)	92.9 (7.0)	31.9 (6.6)
Dinkum	2000	0.8 (0.1)	-0.5 (0.1)	68.3 (18.9)	44.8 (18.0)
Dinkum	2001	0.8 (0.1)	-0.5 (0.1)	80.4 (16.7)	33.0 (16.3)
McClure	1999	1.0 (0.1)	-0.1 (0.1)	76.0 (4.0)	44.3 (4.7)
McClure	2000	1.0 (0.1)	-0.2 (0.1)	92.8 (6.8)	53.6 (10.7)
Reindeer	2001	0.7 (0.1)	-0.4 (0.1)	329.7 (10.6)	142.6 (11.1)

Table 20. 2004-2007 tidal ellipse parameters (based on the vertically averaged current component) for major tidal constituents at each site and year. The axes of the ellipse are the semi-major (**M**) and semi-minor (**m**; negative values imply clockwise rotation of the velocity vectors and positive values imply counterclockwise rotation). The inclination (θ) is the angle **M** makes from the east. (see **Figure 31**) The Greenwich phase lag is the time of the maximum constituent velocity relative to Greenwich. The 95% confidence limits on each estimated parameter is given in parantheses.

Luni-solar diurnal K_1 (Period = 23.93 hours)					
Name	**Year**	**Major**	**Minor**	**Inclination**	**Greenwich Phase Lag (degrees)**
		(M; cm s^{-1})	**(m; cm s^{-1})**	**(degrees from east)**	
Camden	2004	0.2 (0.1)	-0.0 (0.1)	29.1 (18.1)	206.8 (22.5)
Camden	2005	0.3 (0.1)	0.0 (0.1)	18.4 (12.8)	223.1 (21.5)
Camden	2006	0.2 (0.1)	-0.0 (0.1)	26.4 (24.1)	227.9 (27.4)
Cross	2006	0.6 (0.2)	-0.2 (0.1)	169.9 (11.3)	99.7 (16.8)
Dinkum	2004	0.8 (0.2)	-0.2 (0.1)	173.7 (8.2)	77.3 (11.6)
Dinkum	2005	0.6 (0.2)	-0.2 (0.1)	189.4 (17.3)	82.3 (24.3)
Dinkum	2006	1.1 (1.2)	-0.4 (1.4)	93.0 (132.6)	127.5 (84.5)
Smith	2004	0.5 (0.1)	-0.1 (0.2)	259.6 (22.9)	69.6 (15.1)
Principal lunar diurnal O_1 (Period = 25.82 hours)					
Camden	2004	0.2 (0.1)	-0.1 (0.1)	188.2 (18.5)	102.5 (30.6)
Camden	2005	0.4 (0.1)	-0.1 (0.1)	181.0 (9.3)	99.3 (14.2)
Camden	2006	0.3 (0.1)	-0.1 (0.1)	192.0 (14.5)	92.5 (20.0)
Cross	2006	0.8 (0.1)	0.1 (0.1)	174.2 (6.8)	79.6 (11.4)
Dinkum	2004	0.7 (0.2)	0.1 (0.1)	173.4 (7.3)	68.5 (13.1)
Dinkum	2005	0.8 (0.2)	-0.1 (0.1)	171.0 (9.2)	90.5 (13.0)
Dinkum	2006	1.1 (1.4)	0.3 (0.9)	163.6 (58.3)	3.1 (90.8)
Smith	2004	0.7 (0.1)	-0.2 (0.1)	314.3 (11.6)	62.9 (11.8)
Principal lunar semi-diurnal M_2 (Period = 12.42 hours)					
Camden	2004	0.9 (0.0)	-0.3 (0.1)	63.2 (4.9)	4.3 (3.7)
Camden	2005	1.0 (0.0)	-0.3 (0.0)	59.1 (3.4)	6.7 (2.9)
Camden	2006	0.9 (0.0)	-0.1 (0.1)	79.4 (3.2)	6.7 (2.3)
Cross	2006	1.4 (0.1)	-0.8 (0.1)	285.5 (6.9)	158.0 (5.2)
Dinkum	2004	1.7 (0.1)	-1.3 (0.1)	264.4 (8.6)	168.1 (8.7)
Dinkum	2005	1.8 (0.1)	-0.9 (0.1)	271.3 (3.9)	169.2 (3.7)
Dinkum	2006	1.9 (0.4)	-0.6 (0.5)	270.3 (22.4)	177.1 (17.5)
Smith	2004	2.1 (0.1)	-0.7 (0.1)	246.1 (3.3)	202.1 (3.5)
Principal solar semi-diurnal S_2 (Period = 12.00 hours)					
Camden	2004	0.4 (0.0)	-0.1 (0.1)	67.5 (9.2)	38.1 (7.4)
Camden	2005	0.4 (0.0)	-0.0 (0.0)	58.2 (8.1)	43.0 (5.7)

Camden	2006	0.4 (0.0)	-0.0 (0.1)	82.2 (8.5)	48.8 (6.2)
Cross	2006	0.6 (0.1)	-0.5 (0.1)	115.6 (17.8)	1.9 (17.0)
Dinkum	2004	0.7 (0.1)	-0.5 (0.1)	67.2 (17.8)	42.8 (19.0)
Dinkum	2005	0.8 (0.1)	-0.4 (0.1)	82.4 (9.1)	39.0 (8.5)
Dinkum	2006	0.9 (0.4)	-0.4 (0.5)	62.1 (37.4)	42.3 (36.4)
Smith	2004	0.9 (0.1)	-0.3 (0.1)	65.1 (8.6)	63.6 (7.8)

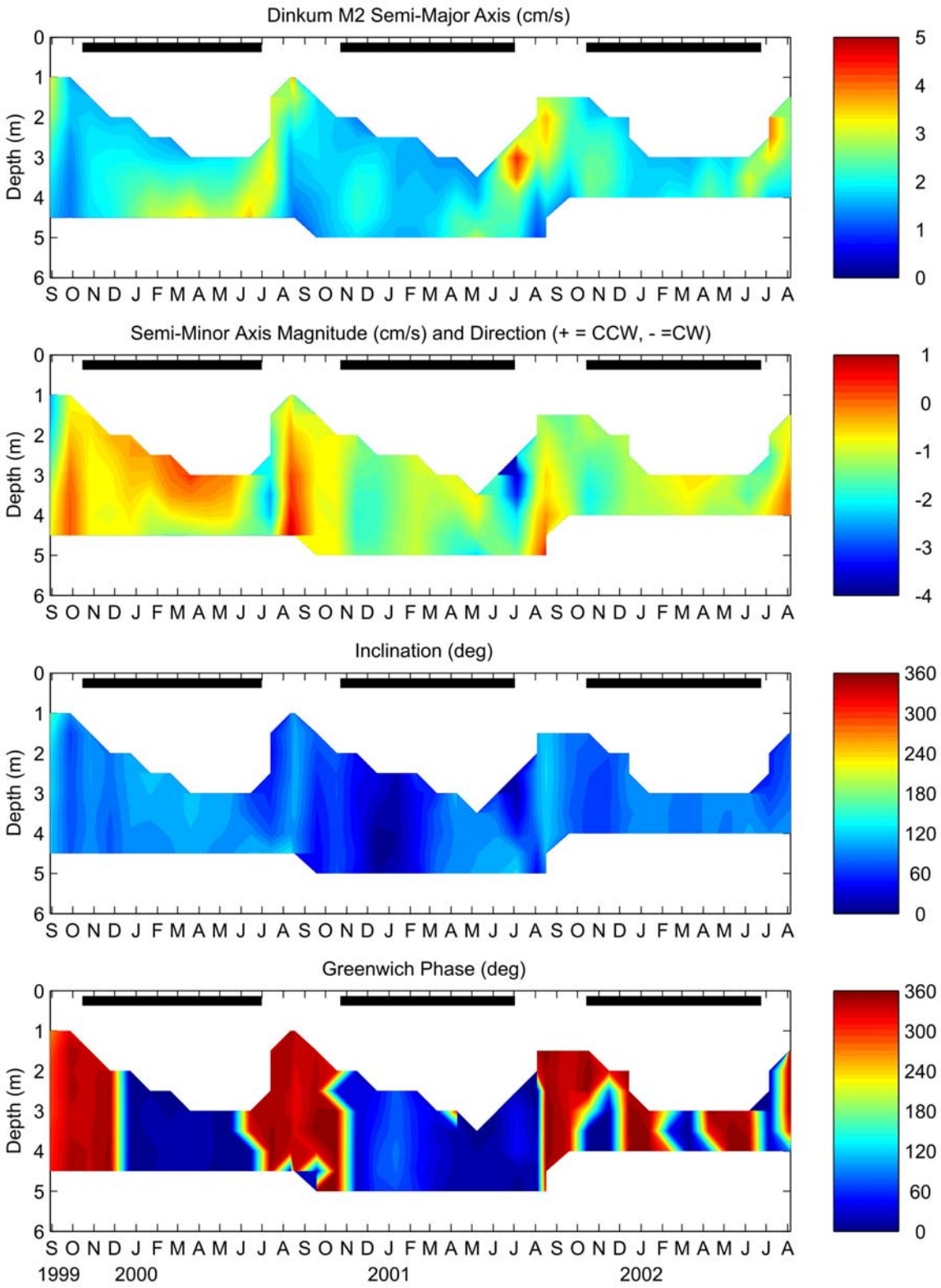

Figure 40. M_2 tidal properties at DINKUM based on 29-day overlapping tidal analyses. The parameters are (from top to bottom) the major axis, minor axis, inclination, and phase. Solid black line indicates landfast ice season.

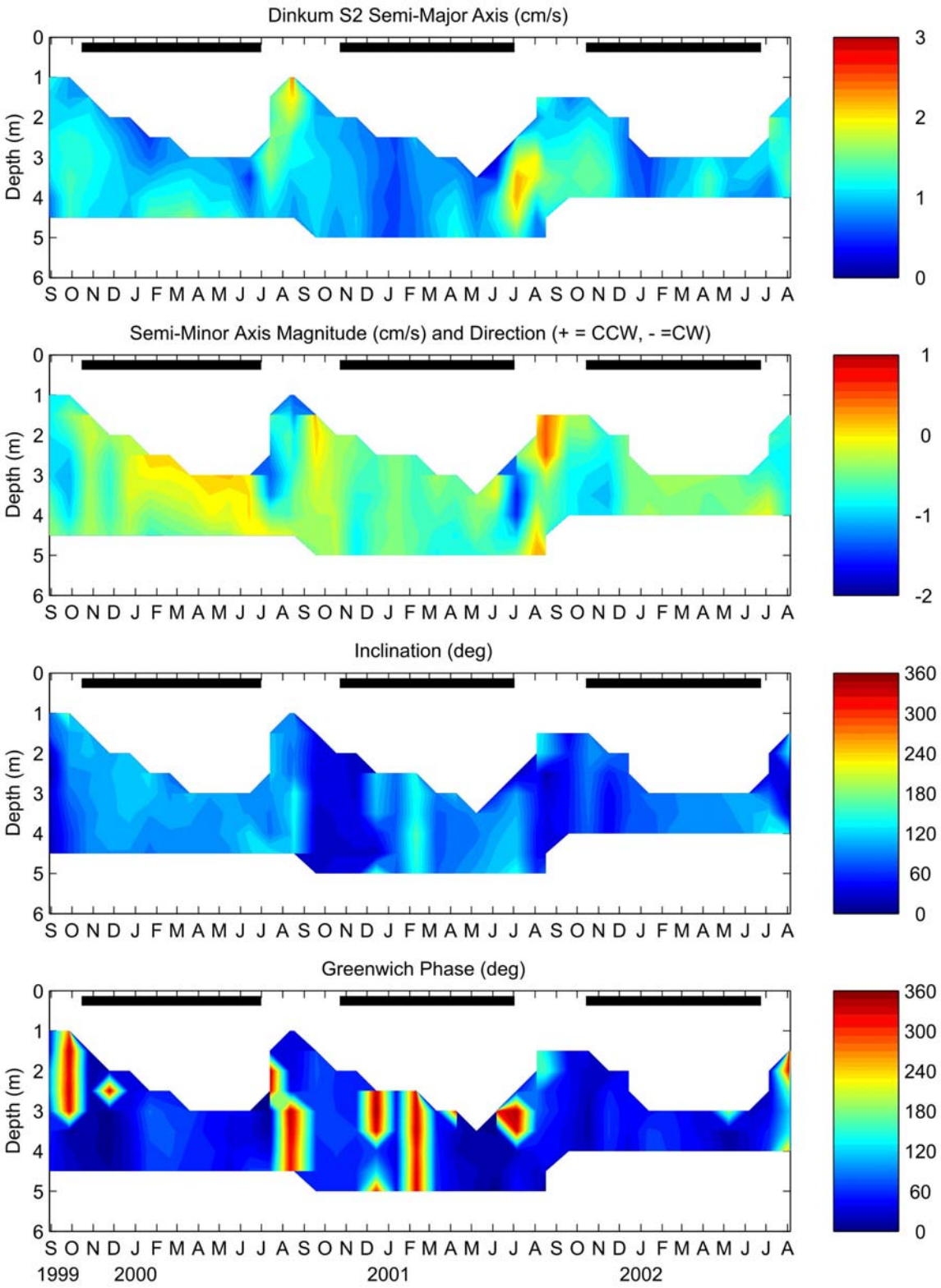

Figure 41. S_2 tidal properties at DINKUM based on 29-day overlapping tidal analyses. The parameters are (from top to bottom) the major axis, minor axis, inclination, and phase. Solid black line indicates landfast ice season.

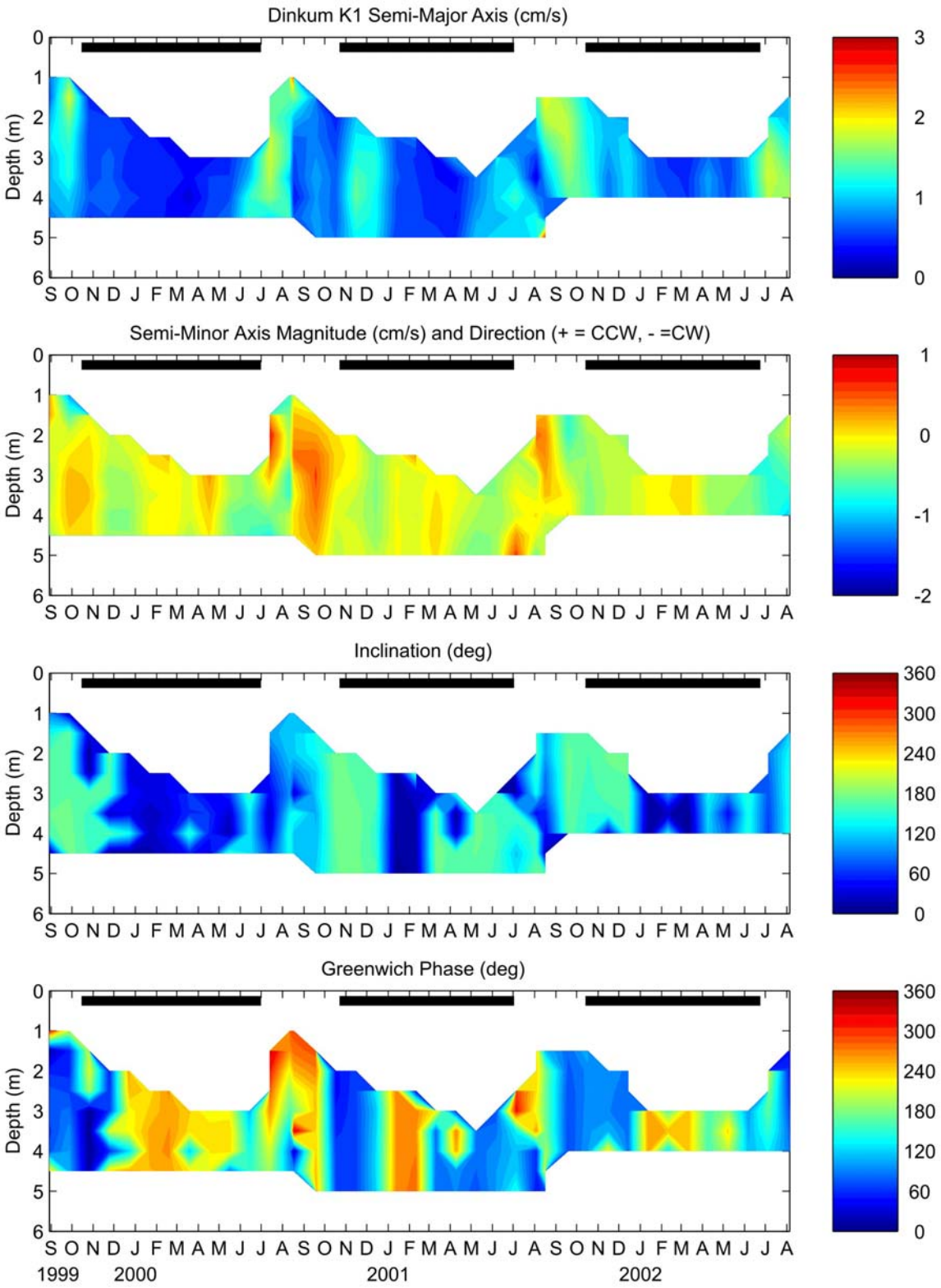

Figure 42. K_1 tidal properties at DINKUM based on 29-day overlapping tidal analyses. The parameters are (from top to bottom) the major axis, minor axis, inclination, and phase. Solid black line indicates landfast ice season.

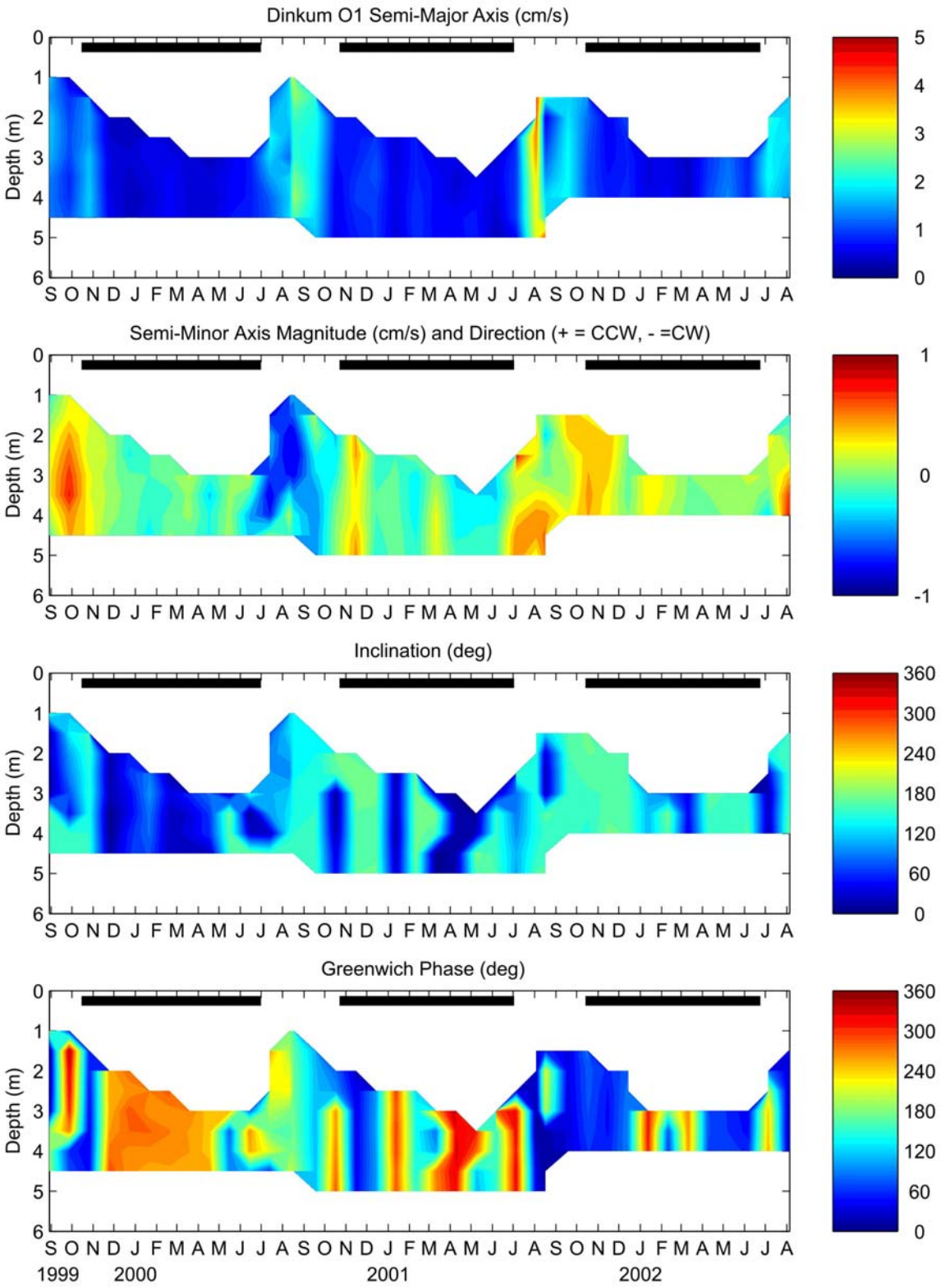

Figure 43. O_1 tidal properties at DINKUM based on 29-day overlapping tidal analyses. The parameters are (from top to bottom) the major axis, minor axis, inclination, and phase. Solid black line indicates landfast ice season.

4. Sea level

Time series of the unfiltered and de-meaned sea level (after correcting for the inverted barometer effect) for all years are shown in **Figures 44 and 45.** Sea-level fluctuations generally range between $\pm$ 0.5 m although the range in sea level varied from a minimum of -2.5 m (October 2006) to a maximum of 1.2 m (August 2000). Sea-level variability, as measured by root-mean-squares are similar for the open-water and landfast ice seasons, ~0.18 m and ~0.15 m, respectively. There are significant annual and semi-annual sea-level variations, which together account for ~30% of the sea-level variance. During Phase I, sea-level was a maximum (+0.2 m) in August and a minimum in April-May (-0.2 m) with a secondary minimum in October-December and a secondary maximum in January-February. For Phase II, sea level was also a maximum in August, but the minima in November-December and April-May were similar in magnitude. The August sea level maximum is consistent with the annual reduction in upwelling-favorable winds (Figure 2; upwelling winds tend to lower coastal sea levels). However, the variations in other months appear to be related to the strength and magnitude of the along-shore wind stress, which varies from year to year. The annual range (~0.4 m) cannot be explained by thermosteric (sea-level changes associated with changes in sea-water density) effects, which we estimate are ~0.07 m. Sea-level fluctuations can vary rapidly over shorter periods. For example, in August 2000 and in late April 2002 sea level rose by ~1 m and then rapidly decreased by more than 1 m over a 10 day period, with both events coincident with rapid reversals in the along-shore wind stress. Similarly, strong northeasterly winds in October 2006 resulted in a large sea level decrease of ~ 2.5 m.

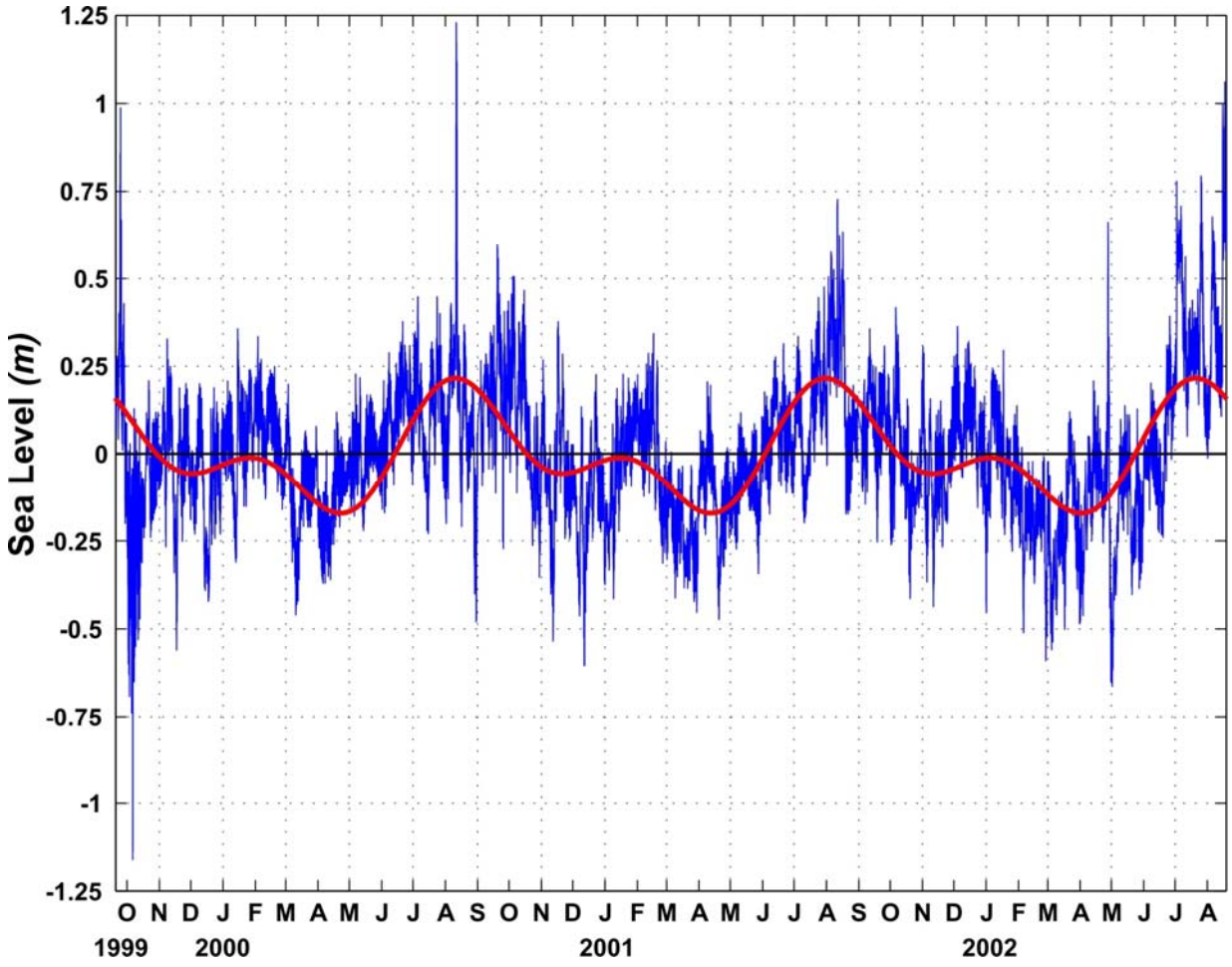

Figure 44. Time series of sea level corrected for the inverted barometer effect from September 1999 – August 2002 (blue line) and the least square harmonic fit to the annual and semi-annual periods (red line).

5. Correlations

We next examine the seasonal relationships among wind stress, currents, and sea level (η) using both correlations (**Tables 21 – 23**), frequency-domain coherence, and dynamical estimates of the terms in linearized along-shelf momentum equation. All correlations are computed after low-pass filtering the currents and sea level time series. Wind stress (rather than wind) is the dynamically important variable and the stresses are computed as:

$$\tau^x = \rho_a C_D W U_W ; \qquad \tau^y = \rho_a C_D W V_W ;$$

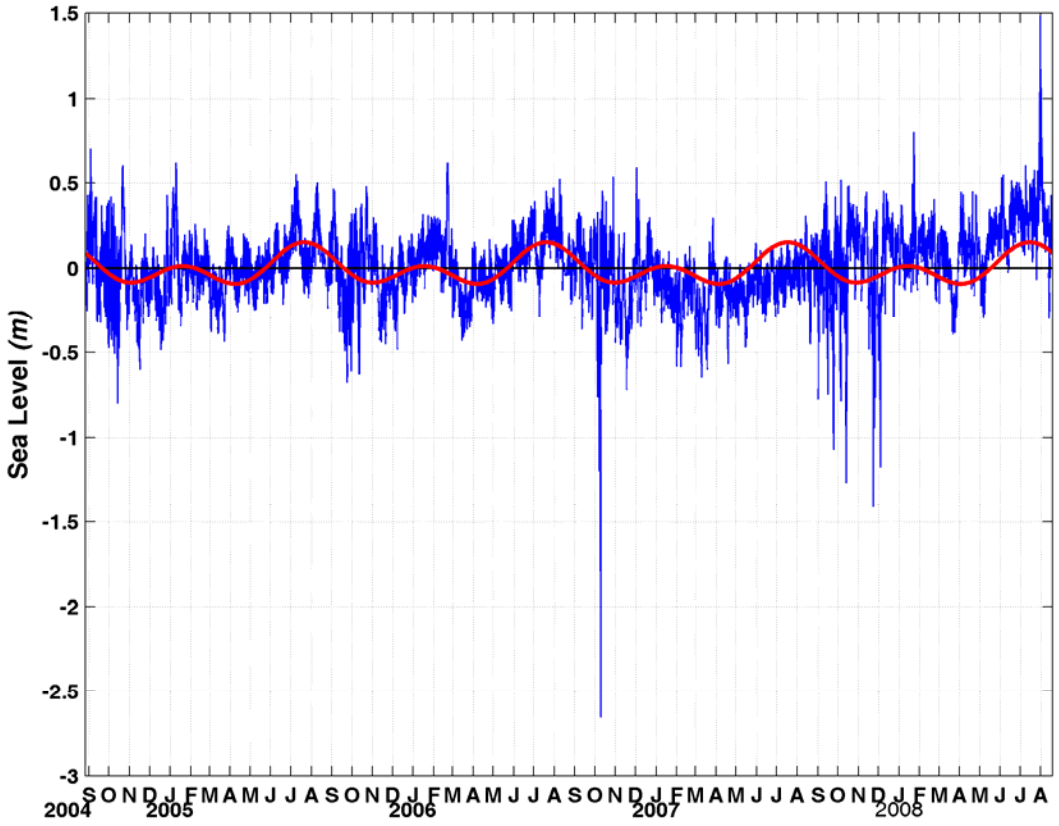

Figure 45. Time series of sea level corrected for the inverted barometer effect from September 2004 – August 2008 (blue line) and the least square harmonic fit to the annual and semi-annual periods (red line).

where $\tau^{x\,(y)}$ is the east-west (x) or north-south (y) component of the stress, ρ_a is the air density, C_D is an open water value for the drag coefficient (2.5 x 10^{-3}), W is the wind speed, and U_W (V_W) is the east-west (north-south) component of the wind velocity. We have also computed the correlations between the wind velocity components and the along-shore currents. Although not shown, these do not differ substantially from those between the stresses and the currents.

Both τ^x (**Table 21**) and η (**Table 22**) are significantly correlated with the along-shore currents at all moorings during the open water season, although the correlations vary amongst sites and years. The differences may be due to record-lengths, interannual differences in wind strength and storm frequency, and water column stratification. The results indicate that the wind

stress and sea-level generally explain only 20 – 50% of the current variance. The signs of the correlations are positive so that an eastward (positive) wind stress or a rise in sea-level is associated with eastward currents and a westward (negative) stress results and/or a sea level set-down coincides with westward currents. Correlations between τ^y and along-shelf currents are small and, in general, not statistically significant. Statistically significant positive correlations are found between τ^x and η during the open water period (**Table 23**) with the sign of the correlation consistent with eastward (downwelling-favorable) winds inducing a sea-level set-up (increase) and westward (upwelling-favorable) winds leading to a sea level decrease during the open water season.

Table 21. Open-water period wind-current correlations. (Italicized entries indicate statistical significance at the $\alpha < 0.05$ level.).

Mooring	**Time Period**	***r*: (τ^x vs U_r)**	***r*: (τ^y vs U_r)**
Argo	6/30 – 10/20/00	*0.68*	0.13
Argo	7/4 – 10/13/01	*0.50*	*0.33*
Argo	6/30 – 8/19/02	*0.50*	0.16
Dinkum	6/30 – 10/22/00	*0.71*	0.16
Dinkum	7/2 – 10/13/01	*0.54*	*0.31*
Dinkum	6/23 – 8/19/02	*0.52*	0.09
McClure	6/30 – 10/22/00	*0.65*	0.16
McClure	7/2 – 8/31/01	*0.58*	*0.34*
Reindeer	6/27 – 8/19/02	*0.53*	0.15
Camden	8/26 - 10/29/04	*0.74*	0.37
Camden	7/6 - 10/25/05	*0.78*	0.18
Camden	6/27 - 10/31/06	*0.63*	-0.08
Camden	6/28 - 9/18/07	*0.59*	0.20
Cross	7/3 - 9/26/07	*0.44*	0.13
Dinkum	8/25 - 10/27/04	*0.72*	0.31
Dinkum	7/5 - 10/25/05	*0.65*	0.23
Dinkum	6/28 - 10/9/06	*0.56*	0.08
Smith	8/29 -10/27/04	*0.71*	0.31

Table 22. Open-water period current-sea level correlations. (Italicized entries indicate statistical significance at the $\alpha < 0.05$ level.)

Mooring	Time Period	*r*: (η vs U_r)
Argo	6/30 – 10/20/00	*0.66*
Argo	7/4 – 10/13/01	*0.45*
Argo	6/30 – 8/19/02	*0.73*
Dinkum	6/30 – 10/22/00	*0.67*
Dinkum	7/2 – 10/13/01	*0.49*
Dinkum	6/23 – 8/19/02	*0.69*
McClure	6/30 – 10/22/00	*0.61*
McClure	7/2 – 8/31/01	*0.46*
Reindeer	6/27 – 8/19/02	*0.71*
Camden	6/27/06-10/31/06	*0.50*
Camden	6/28/07-9/18/07	*0.51*
Camden	7/6/05-10/25/05	*0.57*
Camden	8/26/04-10/29/04	*0.54*
Cross	7/3/07-8/18/08	*0.43*
Dinkum	6/28/06-10/9/06	*0.4*
Dinkum	7/5/05-10/25/05	*0.63*
Dinkum	8/26/04-10/27/04	*0.62*
Smith	9/13/03-10/27/04	*0.57*

Table 23. Open-water period wind-sea level correlations. (Italicized entries indicate statistical significance at the $\alpha < 0.05$ level.)

Mooring	Time Period	*r*: (τ^x vs η)
Dinkum	6/30/00-10/22/00	*.61*
Dinkum	7/2/01-10/13/01	*.53*
Dinkum	6/23/02-8/19/02	*.49*
Camden	8/26/04-10/29/04	*.45*
Camden	7/6/05-10/25/05	*.47*
Camden	6/27/06-10/31/06	*.58*
Camden	6/28/07-9/18/07	*.41*
Cross	7/3/07-8/18/08	*.48*
Dinkum	6/28/06-10/9/06	*.54*
Dinkum	7/5/05-10/25/05	*.55*
Dinkum	8/26/04-10/27/04	.37
Smith	9/13/03-10/27/04	.38

In contrast to the open water season, there is no statistically significant correlation between along-shore currents and τ^x, τ^y (**Table 24**), or η (**Table 25**) during the landfast ice period. However, τ^x and η are significantly correlated at this time (**Table 26**), but the magnitude of these correlations are about half those of the open water season.

Table 24. Landfast ice season wind-current correlations. (None are statistically significant at the $\alpha < 0.05$ level.)

Mooring	Time Period	*r*: (τ^x vs U_r)	*r*: (τ^y vs U_r)
Argo	10/15/99 – 6/30/00	-0.01	0.09
Argo	10/20/00 – 7/4/01	-0.06	0.21
Argo	10/13/01 – 6/30/02	0.11	0.15
Dinkum	10/15/99 – 6/30/00	0.07	0.11
Dinkum	10/20/00 – 7/4/01	-0.04	.21
Dinkum	10/13/01 – 6/23/02	0.10	0.14
McClure	10/15/99 – 6/30/00	-0.06	0.05
McClure	10/20/00 – 7/4/01	-0.05	0.17
Reindeer	10/10/01 – 6/27/02	0.12	0.14
Camden	10/29/04- 7/6/05	-0.37	-0.17
Camden	10/25/05- 6/27/06	-0.32	-0.03
Camden	10/31/06- 6/28/07	-0.15	0.19
Dinkum	10/27/04- 7/5/05	0.08	0.09
Dinkum	10/25/05- 6/28/06	-0.01	0.07
Cross	11/22/06- 7/3/07	0.29	0.2
Smith	10/27/04- 7/5/05	-0.03	0.06

Table 25. Landfast ice season sea-level-current correlations. (None are statistically significant at the $\alpha < 0.05$ level.)

Mooring	Time Period	R: (η vs U_r)
Argo	99/10/15 – 00/6/30	0.07
Argo	00/10/20 – 01/7/4	0.12
Argo	01/10/13 – 02/6/30	0.12
Dinkum	99/10/15 – 00/6/30	0.15
Dinkum	00/10/20 – 01/7/4	0.13
Dinkum	01/10/13 – 02/6/23	0.09
Dinkum	6/28/06-10/9/06	0.18
Dinkum	7/5/05-10/25/05	0.01
McClure	99/10/15 – 00/6/30	-0.01
McClure	00/10/20 – 01/7/4	0.09
Reindeer	01/10/10 – 02/6/27	0.07
Camden	10/29/04-7/6/05	-0.5
Camden	10/31/06-6/28/07	-0.22
Camden	10/25/05-6/27/06	-0.14
Cross	11/2206 – 7/3/07	0.51
Dinkum	10/27/04-7/5/05	0.01
Dinkum	10/25/05-6/28/06	0.18
Smith	9/13/03-10/27/04	0.14

Correlations between along-shore currents and the zonal component of the geostrophic wind at 72.5^oN, 147.5^oW from National Center for Environmental Prediction (NCEP) forecast models

were also computed. These were non-significant during the landfast ice period, but significant during the open water period. The correlation between along-shore currents and the Deadhorse-Pt. Barrow atmospheric pressure difference was significant (r ~ .26) in both seasons, although this correlation explains <10% of the current variance.

Table 26: Landfast Ice season winds and sea level correlation:

Mooring	**Time Period**	***r:*** **(τ^x vs η)**
Dinkum	10/15/99 – 6/30/00	*0.25*
Dinkum	10/22/00 – 7/2/01	*0.28*
Dinkum	10/13/01 – 6/23/02	*0.32*
Camden	10/29/24-7/6/05	*0.56*
Camden	10/25/05-6/27/06	*0.34*
Camden	10/31/06-6/28/07	*0.26*
Cross	11/22/06-7/3/07	*0.37*
Dinkum	10/27/04-7/5/05	*0.49*
Dinkum	10/25/05-6/28/06	*0.26*
Smith	10/27/04-7/5/05	*0.60*

The absence of a significant wind-current correlation contrasts with *Aagaard's* [1984] suggestion that currents on the inner shelf were correlated with the winds during the landfast ice period. His conclusion, however, was based on visual inspection of wind and current records from two 3-week current meter records collected under the landfast ice in water depths of 27 and 38 m, approximately 35 km northeast of the DINKUM mooring. The reason for this is not clear although his measurements might have coincided with a period when winds and currents were roughly correlated and such periods can be found upon inspection over portions of our data set.

We have also examined the along-shore coherence and phase relationships between ocean bottom pressure at Camden, Prudhoe, and Smith bays for the landfast ice season. Bottom pressure variations are coherent and in-phase at most periods between Camden and Prudhoe bays (**Figure 46a**), which are separated by about 120 km. Pressure fluctuations at periods >9 days are also coherent and in-phase between Prudhoe and Smith (235 km separation; **Figure 46b**) and Camden and Smith (355 km separation; **Figure 46c**) bays, but degrades at shorter periods.

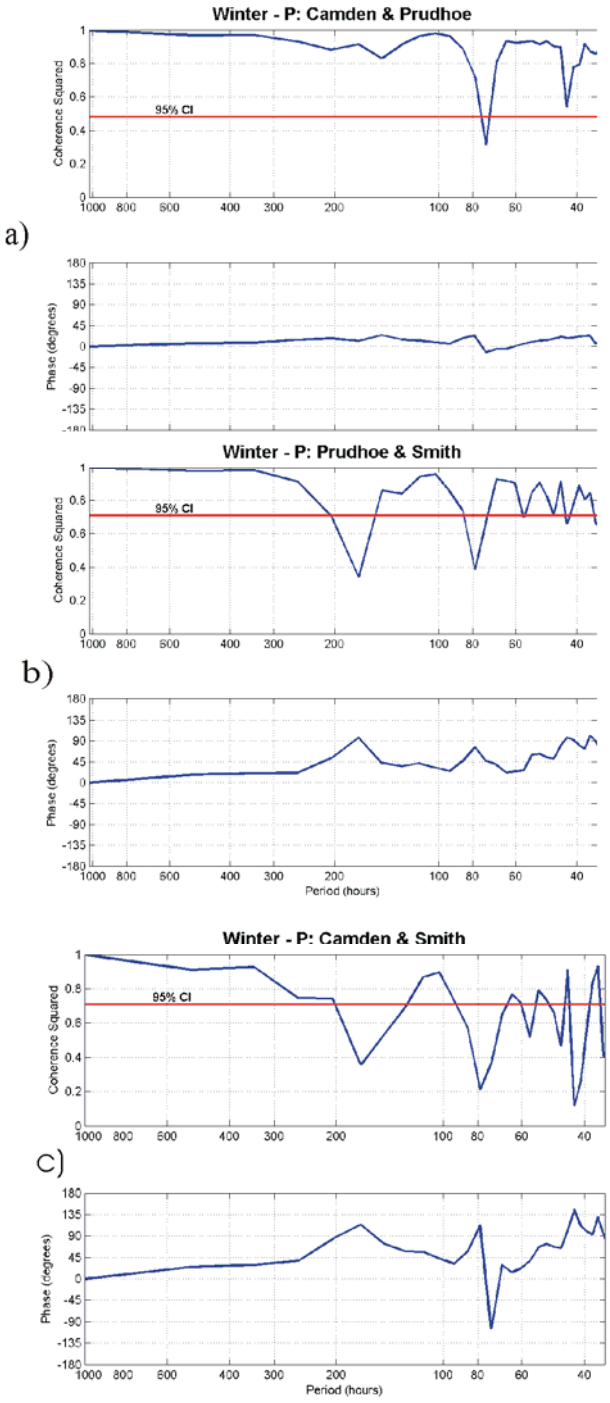

Figure 46. Coherence squared and phase in bottom pressure between **a**) Camden and Prudhoe bays, **b**) Prudhoe and Smith bays, and **c**) Camden and Smith bays.

We find that the along-shore velocity (U) at Prudhoe Bay is coherent and nearly out-of-phase with the pressure difference between Smith and Camden bays (**Figure 68)**. This result,

which we examine in more detail in the next section, implies that along-shore pressure gradients are important components of the along-shore momentum balance during the landfast ice season.

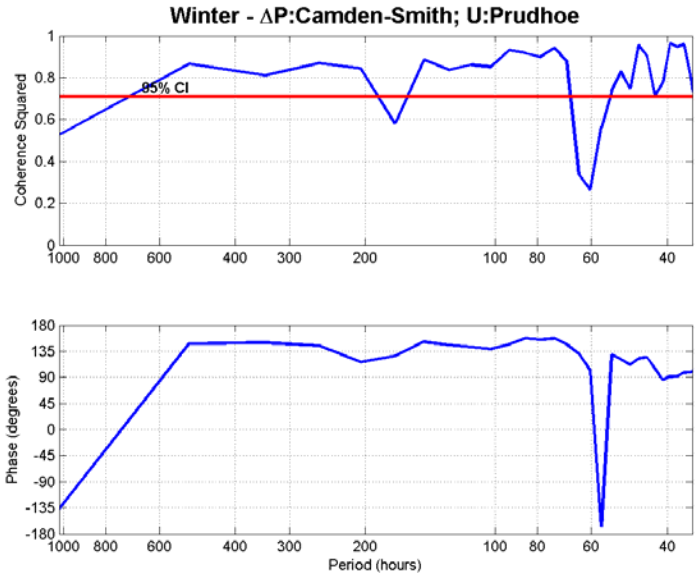

Figure 47. Coherence squared and phase between differences in bottom pressure between Camden and Smith bays and the along-shore velocity at Prudhoe.

6. Dynamics

We next examine the vertically integrated along-shore momentum balance at subtidal time scales for both the landfast and open water seasons using data from the moorings and wind stresses as calculated above. The vertically integrated, linearized, along-shore momentum equation is:

$$\underset{(a)}{\frac{\partial U}{\partial t}} = \underset{(b)}{-g\frac{\partial \eta}{\partial x}} + \underset{(c)}{\frac{\tau_s^x}{\rho H}} - \underset{(d)}{\frac{\tau_b^x}{\rho H}} \qquad (2)$$

where U is the vertically averaged along-shore velocity component, g the gravitational acceleration, H the water depth, ρ the density, and τ^x the stress in the along-shore direction. The subscripts "s" and "b" refer to the stress at the surface and bottom, respectively. The equation states that local accelerations in along-shore velocities (term a) are balanced by the along-shore

pressure gradient arising from the along-shore sea level slope (term b) and the vertically integrated effects of surface (term c) and bottom stresses (term d). The bottom stress (τ_b^x) is often parameterized by a linear stress law, $\tau_b^x = \rho r U$, with r, the resistance coefficient being~10^{-4} m-s^{-1} [*Csanady*, 1981; *Lentz*, 1994]. We assumed that the non-linear terms in this force balance are small and we have neglected the effects of wave radiation stresses. The latter arise due to surface gravity waves propagating obliquely onshore and these stresses can be a substantial momentum source in shallow water (<5m) during storms [*Lentz et al.,* 1999]. Although wave radiation stresses are absent during the landfast ice period, they might be important during the open water period especially when waves are large. These stresses are probably small in general because the energy of onshore propagating waves is probably dissipated (to some extent) along the barrier islands and shoals girding the offshore boundary of Stefannsson Sound. However, they may become a more important aspect of the nearshore momentum balance with changes in the sea ice cover. More extensive open water in summer and fall will increase fetch and thus generate larger waves especially if landfast ice formation is delayed, as anticipated with a gradually warming climate.

In summer, τ_s^x is the surface wind stress, whereas in winter it arises due to frictional coupling between the ocean and the underside of the immobile landfast ice. Consequently, both the sea bottom and the underside of the ice exert a frictional stress against the along-shore flow during the landfast ice season, whereas during the open water season bottom and surface stresses oppose one another. For present purposes we assume that the underice stress can be parameterized in the same manner as the bottom stress, e.g. ($\tau_b^x = \tau_s^x = \rho r U$) with $r \sim 10^{-4}$ m-s^{-1} for both friction coefficients. Our choice of r for the resistance coefficient between ice and water might not be valid as discussed below. However, in the absence of the necessary observations,

we assume that it is of the same magnitude as the bottom resistance coefficient. With this assumption, the along-shore momentum balance for the landfast ice sea is a modified equation 1:

$$\frac{\partial U}{\partial t} = -g\frac{\partial \eta}{\partial x} - \frac{2rU}{H} \qquad \textbf{(3)}$$

We computed all terms in equations 1 and 2 except the along-shore sea level slope, which is estimated as the residual. The results are shown using data from DINKUM for the 00 and 01 open water seasons (**Figures 48 and 49**) and for the 2000-01 and 2001-02 landfast ice seasons at DINKUM (**Figures 50 - 51**). Results using other moorings are similar and thus not shown.

In both seasons balance is primarily achieved among the stresses and along-shelf pressure gradient, with the local acceleration term ($\partial U / \partial t$) typically being 10^{-6} or smaller and thus an order of magnitude smaller than the other terms. In both seasons the along-shelf pressure gradients imply along-shore sea level slopes of $\pm$5 to $\pm$10 cm/100 km. If these slopes extend the entire length of the Alaskan Beaufort coast then the sea level difference between Barrow and the US-Canada boundary can be as large as 0.5 m, which is easily detected with pressure gauges. The average along-shore velocity over the landfast ice period is virtually negligible implying that the there is no mean sea level slope during this season. In general, the along-shelf sea level gradients are about twice as large during the

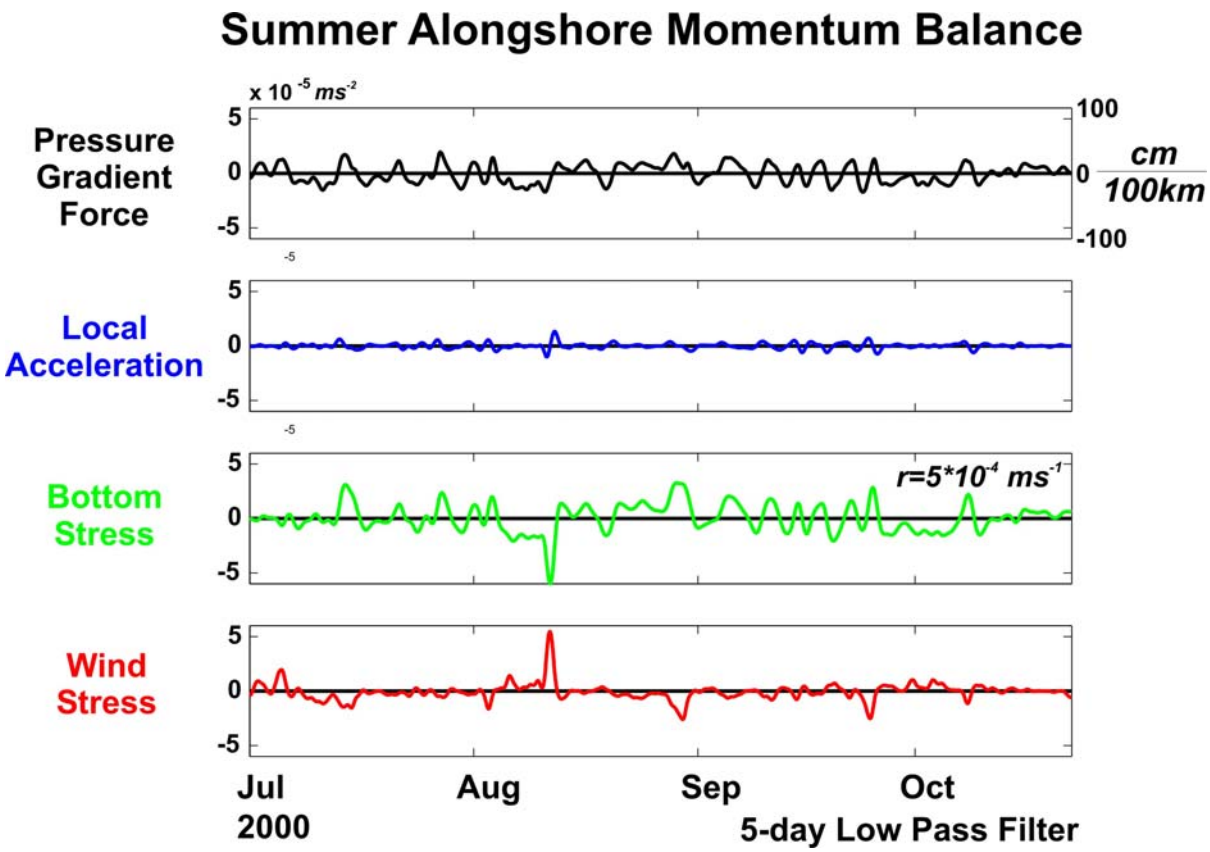

Figure 48. Time series of the terms in the vertically integrated along-shelf momentum equation for the 2000 open water season using data from DINKUM.

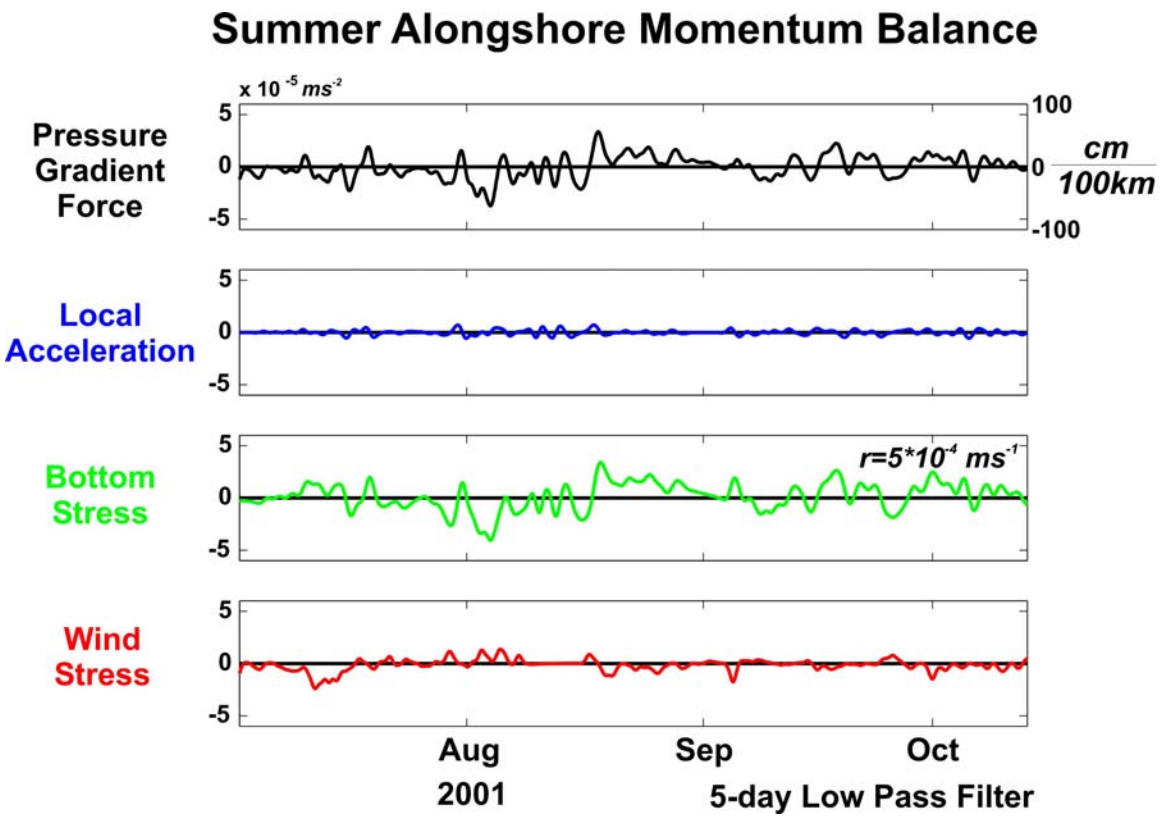

Figure 49. Time series of the terms in the vertically integrated along-shelf momentum equation for the 2001 open water season using data from DINKUM.

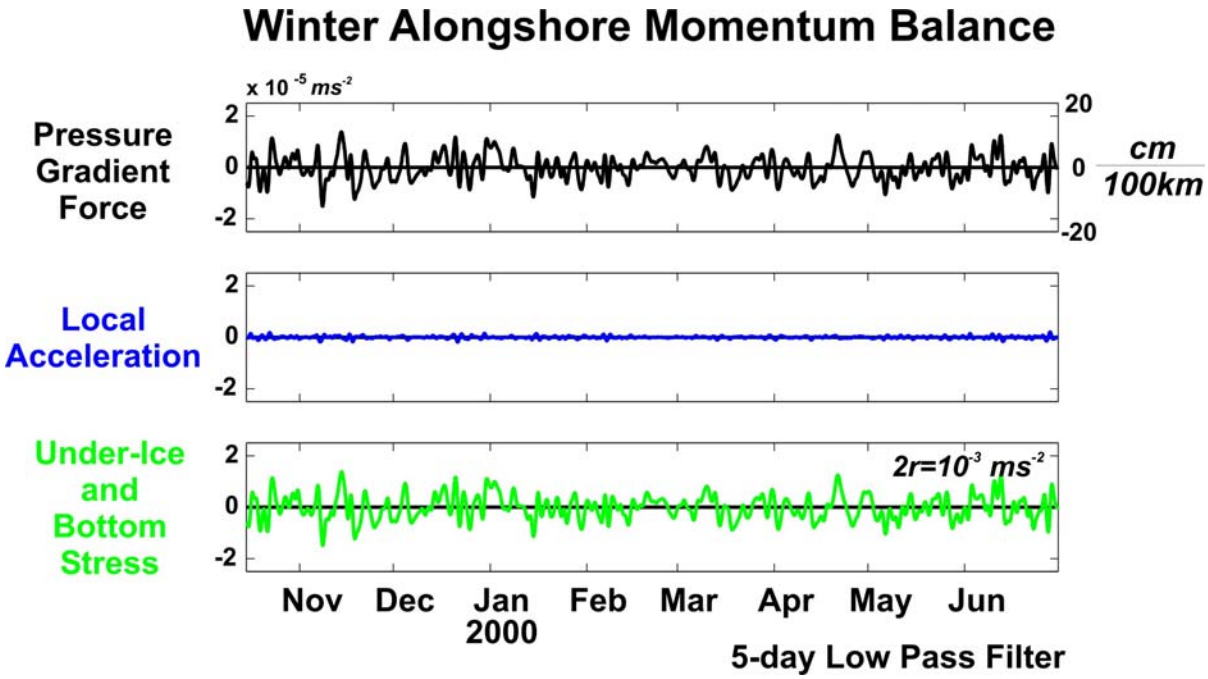

Figure 50. Time series of the terms in the vertically integrated along-shelf momentum equation for the 2000 – 01 landfast ice season using data from DINKUM.

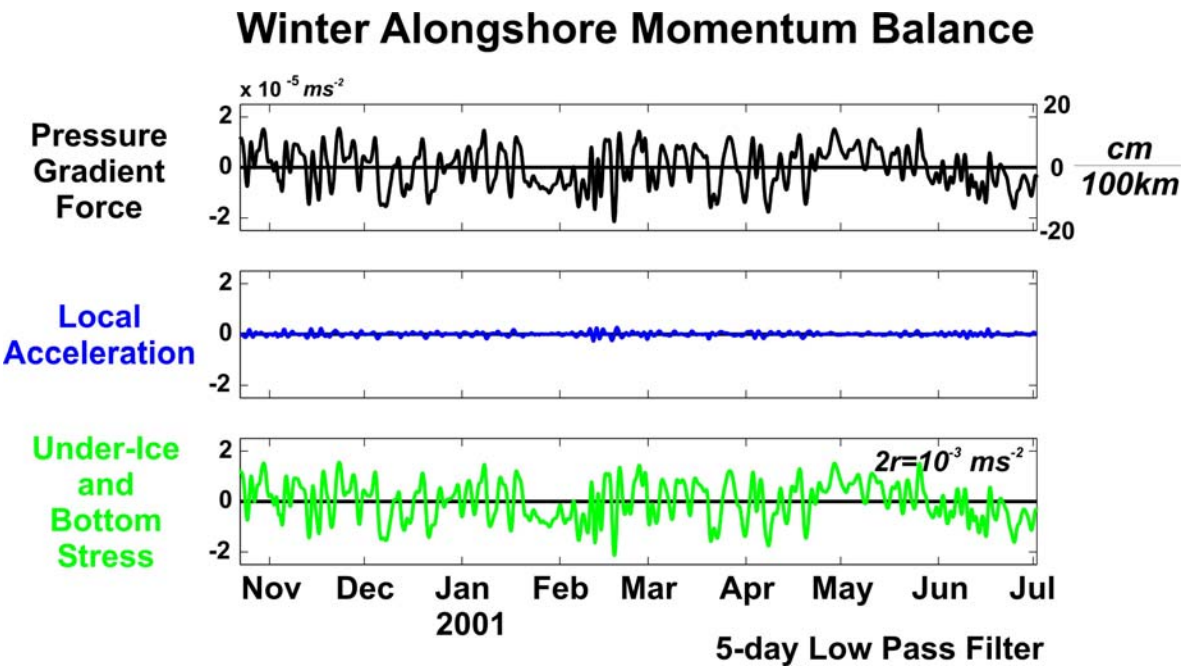

Figure 51. Time series of the terms in the vertically integrated along-shelf momentum equation for the 2001 – 02 landfast ice season using data from DINKUM.

open water season than during the landfast ice period. We emphasize that the estimates of the winter along-shore sea-level gradients are uncertain, however, because of uncertainty in the ice-water frictional coupling.

Note however, that equation 2 implies that the presence of sub-tidal underice flows requires an along-shore sea level slope. How these slopes originate is not clear, however, although several possibilities exist. First, sea level fluctuations might be induced on the western shelf near Barrow due to variations in the coastal current that drains the Chukchi Sea through Barrow Canyon [*Weingartner et al*., 1998; *Weingartner et al.,* 2005]. If this were the primary forcing for the underice flows, we would expect a stronger correlation between the underice currents and the NCEP wind fields, since currents in the Chukchi Sea are strongly correlated with these winds [*Weingartner et al.*, 1998; accepted]. We would also expect that the variance in current and along-shore sea level would be greater in late fall-early winter than in late winter as these authors found for the flow in Barrow Canyon. Second, fluctuating along-shore coastal sea-

level gradients can be established by time-varying divergences in the along-shelf wind field. Third, spatial variations in the underice friction associated with the complex deformation field of the sea ice might establish cross-shelf flows that alter the along-shelf pressure field [*Trowbridge et al.,* 1998]. Finally, remotely forced continental shelf waves could also affect the along-shore pressure gradient. These waves would be forced by wind stress variations to the west of our measurement site. However, the lack of a significant correlation between local or remote winds and the underice flow argues against this reason.

Under a separate proposal, we have been investigating the dynamics of the underice flow using simply-forced, idealized three-dimensional circulations models of the landfast ice zone subjected to an along-shore wind stress offshore of the landfast ice domain. Some of these results shed light on our observations hence here we outline the modeling approach and present some preliminary findings of this activity.

We use the Regional Ocean Model System (ROMS; *Song and Wright*, 1998; *Shchepetkin and McWilliams*, 2005) for the experiments. ROMS is a finite difference, free surface model which uses stretched, terrain following coordinates in the vertical (*s*-coordinate, *Song and Haidvogel*, 1994). The *s*-coordinate model is desirable when dealing with continental shelf topography and allows for increased resolution in the top and bottom boundary layers. It incorporates the Mellor-Yamada level 2.5 (*Mellor and Yamada*, 1982) mixing scheme, where eddy diffusivity is calculated based upon the local flow and stratification.

Several simplifications are involved in our modeling study. First, we ignore ice dynamics/thermodynamics. Instead, landfast ice enters the model experiments only through the ice-water stress representation and by prescribing the distance from the coast to the offshore boundary where wind stress directly affects the ocean. This simplification circumvents the need

to couple complex nearshore ice physics to the ocean model. For the Alaskan Beaufort shelf setting, wind stress is applied to the ocean surface outside of the landfast ice domain, which extends to the 20 m isobath or ~20 km offshore in our experiments. Second, we employ a bathymetry that mimics the Alaskan Beaufort shelf bottom slope (10^{-3}) and depths. We ignore along-shore variations in topography and coastline orientation as this seems appropriate given the relatively simple bathymetry and nearly straight coastline of the ABS. These simplifications ensure that the modeled flows result only from physical processes associated with the imposed boundary conditions or underice stress parameterizations. **Figure 52** is a schematic of the model domain.

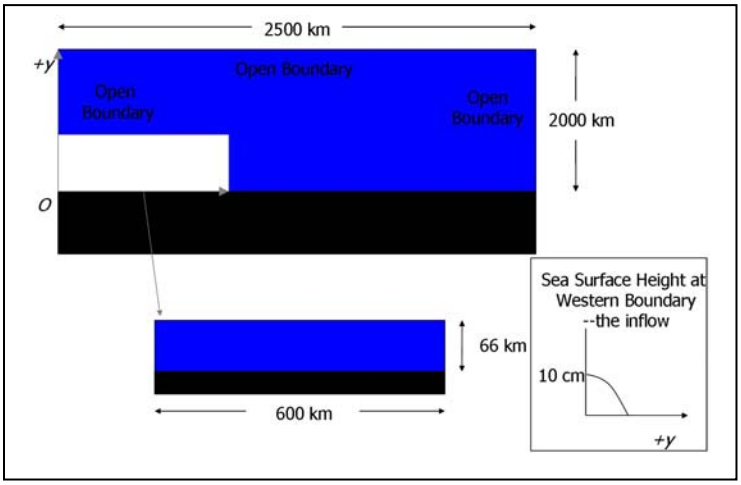

Figure 52. Schematic of the numerical model domain. The 600 km "box" shown in the inset is the modeled region of interest and includes a 20 km wide band of landfast ice adjacent to the coast.

The model domain consists of a 600 km long shelf, oriented east-west, with a coastal wall at the southern boundary and with open boundary conditions elsewhere. Test runs show that this set-up works well for experiments involving only wind stress and inflows at either end of the channel.

We first examine horizontal circulation field that evolves in response to a spatially uniform, westward (upwelling-favorable) alongshore wind of 7 m s^{-1}, which is typical of the ABS in winter. The model is allowed to evolve from a state of rest to steady state after the winds

are "switched on". Bottom friction and ice-water friction are included via a linear drag law, (e.g., alongshore bottom friction = $\rho r_b U$ and alongshore ice-water friction = $\rho r_i U$, where r_b is the bottom friction coefficient, r_i is the ice-water friction coefficient, ρ is seawater density, and U is the alongshore current speed. Analogous expressions are written for the cross-shore stresses, with V, the cross-shore velocity, replacing U in the above.) In the following experiment we choose $r_i = r_b = 10^{-4}$ m s^{-1}. Figure XX shows the cross-shore sea level setup and the along- and cross-shore velocity fields in the landfast ice zone. At steady state the sea-level has decreased at the coast (by about 1 m) and slopes downward offshore by ~0.5 cm and is a minimum at the edge of the landfast ice. The cross-shore sea level slope is 0.5 cm/20 km or -2.5 x 10^{-7}. This slope geostrophically balances an *eastward* (hence upwind) flow beneath the landfast ice. The underice alongshore flow speeds range from 1 – 5 cm s^{-1} but is strongest at the ice edge and weakens upon approaching the coast. Offshore of the landfast ice the sea level slopes steeply (only partially shown in the figure) and supports a strong downwind jet at the ice edge. Beneath the landfast ice the cross-shore velocity field is very weak (~0.5 cm s^{-1}) and consists of offshore boundary layer flows beneath the ice and at the bottom, and an onshore flow distributed over the interior of the water column.

The mechanism for the counter current is the curl in the surface stress at the ice edge (the curl arises because of the abrupt change from no surface wind stress to strong surface wind stress at the ice edge) and the coastal boundary constraint of no inflow at the coast. Under westward winds, strong upwelling develops at the ice edge, which leads to a decrease in sea-level beneath the landfast ice. The sea-level decrease is not uniform across the shelf, but is a maximum at the ice-edge and smallest at the coast, thus giving rising to a cross shore sea level slope under the ice. The results from this simple model predict that the underice circulation should be anti-

correlated with the along-shore winds, while sea level variations should be correlated with these winds.

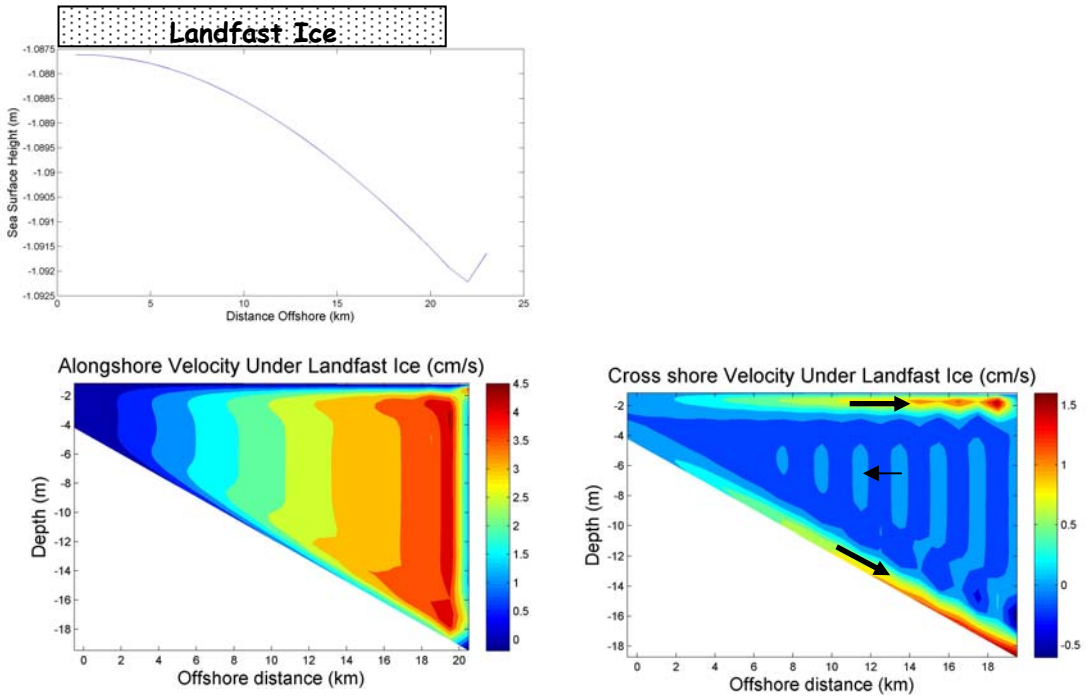

Figure 53. Steady-state model results of underice sea-level and circulation subject to a westward (into page) wind stress offshore of the landfast ice-edge. The upper left panel shows the underice sea-level distribution, the lower left panel shows the along-velocity (positive is eastwards our out of the page), and the lower right panel shows the cross-shore currents.

In contrast the observations yielded no significant correlation between the underice currents and the winds but a weak, albeit significant, positive correlation between sea level and winds. Nevertheless there is some observational support for these simple model predictions based on the CROSS current meter data as we next discuss.

Before presenting these data we show a series of Synthetic Aperture Radar (SAR) images (Figure 54) collected at 1 – 5 day intervals between November 11 and December 22. Included in each image is the location of the Cross Island (yellow dot) mooring and the approximate location of the landfast ice edge (red line). That location was determined subjectively by having two analysts working independently to examine feature displacements between successive pairs of

images. The imagery shows the seaward advance of the landfast ice edge, which covered the mooring shortly after November 22, based upon the bottom track record from the mooring (discussed below). The landfast ice then retreated inshore of the mooring between Dec. 2 – 9, and then advanced seaward afterwards. By December 13 the edge of the landfast ice was approximately 15 km seaward of the mooring (35 km offshore of the coast), where it remained until at least December 22.

Figure 55 shows time series from September 1 through December 31, 2006 of the along-shore winds, along-shore currents, and the bottom-tracking record. We use both the bottom-track record and the SAR images to gauge when landfast ice covers the mooring. From early Sept. 1 – 15, a band of loose ice covered the mooring, but from Sept. 15th through Nov. 22, the mooring was not covered by any ice and currents vary coherently with the winds. Landfast ice began to develop in late October and expanded

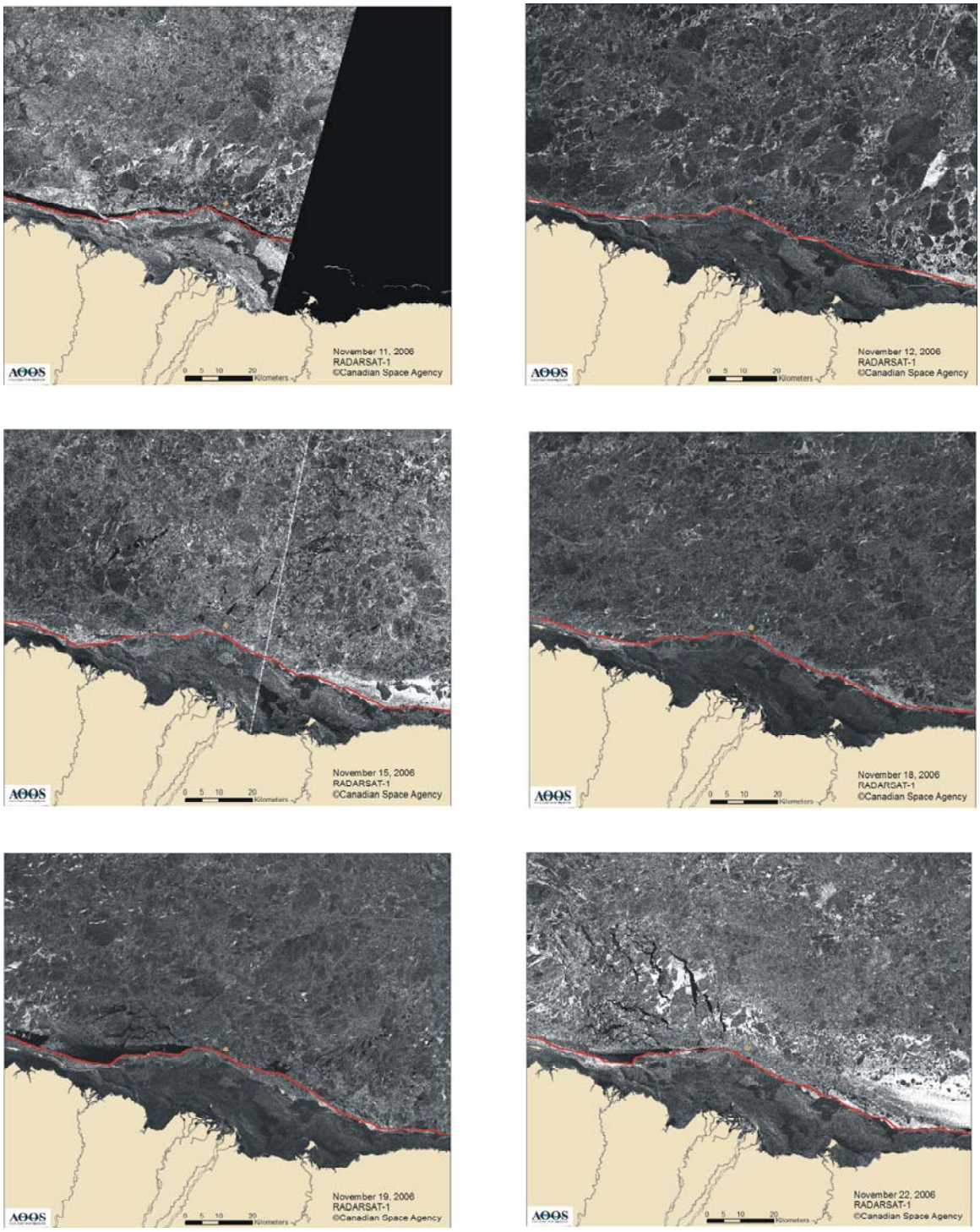

Figure 54. Time series of SAR imagery of the landfast and pack ice over the ABS from November 11 through November 22, 2006. Red line outlines edge of the landfast ice zone. Yellow dot shows the location of the Cross Island mooring.

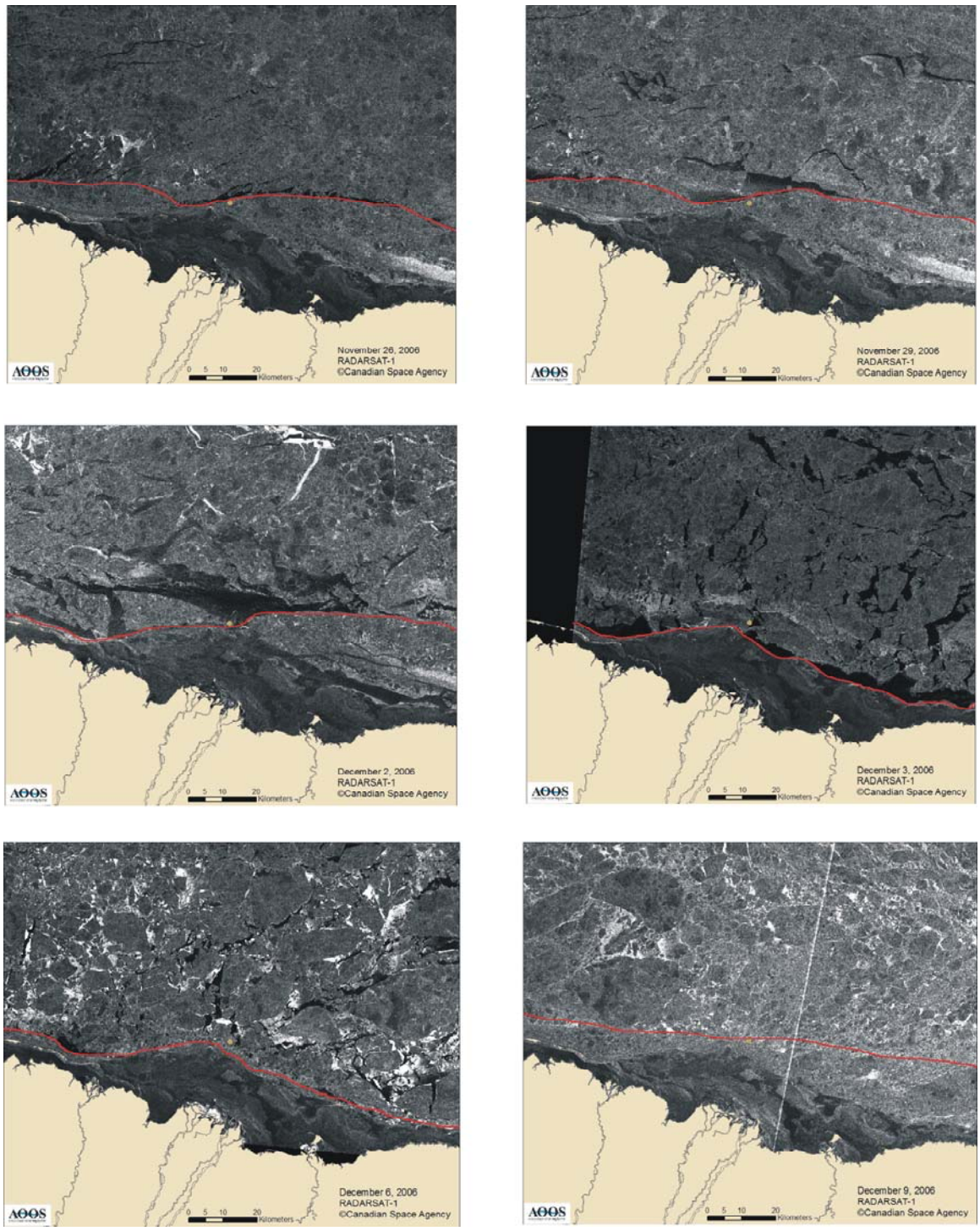

Figure 54 (continued). Time series of SAR imagery of the landfast and pack ice over the ABS from November 26 through December 9, 2006. Red line outlines edge of the landfast ice zone. Yellow dot shows the location of the Cross Island mooring.

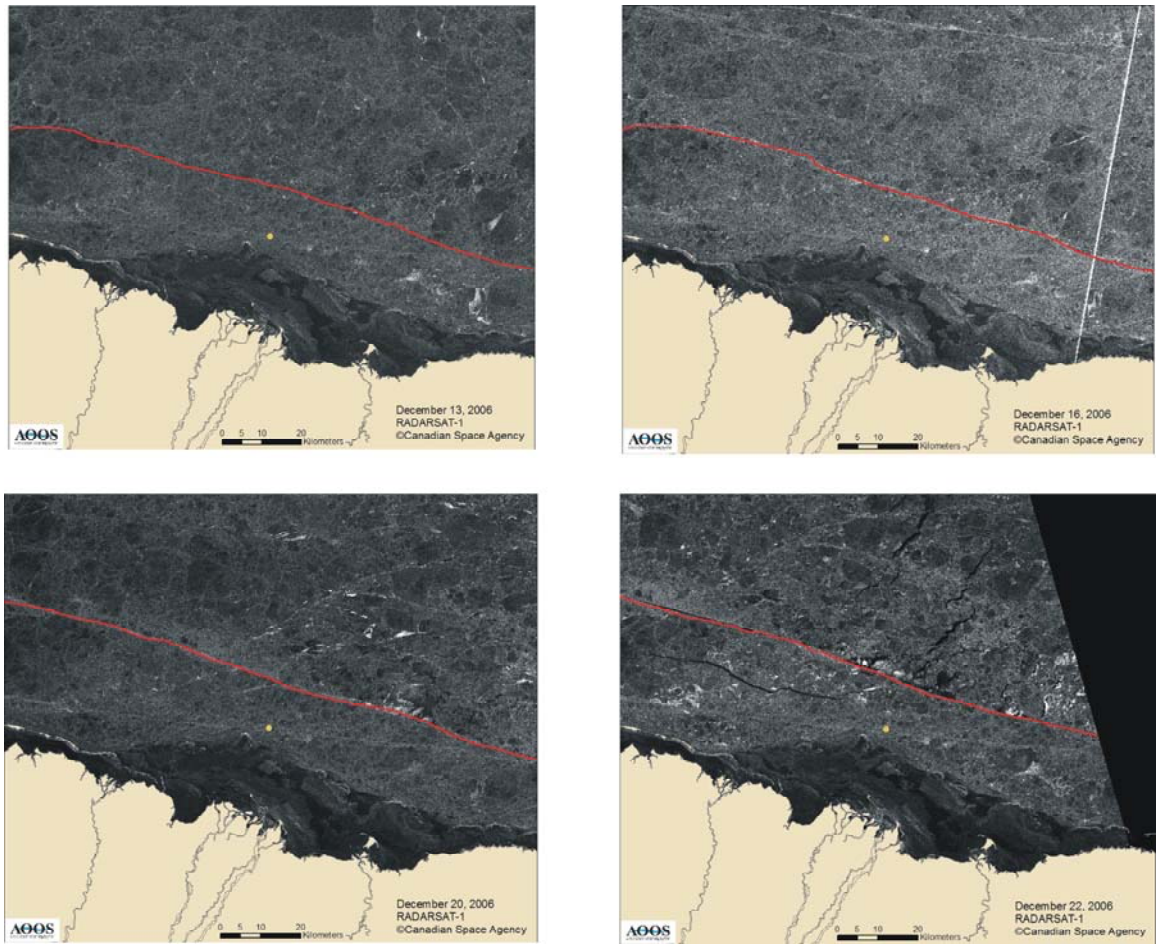

Figure 54 continued. Time series of SAR imagery of the landfast and pack ice over the ABS from December 13 through December 22, 2006. Red line outlines edge of the landfast ice zone. Yellow dot shows the location of the Cross Island mooring.

seaward and covered the Cross Island mooring on Nov. 22. Landfast ice covered the mooring from Nov. 22 – Dec. 2, during which time the currents beneath the landfast ice were eastward at ~5 cm s^{-1}, while the winds were westward at 7 – 10 m s^{-1}. The landfast temporarily retreated inshore from Dec. 3 – 12. At this time the winds varied from eastward to westward at ~5 – 10 m s^{-1}, current velocities varied coherently and in-phase with the winds and current speeds increased substantially and were much greater than those beneath the landfast ice. The landfast ice expanded steadily seaward after Dec. 12 with the mooring being ~15 km inshore of the ice edge between Dec. 12 – 21 based on the SAR images. At this time currents were weakly eastward,

while winds were westward. Thus during the periods of Dec. 3 – 12 and Dec. 12 – 21, the currents were weak and flowed upwind in agreement with the model results. However, after Dec. 22, the winds remained westward but the currents beneath the landfast reversed to become westward and downwind, in contrast to the model prediction. However, throughout the remainder of the record there was no consistent relation between currents and winds.

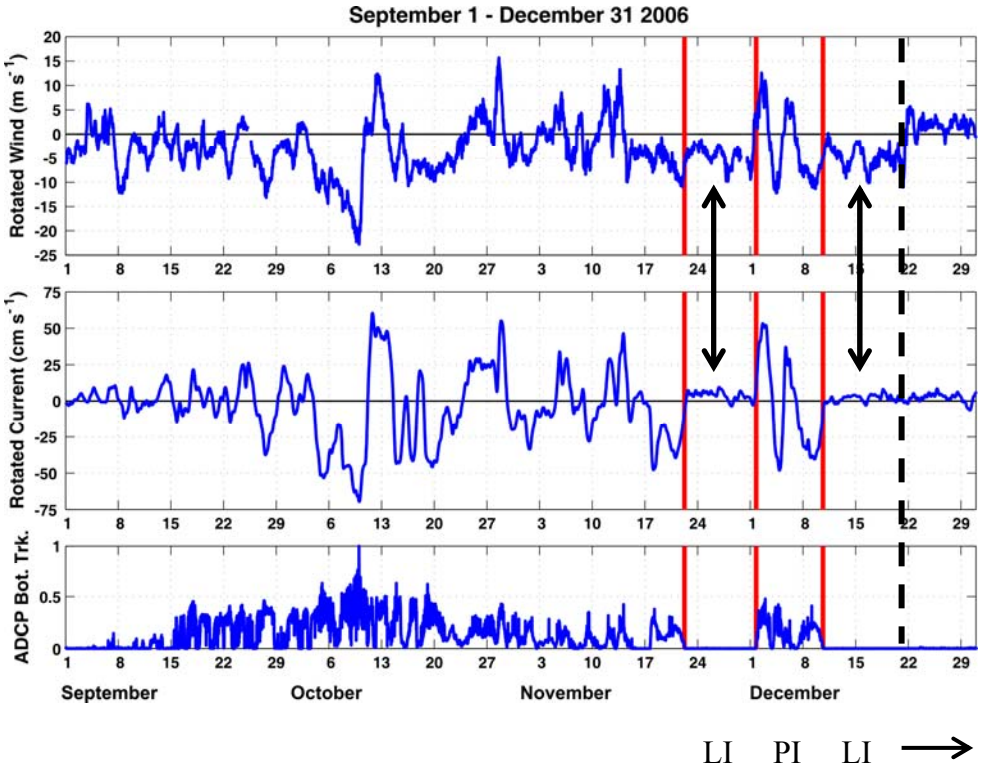

Figure 55. Time series of along-shelf winds (positive eastward), along-shelf currents (positive eastward), and ADCP bottom track return from the Cross Island mooring for the period Sept. 1 – December 31, 2006. The regions bracketed by the vertical red lines indicate when landfast ice (LI) or pack ice (PI) covers the mooring. The black vertical arrows indicate where the currents and winds are anti-correlated and the black dashed line indicates that currents and winds are uncorrelated after Dec. 21, 2006.

Before examining possible reasons for the wind-current correlation breakdown, we note that the current data suggest that there is a strong cross-shelf horizontal velocity shear across the ice-edge as predicted by the model. This is evident by the rapid changes in velocity as the landfast ice migrates back and forth over the mooring. The strong shears imply that the ice-edge

jet might be non-linear, at least occasionally as determined by the ratio of the relative vorticity to the planetary vorticity (or Rossby number, *Ro*):

$$\frac{1}{f}\frac{\partial u}{\partial y} \Rightarrow \frac{U}{fL_y} = Ro$$

where u is the along-shore velocity, y is cross-shore co-ordinate, L_y is the cross-shore length scale over which the along-shore velocity changes by U, and f is the Coriolis parameter. If along-shore currents change by up to 50 cm s^{-1} over a short distance, say 1 - 2 km, as suggested by the SAR images, then Ro ~ 0.4. Linear dynamics are typically assumed for Ro < 0.1, so that the ice-edge jets in the ABS are likely to be non-linear at least occasionally, when winds are strong and the transition zone between landfast ice and the drifting pack ice is only a few kilometers.

The model discussed above assumed along-shore uniformity in winds, bottom and underice friction. Under such conditions no along-shore pressure gradient develops. The breakdown in the anti-correlation implies that these assumptions may not be valid and that an along-shore pressure gradient is established. Other model runs show that the underice sea surface height field response to offshore winds depends upon the magnitude of the ice ocean drag coefficient. Specifically, we examined the sea surface height response to the same offshore winds (westward at 7 m s^{-1}) but with different values of the underice coefficient. In one case the underice friction coefficient was set constant at $r_i = 10^{-4}$ m s^{-1}. At a second transect approximately 100 m to the east of the first we set the underice friction coefficient to linearly increase from 0 to 10^{-4} m s^{-1} between the coast and the landfast ice edge. These differences are motivated by the assumption that differences in underice topography (due to along and cross-shore variations in landfast ice deformation) lead to spatial variations in the drag coefficient.

When forced by uniform along-shore upwelling favorable winds, the differences in along- and cross-shore underice friction parameterizations lead to along-shore differences in sea

level (**Figure 56**). While both regions suffer a drop in sea-level, the response is sensitive to the underice friction coefficient. We also find that the along-shore differences in sea surface height imply an along-shore sea level slope ~10 cm/100 km (e.g., 10^{-7}), which is of the same magnitude deduced from the simple along-shore momentum balance discussed above.

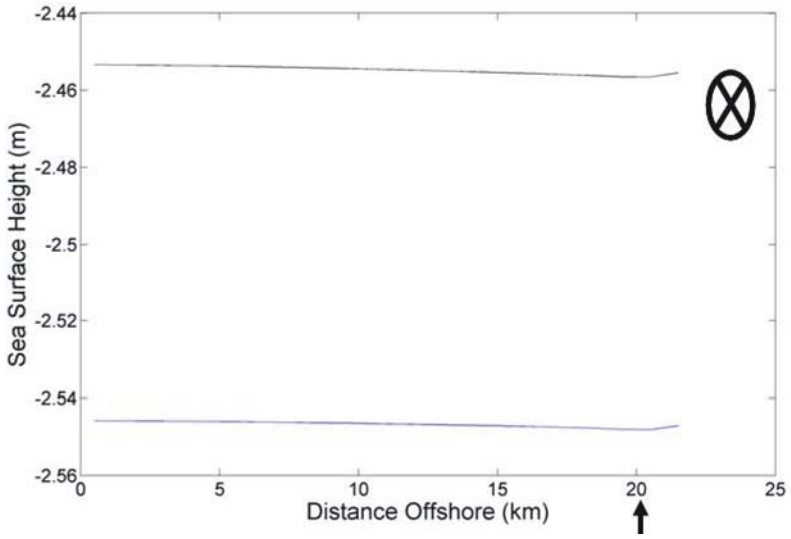

Figure 56. Cross-shore sea surface heights along two transects separated by 100 km at steady state and subject to upwelling favorable winds along the landfast ice edge. Upwelling winds at the ice edge (vertical arrow at the 20 km point on the x-axis) are denoted by the circled X.

These simple model experiments underscore the potentially important consequences of along- and cross-shore variations in landfast ice-ocean drag coefficients. Such variations can account for several of the observed features of circulation under the landfast ice. For example, along-shore variations in underice friction could give rise to along-shore sea-level (pressure) fields that force along-shore currents uncorrelated with the winds. Similarly, spatial variations in friction could also explain the weak correlation between sea level variations and offshore winds. For example, the structure of the outer edge of the landfast ice zone might change throughout the year (Tucker et al., 1977), which could alter the underice friction. We also emphasize that the circulation response to along-shore variations in underice friction coefficients would be

augmented by along-shore variations in the winds, since these also give rise to along-shore sea level gradients.

The spatially-varying underice topography can steer, block or channel the underice flow. Results from CROSS suggest that a deep keel was near the mooring and influenced the vertical structure of the flow field. This effect is illustrated in Figure 57, which is the February 2007 mean vertical velocity profiles and coefficients of variation (standard deviation divided by the mean) of the alongshore velocity for westward (blue profiles) and eastward (red profiles) flow events. Note that the mean westward flow profile is parabolic (similar to the structure discussed with respect to Figures 28 and 29), with maximum velocity at mid-depth. The coefficient of variation is a maximum at the

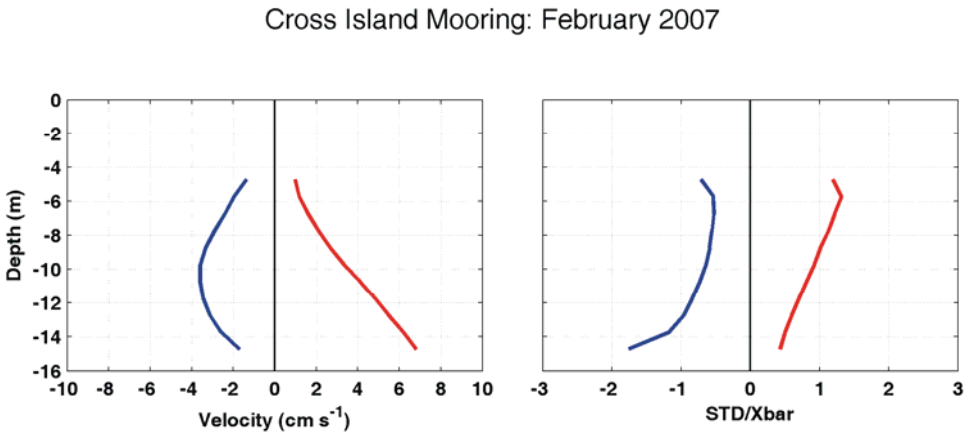

Figure 57. Mean velocities and coefficients of variation as a function of depth for westward (blue) and eastward (red) flows computed for February 2007 from the Cross Island mooring.

bottom. In contrast the mean eastward profile is a maximum at the bottom and linearly decreases with height above the bottom. The coefficient of variation profile for eastward flows increases moving upward through the water column. The asymmetric velocity profiles imply that there is a deep keel to the west of the mooring that affects the eastward flow. The presence of the keel would likely intensify the flow at depths below the keel depth and perhaps leave a separated flow and turbulent wake in the lee of the keel. Flow separation is consistent with the small mean

velocities and the increase in the coefficient of variation at the top of the velocity profile. Hence the underice topography could be a source of form drag that could be a source of turbulent energy and a sink for mean flow energy.

7. Temperature, salinity, transmissivity, fluorescence

Water property parameters also vary throughout the year in accordance with the formation and ablation of sea ice. The annual cycles of temperature (*T*) and salinity (*S*) are shown for each mooring (with high quality data) in **Figures 58 – 72.** At each site the annual temperature cycle consists of maximum near-bottom temperatures that range from 5 – 2^{o}C in summer and fall, followed by a rapid (1 – 2 week) collapse to the freezing point (~-1.7^{o}C) (usually in early October), after which temperatures remain near-freezing until late June or early July. At that time, temperatures slowly increase and reach about 0^{o}C by late July after the ice melts. Salinity varies from 14 through 32 through the open water season, with the lowest salinities observed immediately following the decay of the landfast ice and in the aftermath of sufficiently strong winds that mix the water column. After the ice forms in October, salinities increase and attain values of 34 – 35 by January due to the expulsion of salt from growing sea ice. Thereafter, salinities remain relatively constant through winter and spring before slowly starting to decrease in June. Following the removal of ice and the first significant wind-mixing event, salinities rapidly decrease as a consequence of mixing of low-salinity ice meltwater and the river plume (discussed in Section V).

Transmissivity also shows a strong seasonal cycle. During late summer and fall it varies due to stirring by the winds and currents, but generally decreases to very low values at about the time of rapid ice formation in early October. The low values are due to turbulent mixing of the water column brought about by winds and cooling and freezing that extend over the entire water

column. The high suspended sediment levels in the water column during freeze-up suggest that much sediment is included into the landfast ice matrix during the vigorous production period. The incorporation of sediments into sea-ice has bearing on oil dispersal because the sea ice represents a potential vehicle by which oiled sediments can be subsequently transported out of the region. However, that transport would be delayed until the following summer during and after break-up. Either the sediment-laden ice will be advected out of the region or will melt *in-situ* and release its oiled sediments back into the water. Transmissivity values remain relatively high through winter although the data suggests periods of moderate suspended sediments followed by clearer water masses. Winter periods of moderately low transmissivity might, in fact, be a sampling artifact because the transmissometer was inclined to the horizontal on the mooring frame. Thus, sediment might have accumulated on the lens during periods of low flow and then be cleansed when current speeds increased. Although there is some uncertainty in the winter transmissivity record, there is a consistently large decrease in transmissivity in early June of each year, coincident with the spring freshet when rivers are carrying a heavy suspended sediment load. This load sinks to the seabed under the landfast ice because there is little energy available for mixing in the water column. Once the ice retreats, the near-bottom suspended sediment load remains relatively low until vigorous storms mix sediment back into the water column where it is advected by wind-driven currents.

Fluorescence provides a qualitative measure of the chlorophyll content in the water. These values are always low except in late July or August after the ice has disappeared and transmissivity levels have risen above the post freshet minimum.

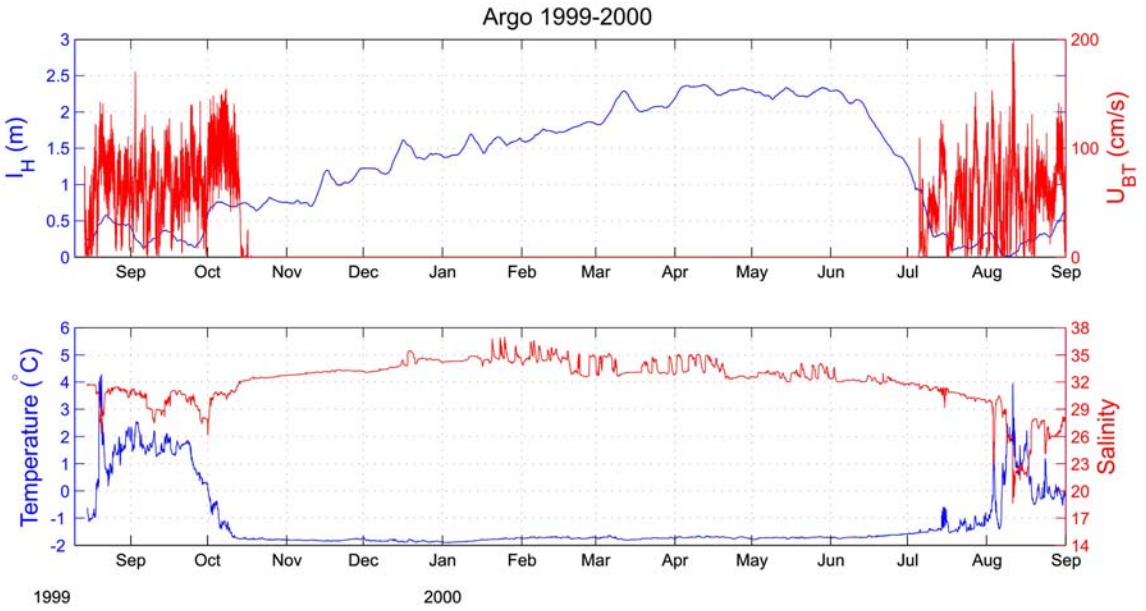

Figure 58. Ice thickness and bottom track velocity (upper panel) and temperature and salinity (lower panel) at ARGO during the 1999 – 00 deployment.

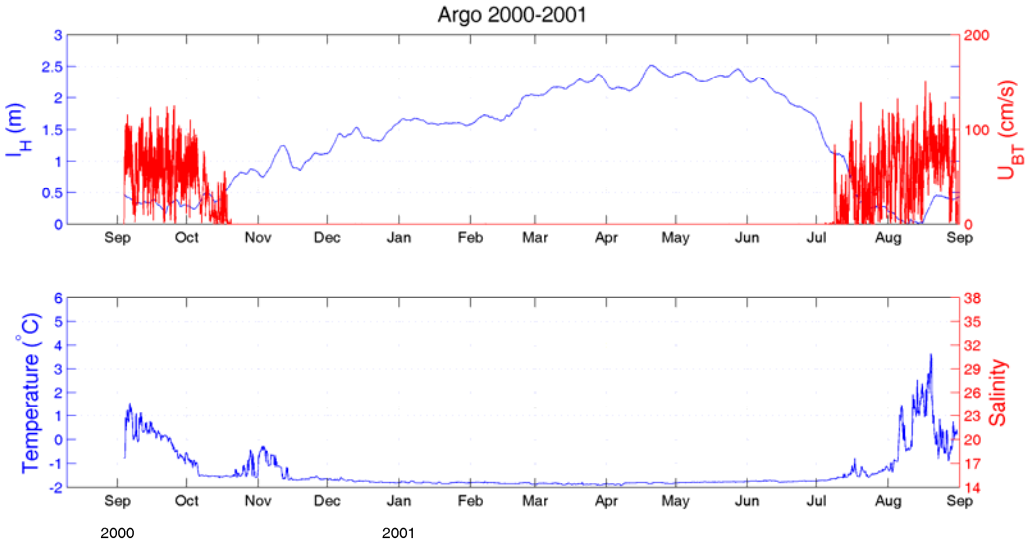

Figure 59. Ice thickness and bottom track velocity (upper panel) and temperature (lower panel) at ARGO during the 00 – 01 deployment.

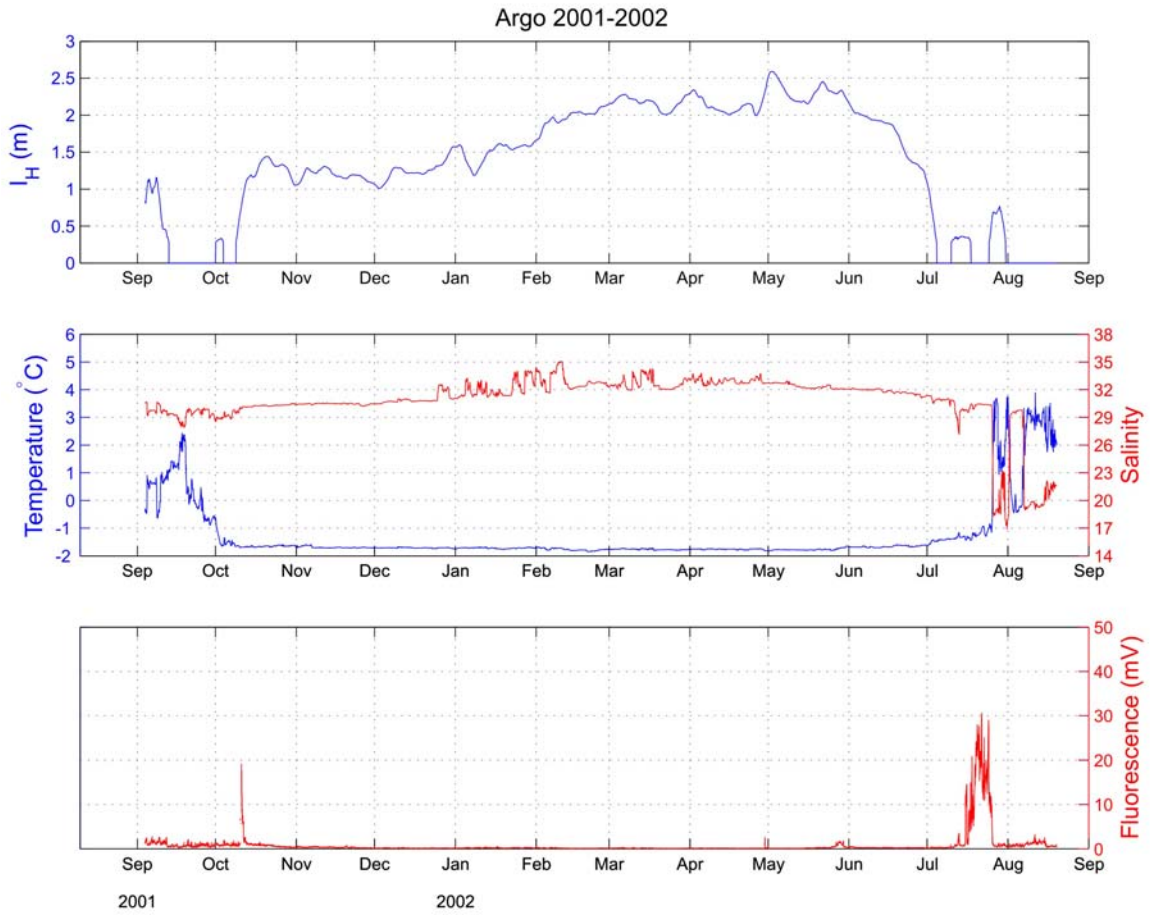

Figure 60. Ice thickness (upper panel), temperature and salinity (middle panel) and fluorescence (lower panel) at ARGO during the 2001 – 02 deployment.

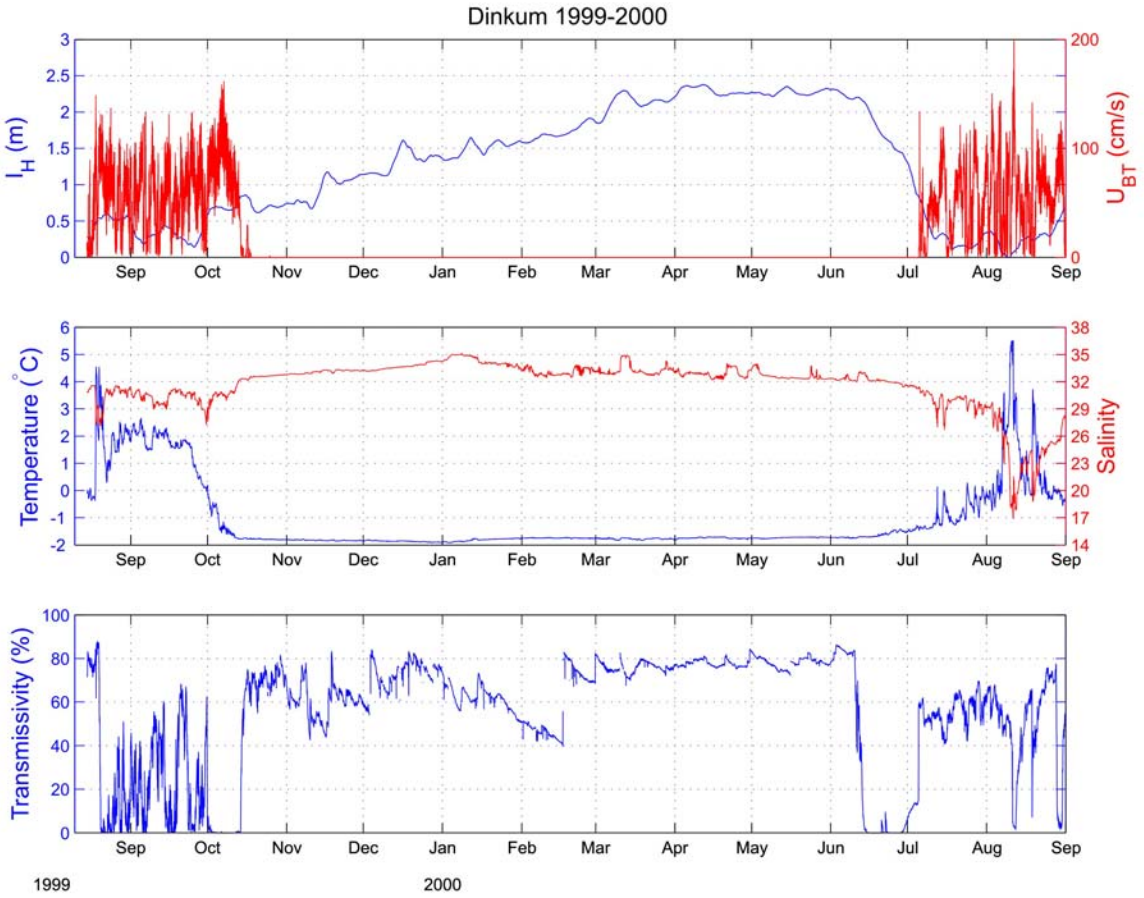

Figure 61. Ice thickness (upper panel), temperature and salinity (middle panel) and transmissivity (lower panel) at DINKUM during the 1999 - 00 deployment.

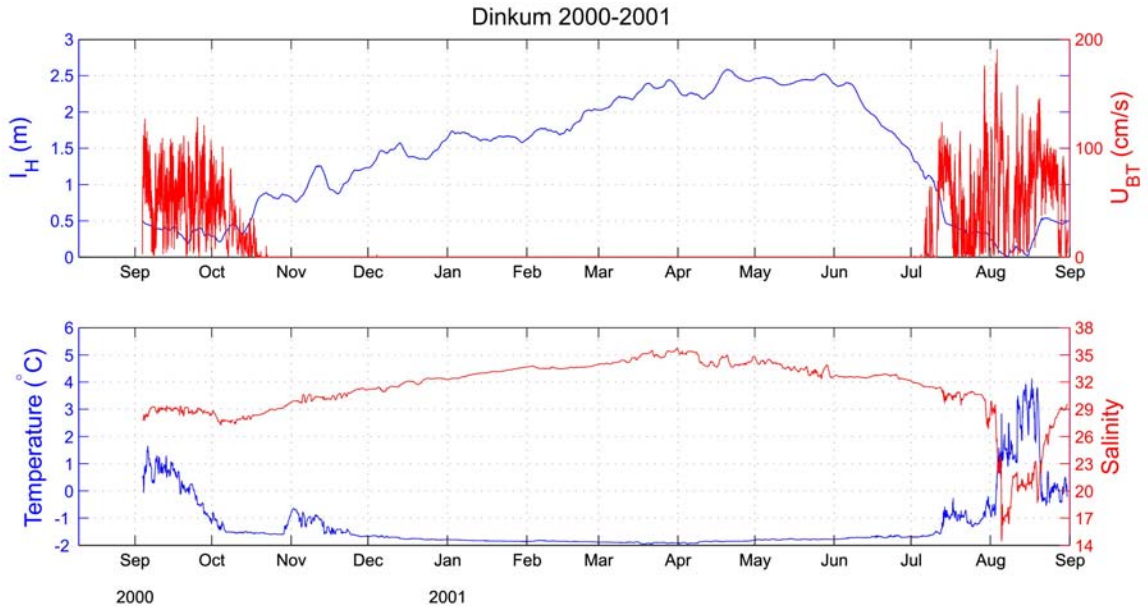

Figure 62. Ice thickness (upper panel) and temperature and salinity (lower panel) at DINKUM during the 2000 - 01 deployment.

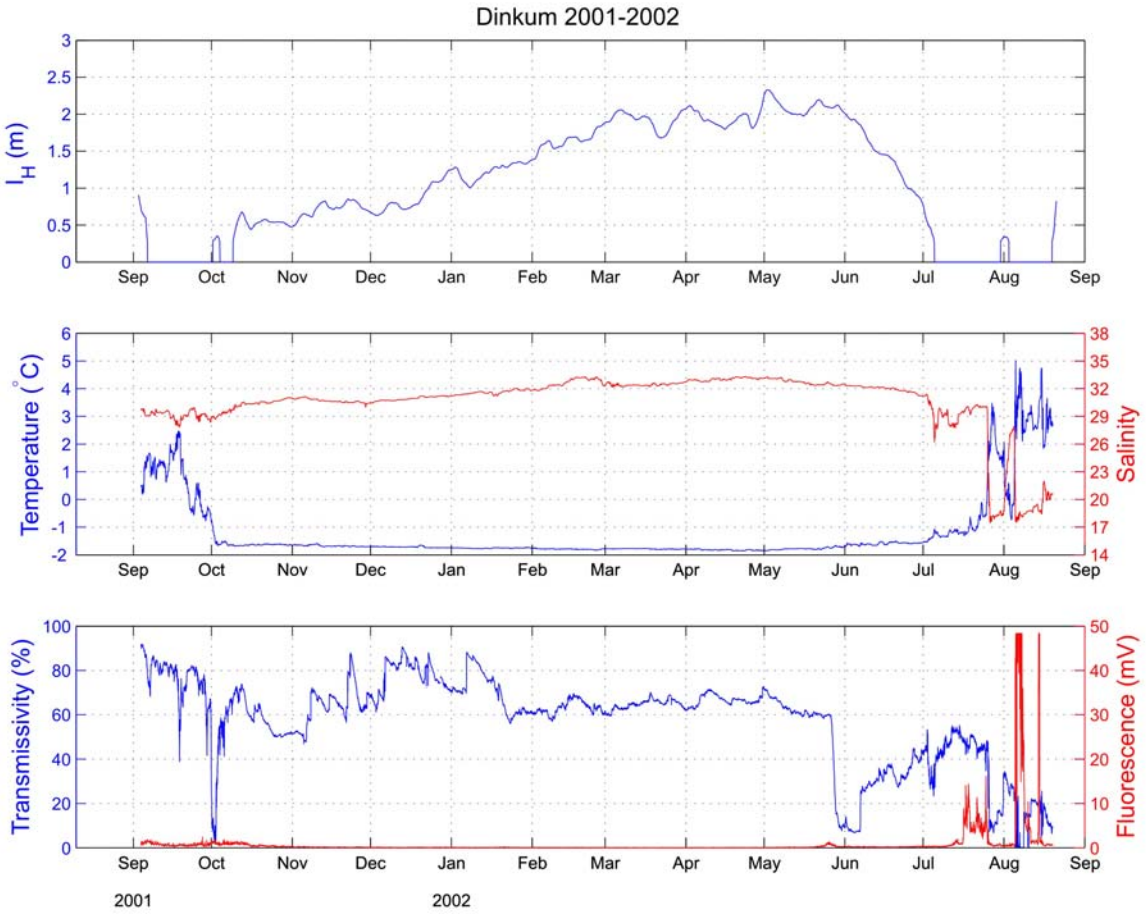

Figure 63. Ice thickness (upper panel), temperature and salinity (middle panel) and transmissivity and flourescence (lower panel) at DINKUM during the 01 - 00 deployment.

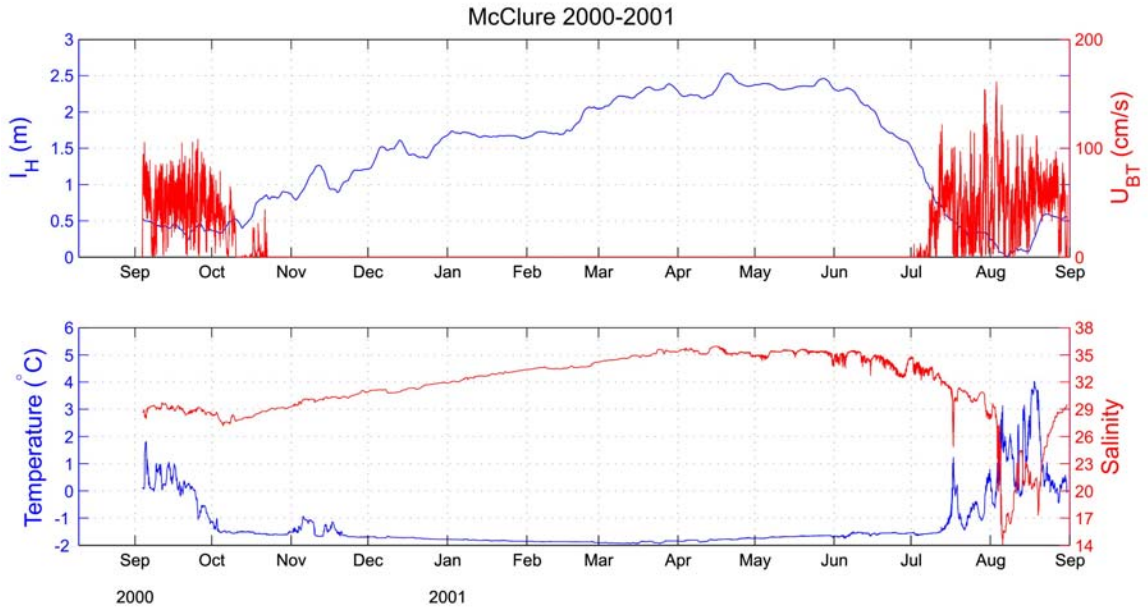

Figure 64. Ice thickness and bottom-track velocity (upper panel) and temperature and salinity (lower panel) at MCCLURE during the 2000 - 01 deployment.

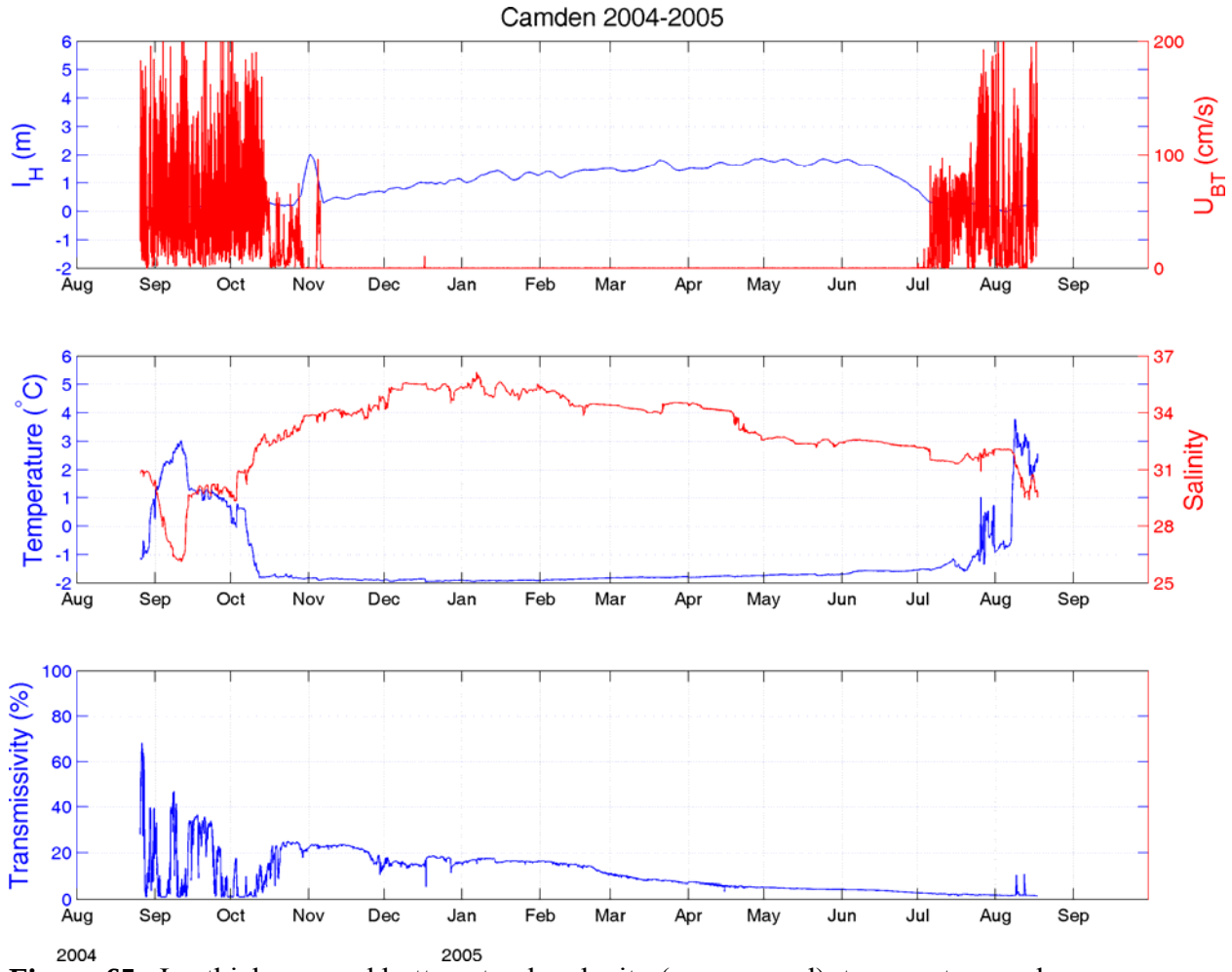

Figure 65. Ice thickness and bottom-track velocity (upper panel), temperature and salinity (middle panel) and transmissivity at CAMDEN during the 2004-2005 deployment.

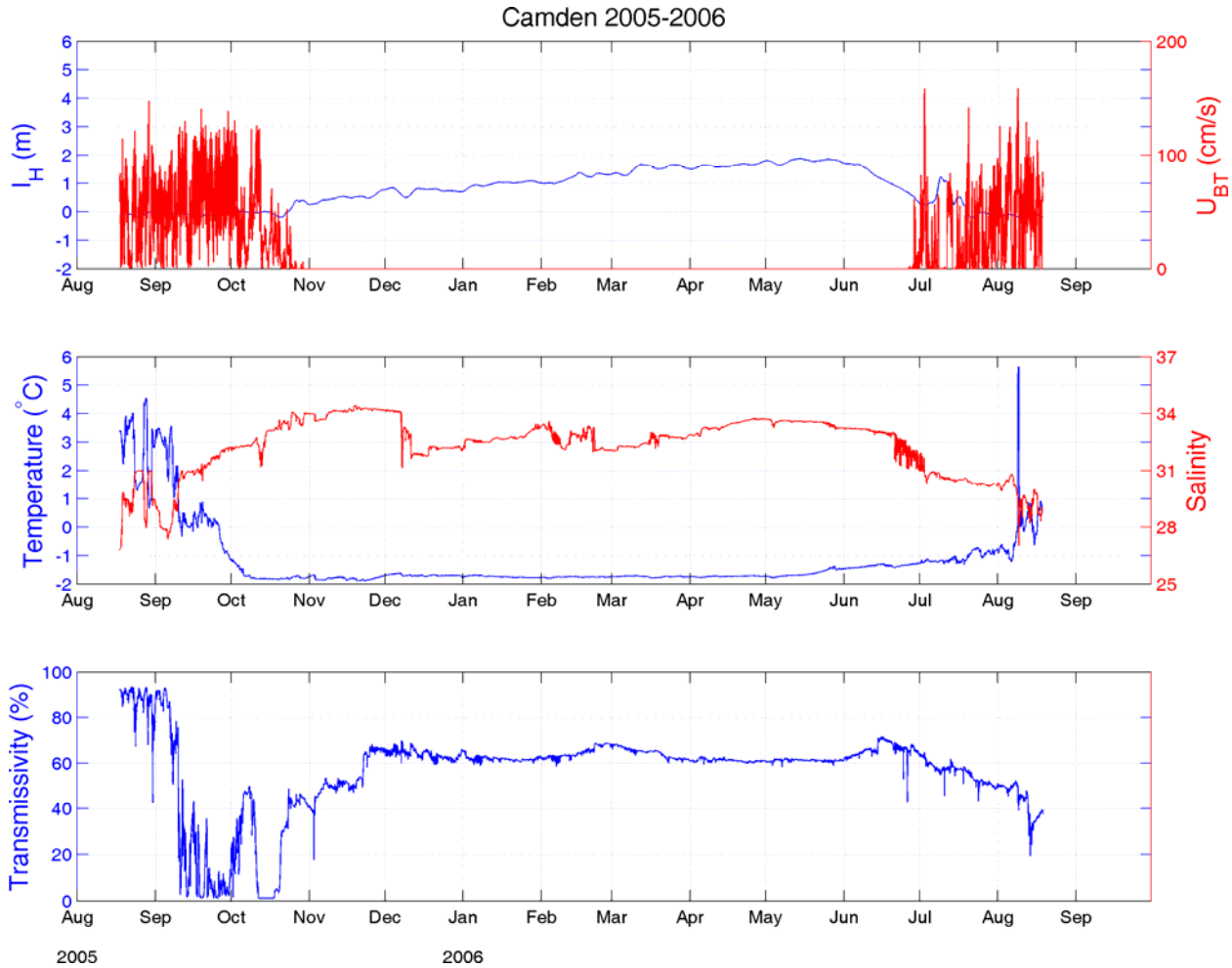

Figure 66. Ice thickness and bottom-track velocity (upper panel), temperature and salinity (middle panel) and transmissivity at CAMDEN during the 2005-2006 deployment.

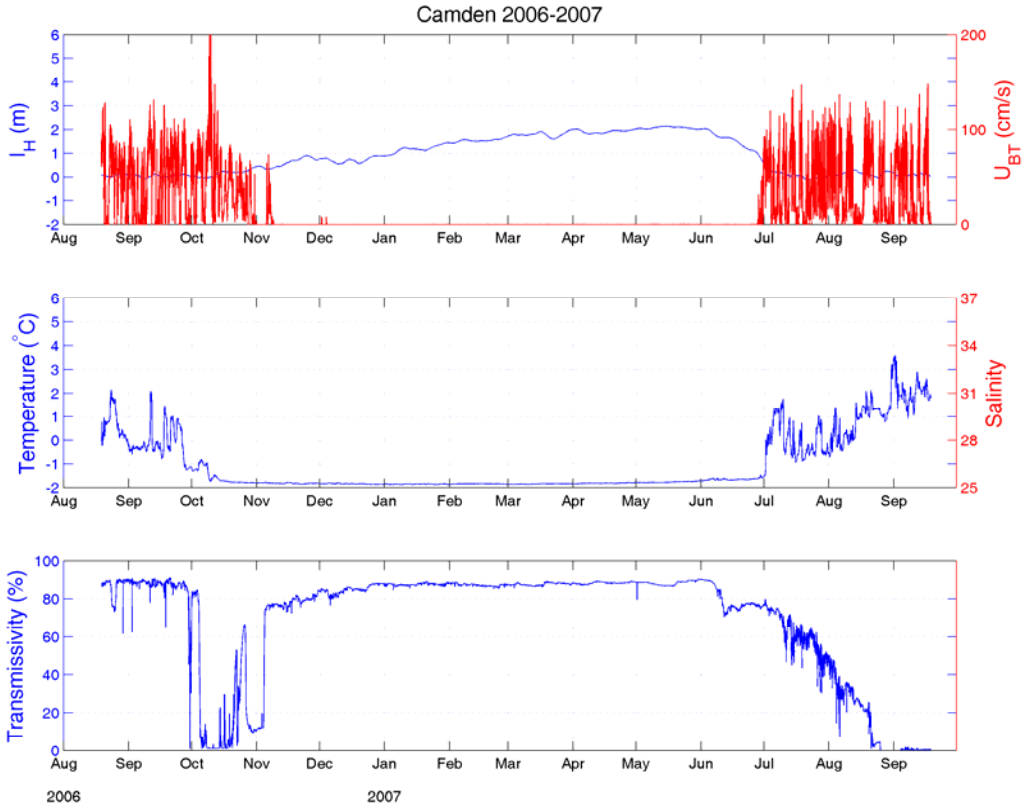

Figure 67. Ice thickness and bottom-track velocity (upper panel), temperature (middle panel) and transmissivity at CAMDEN during the 2006-2007 deployment.

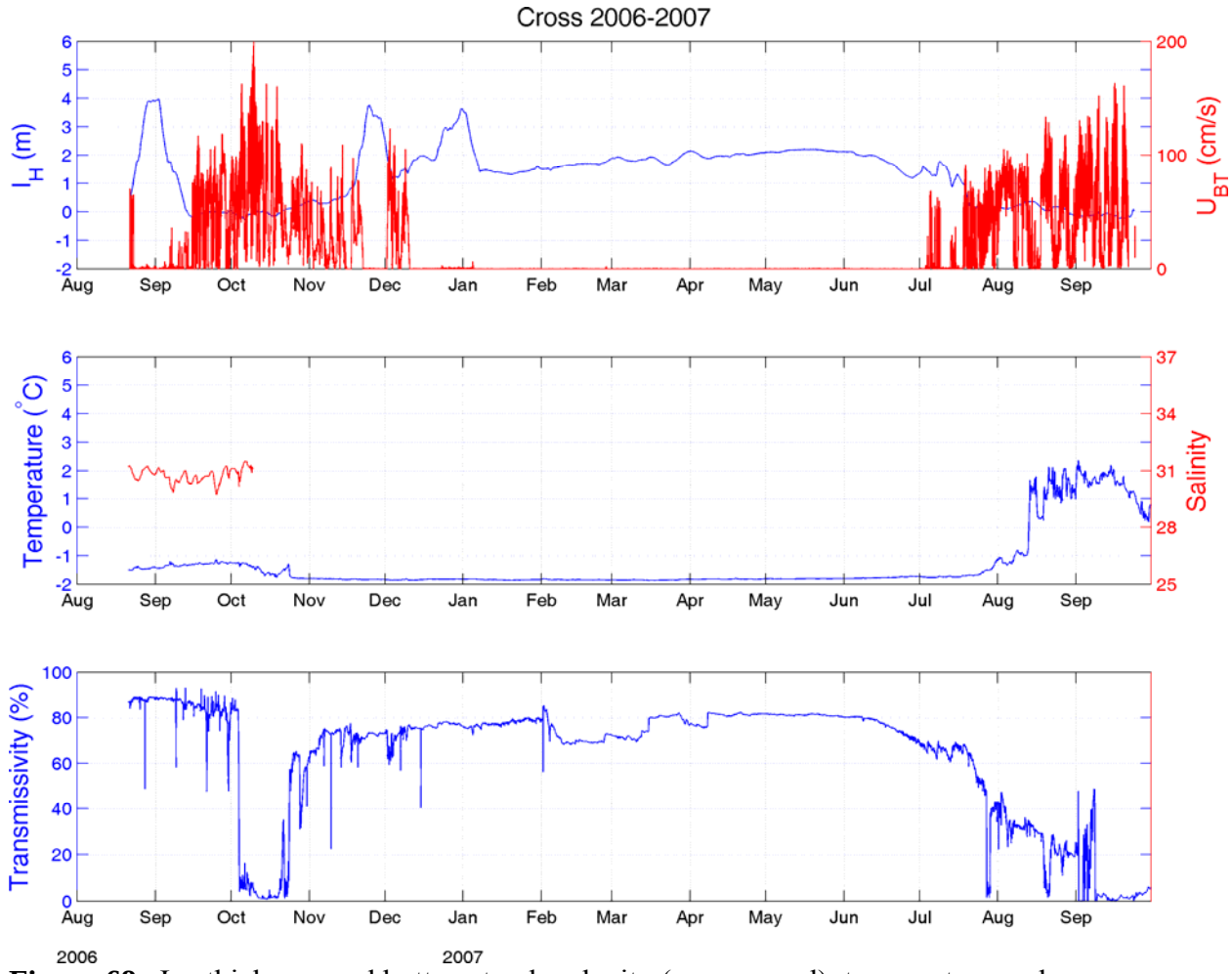

Figure 68. Ice thickness and bottom-track velocity (upper panel), temperature and salinity (middle panel) and transmissivity at CROSS during the 2006-2007 deployment.

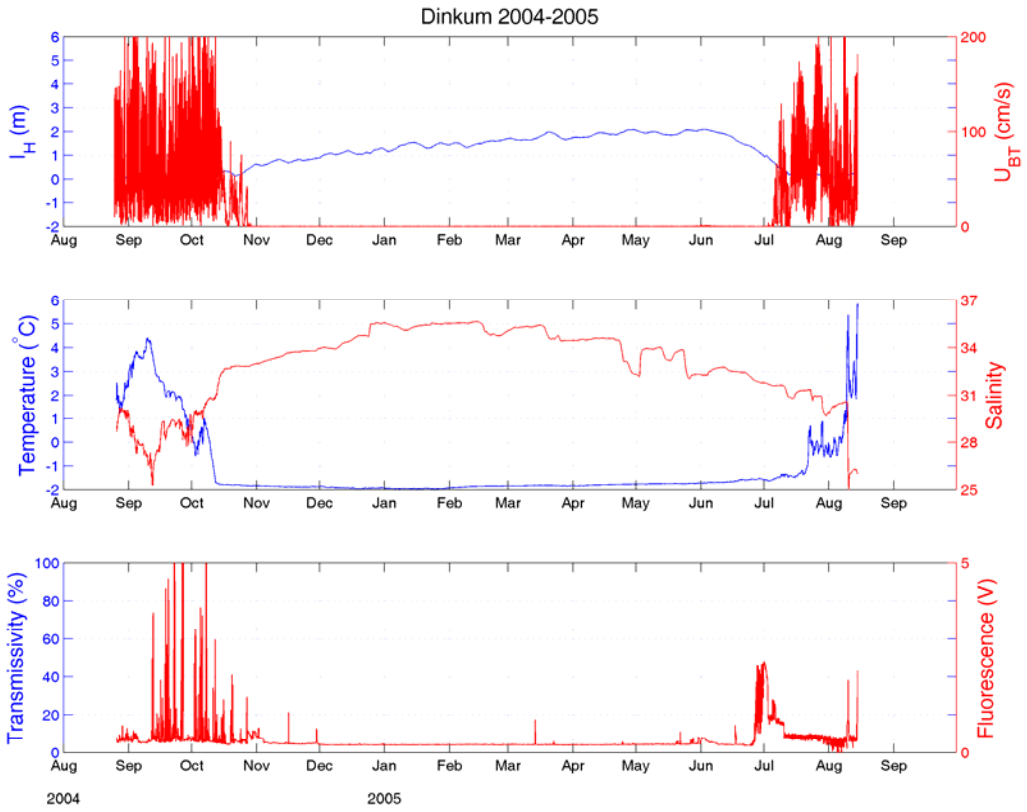

Figure 69. Ice thickness and bottom-track velocity (upper panel), temperature and salinity (middle panel) fluorescence at DINKUM during the 2004-2005 deployment.

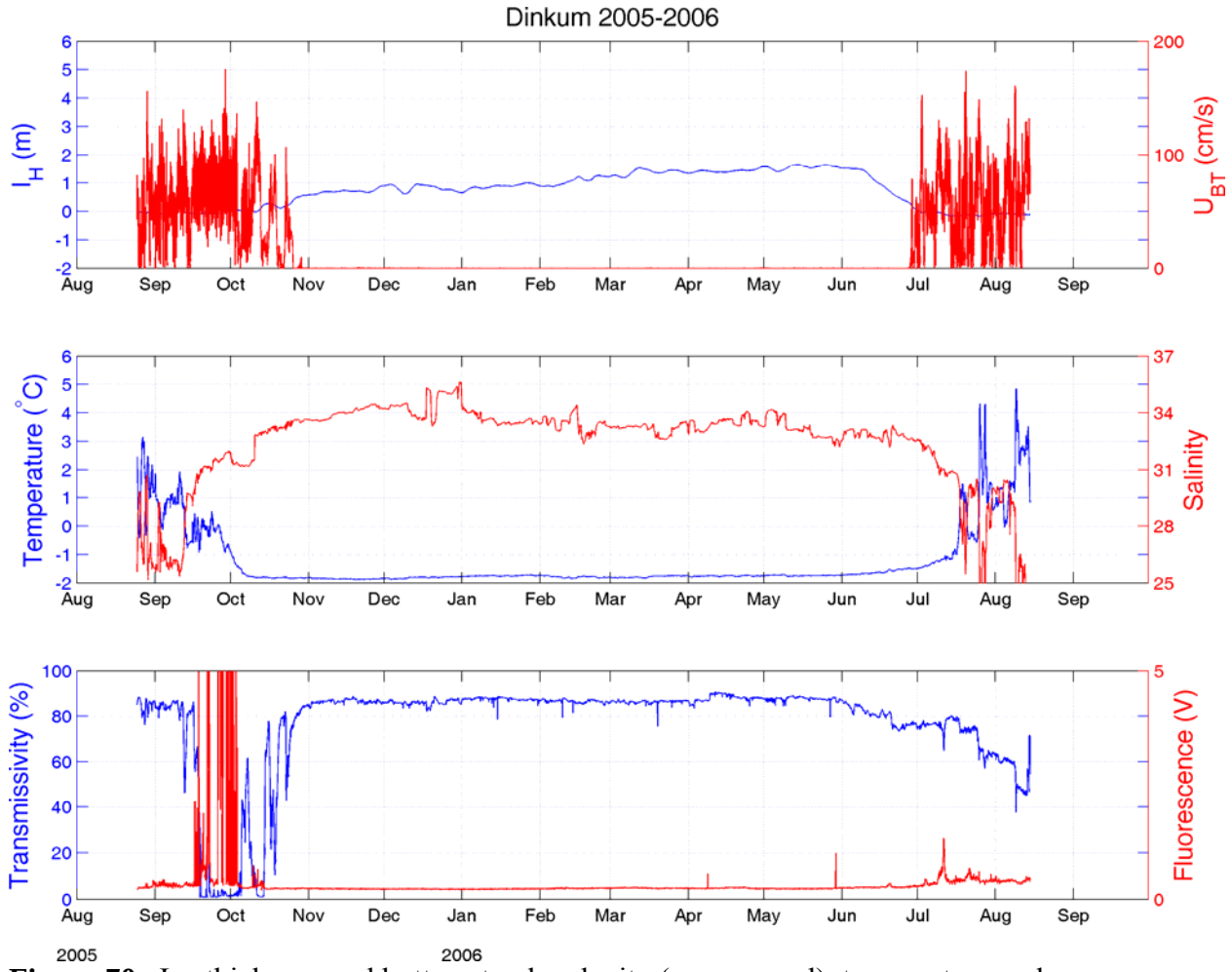

Figure 70. Ice thickness and bottom-track velocity (upper panel), temperature and salinity (middle panel) and transmissivity and fluorescence at DINKUM during the 2005-2006 deployment.

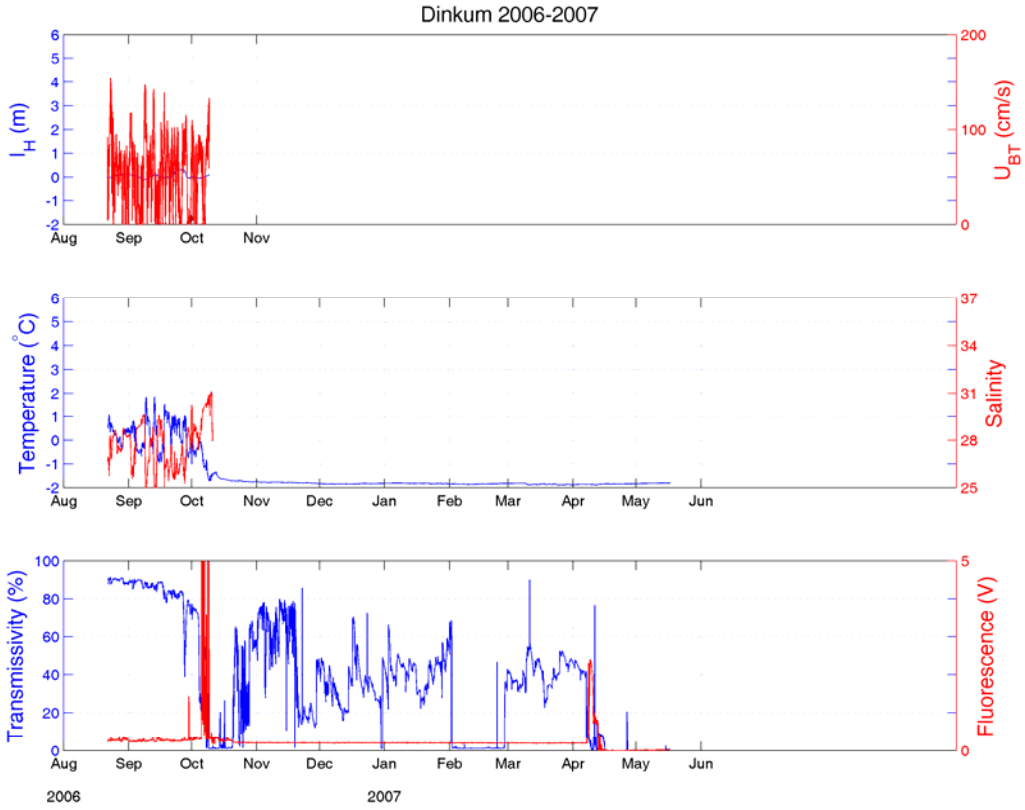

Figure 71. Ice thickness and bottom-track velocity (upper panel), temperature and salinity (middle panel) and transmissivity and fluorescence at DINKUM during the 2006-2007 deployment.

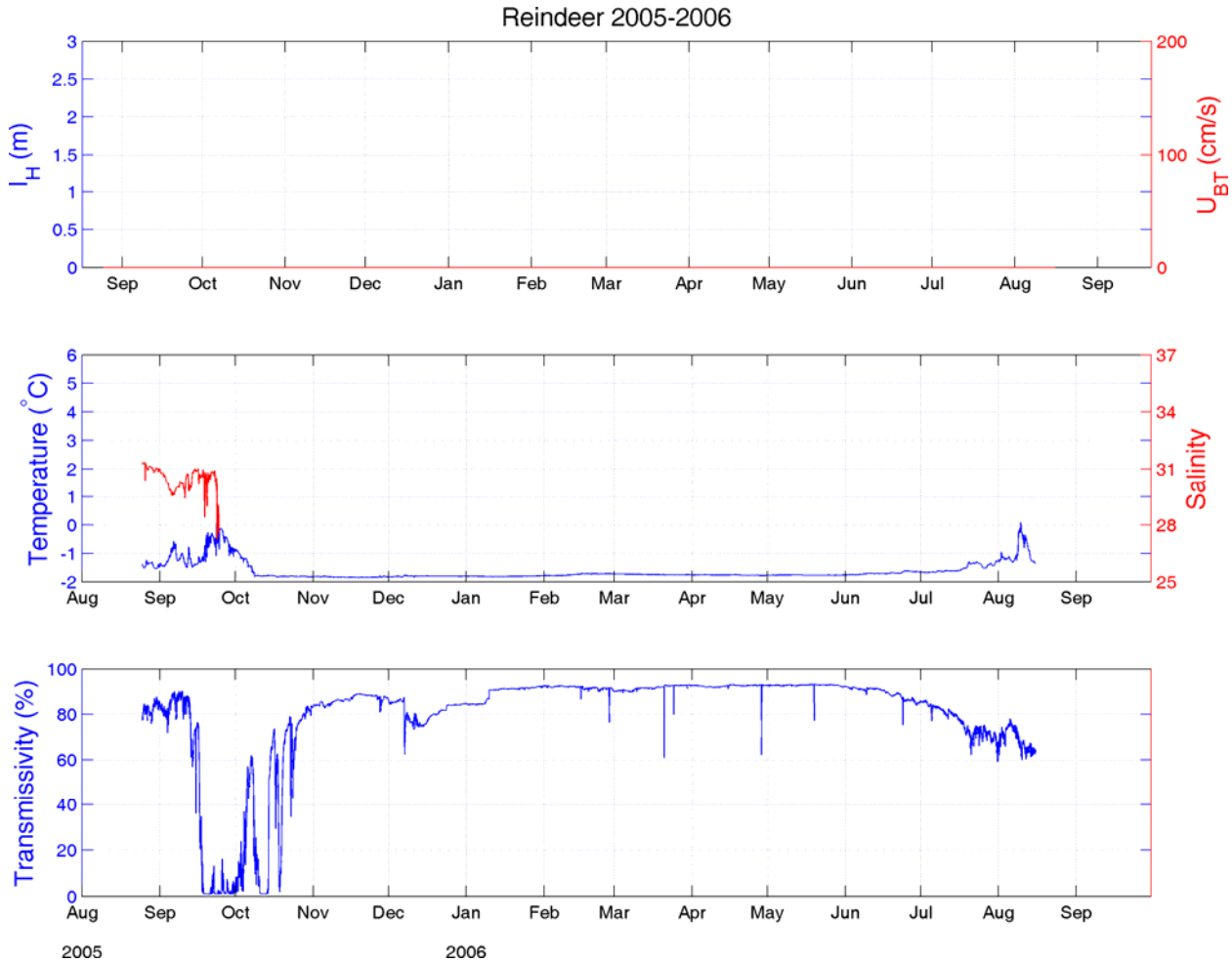

Figure 72. Temperature and salinity (middle panel) and transmissivity (lower panel) at REINDEER during the 2005-2006 deployment.

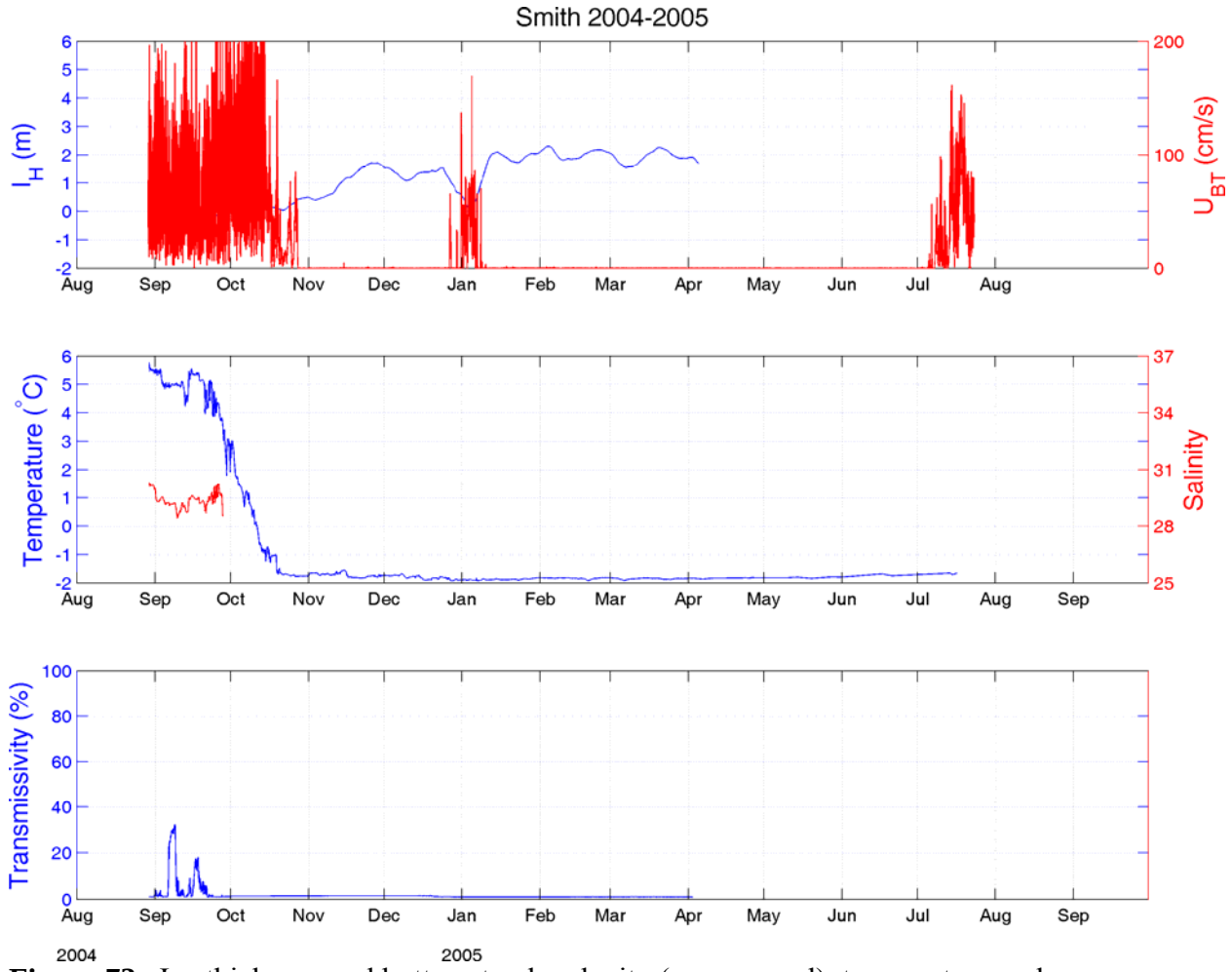

Figure 73. Ice thickness and bottom-track velocity (upper panel), temperature and salinity (middle panel) and transmissivity at SMITH during the 2004-2005 deployment.

Figure 74 shows in detail the relationship between Sagavanirktok River discharge, transmissivity, ice thickness, currents and current shears from May through June from mooring DINKUM in 00. Prior to the onset of discharge, all parameters are relatively constant and typical of winter conditions. However, once the freshet reaches its maximum on June 9, the transmissivity and ice thickness rapidly decrease, relatively large cross-shore flows (of up to 10 cm-s^{-1}) are initiated, and vertical shears large cross-shore flows (of up to 10 cm-s^{-1}) are initiated, and vertical shears increase. Rapid sea-ice ablation occurs due both to strong solar heating and to the rapid decrease in albedo of the

ice surface by melt water ponds and/or the spreading of turbid river water over the surface of the ice *Searcy et al.* [1996].

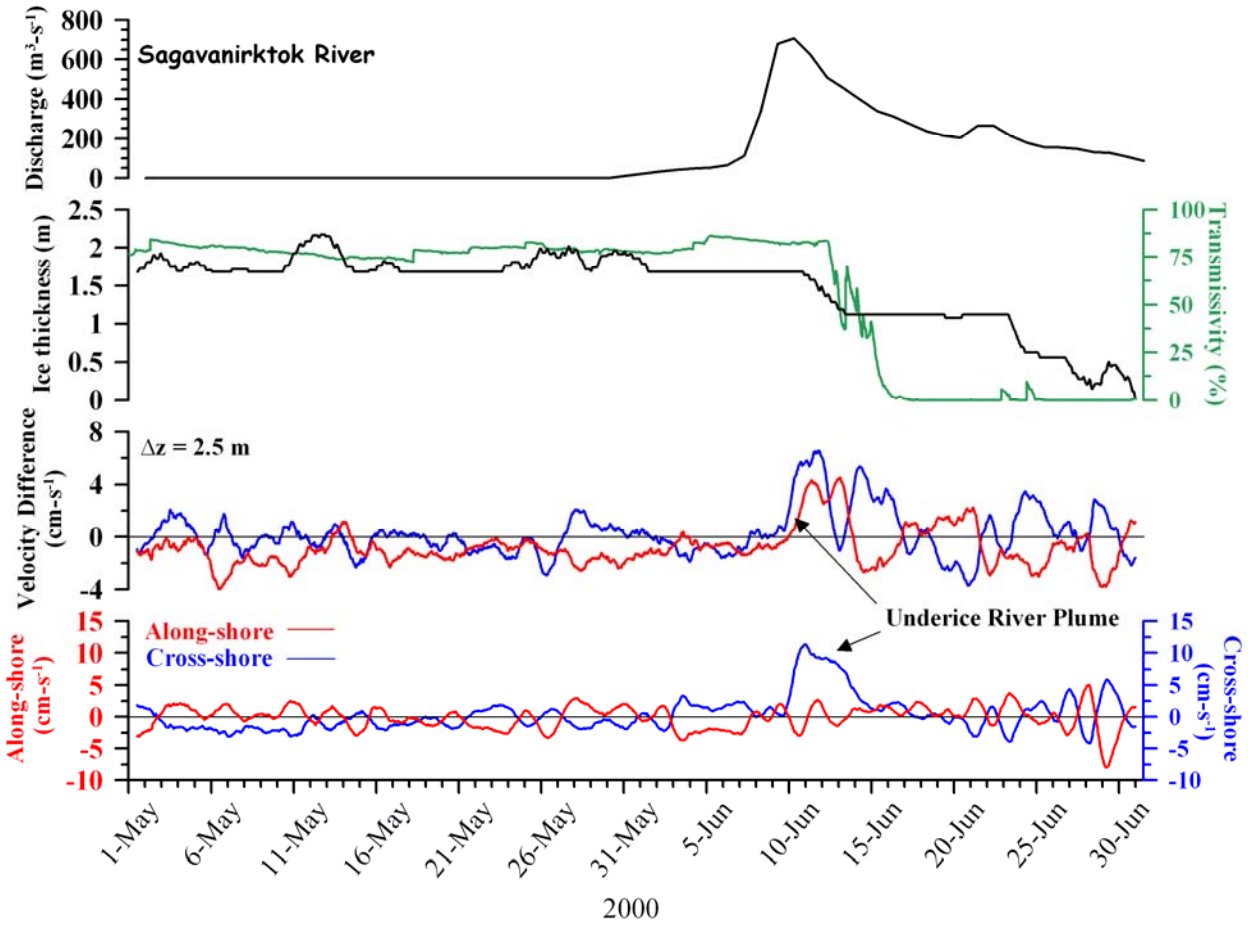

Figure 74. May through June time series of (from top to bottom) Sagavanirktok River discharge, ice thickness (black), transmissivity (green), cross- and along-shore velocity shear, and cross- and along-shore velocities. Along-shore (cross-shore) components are red (blue).

V. FRESHWATER INFLUENCE

In this section we further explore the influence that freshwater runoff exerts on the inner shelf's density structure and circulation field. During river breakup a significant fraction of the river runoff flows beneath the landfast ice where it establishes a strongly stratified water column, with salinity accounting for most of the stratification **(Figure 75a)**. Salinities increase by ~25 m^{-1} across the halocline, while temperature decreases by

1.5 ^{o}C m^{-1} (**Figure 75b**) and transmissivity by 80% m^{-1} (**Figure 75c**). The inner shelf will remain highly stratified until sufficient turbulent energy is supplied to the water column to mix it vertically. This is evident from the bulk Richardson number:

$$Ri = \frac{g}{\rho}\left(\partial\rho/\partial z\right)\Big/\left[\left(\partial u/\partial z\right)^2 + \left(\partial v/\partial z\right)^2\right] \qquad \textbf{(3)}$$

where $\partial\rho/\partial z$ is the vertical density gradient and the denominator is the square of the vertical gradient of horizontal velocity. $Ri \sim 325$ for typical values of the gradients of underice shear and density observed during river runoff in summer. These values are substantially greater than the range of 1 - 10 typical of weak and moderately stratified shelf conditions and much larger than the value of ~1 when mixing occurs. The large Richardson number also implies that interfacial stresses are small so that after the ice has receded, most of the momentum imparted by the wind stress will be confined to the plume. This has important implications for the subsequent spreading of the plume after the landfast ice retreats. For example, if we assume that the wind stress is confined to a strongly stratified 2 m thick plume, a weak but upwelling favorable wind speed of 2 m s^{-1} would transport the plume seaward at ~5 cm s^{-1} (~5 km day^{-1}). Such winds are not

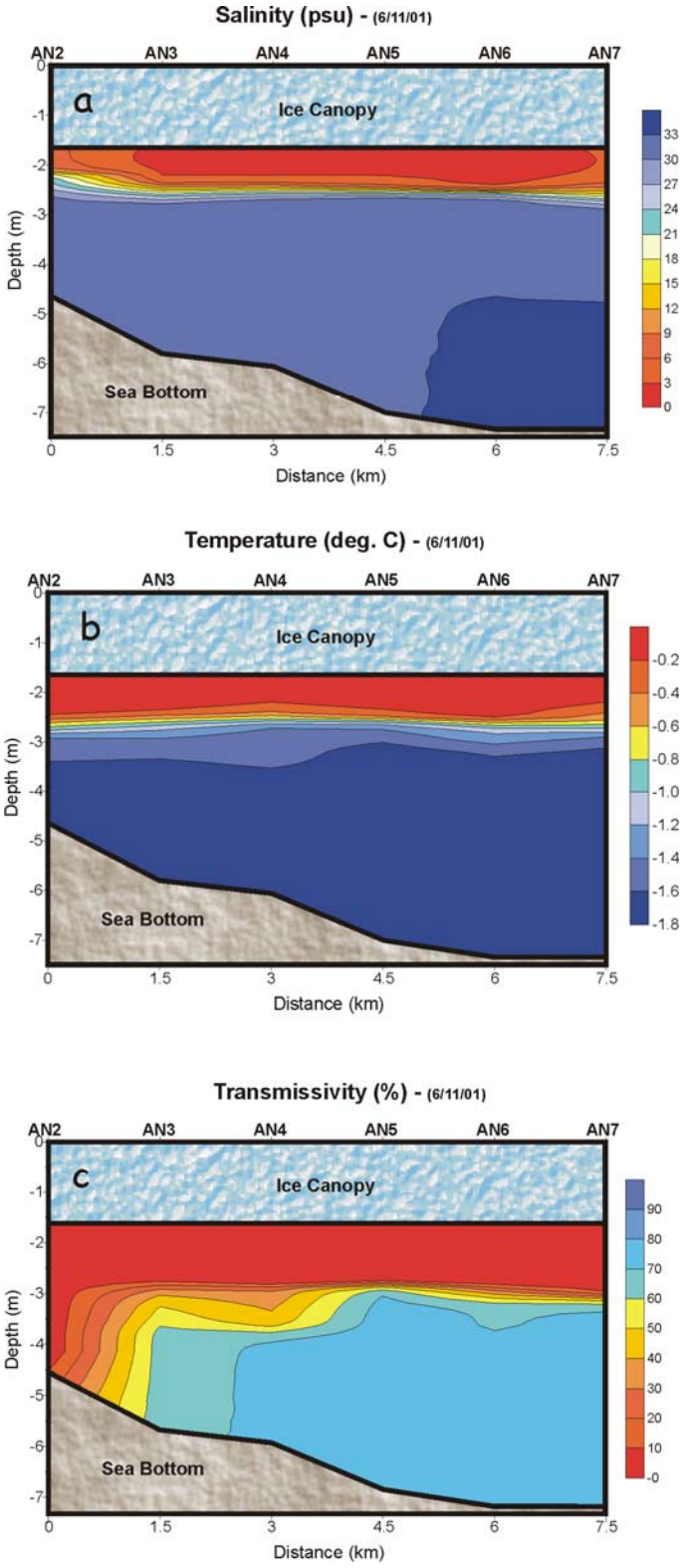

Figure 75. a) Salinity, b) Temperature, and c) Transmissivity along the DINKUM June 2001 transect (see Figure 3 for location of this transect.)

unrealistic for the nearshore Beaufort Sea in summer, where the winds are frequently upwelling-favorable. The offshore velocity of the plume is comparable to the 6 cm s^{-1} alongshore speed a surface oil slick would have assuming it moves at 2% of the wind speed. Although simplified, this example suggests that the effects of stratification and vertical mixing cannot be ignored in oil spill trajectory models for the nearshore Beaufort Sea in summer.

How rapidly the stratification erodes depends upon the strength of the winds once the ice has retreated or becomes mobile, since wind is the primary agent for supplying mixing energy for the water column. We determine the work required (*M*) to completely mix a vertically stratified water column based on potential energy considerations:

$$M = \frac{1}{h}\int_{-h}^{0} (\rho(z) - \bar{\rho}) g z dz \qquad \textbf{(4)}$$

where *g* is the gravitational acceleration, $\rho(z)$ is the density at depth *z*, and $\bar{\rho}$ is the mean density of the water column. The winds are the sole source of mixing energy because the currents (tidal and subtidal) have insufficient shear to overcome the large density gradient. We estimate the time required to vertical mix the water column from *Denman and Miyake's* [1973] open-ocean relationship:

$$\frac{\partial E}{\partial t} \cong \frac{\rho_a m C_D U_{10}^3}{h} \qquad \textbf{(5)}$$

where ($\partial E / \partial t$) is the rate of working by the wind on the water column, ρ_a is the air density (1.29 kg m^{-3}), *m* is an efficiency factor and C_D is the drag coefficient (both ~ 10^{-3}), *h* is the water depth (5.6 m for the CTD profiles shown in **Figure 75**) and U_{10}^3 is the cube of the wind speed at 10 m elevation. Dividing eq. 4 by eq. 5 gives the time required for a *steady* wind to mix the water column. Complete mixing is achieved in ~200 days for

constant winds of 6 m s^{-1}. As discussed below, however, the mixing response depends sensitively on whether winds are upwelling- or downwelling favorable.

The cross-shore velocities associated with the spreading of the river plume shown in **Figure 50** suggest that the plume spreads rapidly offshore. How far offshore does the plume propagate under the ice? *Yankovsky and Chapman* [1997] developed a scale-length for the offshore extent of a buoyant surface-advected plume for a *steady* outflow in the absence of surface friction:

$$y_s = \frac{2\left(3g'h_o + v_i^2\right)}{f\left(2g'h_o + v_i^2\right)^{1/2}}$$

where y_s is the offshore extent of the plume, $g' = g\Delta\rho/\rho_o$ and v_i is the inflow velocity, h_o is the inflow depth, and f is the Coriolis parameter (1.37 x 10^{-4} s^{-1} at 71°N). Although the steady-state, inviscid assumptions do not strictly apply to the impulsive-type discharge characteristic of arctic rivers in early summer or for plumes under landfast ice (where friction might be important), we nevertheless apply this theory to early June when the peak outflow of the Kuparuk River is about 2200 m^3-s^{-1}. We take the effective width of the river mouth to be 1 km and the inflow depth to be 2 m, so that $v_i \sim 1.1$ m-s^{-1}. From the salinity cross-section, we estimate $\Delta\rho \sim 22$ kg-m^{-3}, $\rho_o \sim 1025$ kg-m^{-3} so that $g' \sim 0.21$ m^2- s^{-2}. For these values the offshore extent of the plume is ~25 km and well beyond the region of our measurements. The plume might in fact extend further offshore because of frictional coupling between the plume and ice. Nevertheless, for the case considered, the propagation speed of a gravity current is $c = \sqrt{2g'h_o}$ [*Benjamin*, 1968], so that $c \sim 0.9$ m-s^{-1} for the assumed parameters. Hence the plume should propagate the distance y_s in less than a day. Note also that *Yankovsky and Chapman's* scaling assume

no ambient mean flow. Our observations indicate that the spring freshet can occur during periods of variable along-shelf flow and these might alter the offshore distance that the buoyant river plume can spread [*Yankovsky*, 2004].

Stratification also affects the velocity profile as shown by the mean open water season profiles from REINDEER (**Figure 76 and 77)**. As was done with **Figures 16 and 17**, the means are computed separately for westward and eastward flow events and plotted versus the scaled depth to account for changes in water column depth.

When the along-shore flow is eastward (**Figure 54**), there is little shear in the along- and cross-shore velocities. Eastward currents occur under eastward or downwelling favorable winds, which (at steady state and under an idealized two-dimensional case) cause offshore transport of low density water in the bottom boundary layer. As this water flows seaward it convectively mixes with denser surface water to rapidly erode stratification. Thus the simple mechanical mixing example discussed above does not apply in the presence of a coast. As a consequence, downwelling winds can efficiently and rapidly mix the nearshore water column. Consequently, the open water season stratification reflects the time-integrated response to runoff, meltwater, and the directionality of the winds. The breakdown in stratification allows a more efficient vertical transport of vertical momentum from the wind throughout the water column leading to small velocity shears and, if the water column is sufficiently shallow, overlapping surface and bottom Ekman layers. Interestingly, we do not observe onshore transport in the surface layer and offshore transport in the bottom for eastward flow (left panel of **Figure 76**) for this downwelling case. There are several possible reasons for this. First, our simple averaging approach might mask bottom Ekman layers. Second, a

sufficiently strong alongshore pressure gradient would force an onshore geostrophic flow that swamps the Ekman transport. Lastly, the shelf flow field is likely three-dimensional, so that our simple two-dimensional analysis cannot be applied to this setting.

For westward or upwelling favorable winds the mean flow is westward (right panel of **Figure 77**), but the velocity profile is highly sheared. The sheared structure is consistent with surface offshore transport of low-density water and onshore transport of denser water beneath the surface layer. In aggregate these effects tend to enhance stratification, which in turn, inhibits vertical mixing of momentum. Thus a shallow surface Ekman layer forms wherein the wind momentum is confined to the surface layer (e.g., above the pycnocline depth). Hence the along-shore flow is substantially greater at the surface than below the pycnocline. While we do not have measurements of the stratification throughout the open water period, the mean velocity shear in **Figure 77** suggests that the depth of the pycnocline during upwelling conditions in July and August 2002 is at about 1 – 2 m and so consistent with the CTD transect collected in June 2001. We note that the difference in speeds and velocity structure are not due to the winds being stronger to the west than to the east during the 2002 open water season. In fact, the mean wind stress was strongly eastward during this season (**Figure 8**) although these did not cause swifter surface velocities than those observed under the weaker westward wind stress. An understanding of the asymmetric response to upwelling and downwelling favorable winds in the presence of stratification is extremely important for understanding the regional circulation field.

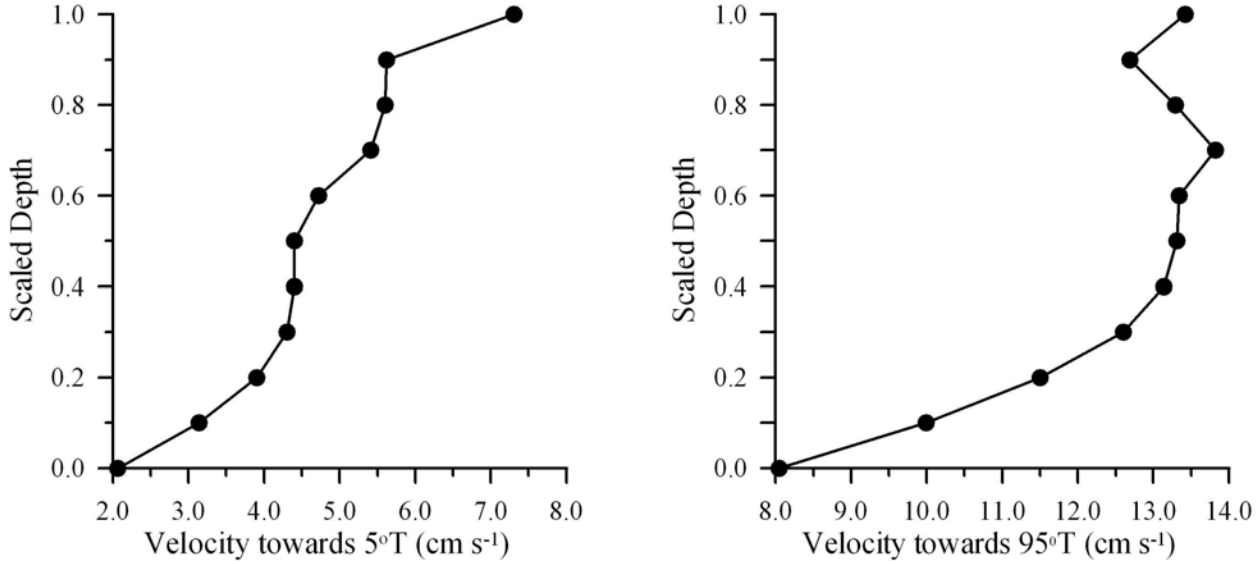

Figure 76. Mean velocity profiles for the cross-shore (left) and alongshore (right) velocity components during eastward flow conditions at REINDEER for the open water season.

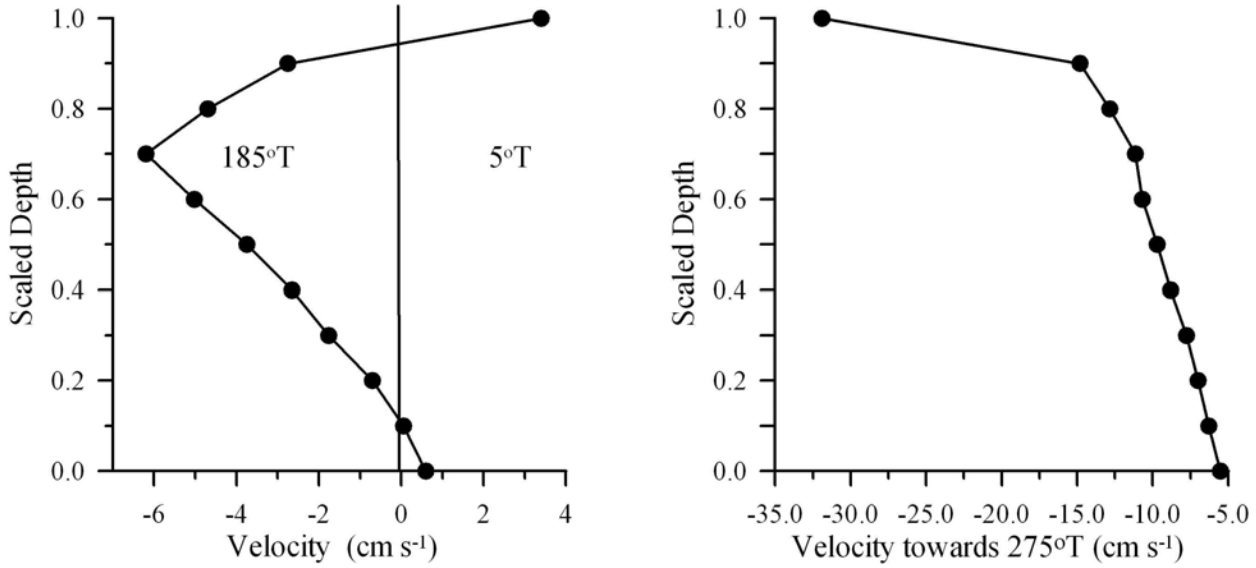

Figure 77. Mean velocity profiles for the cross-shore (left) and alongshore (right) velocity components during westward flow conditions at REINDEER for the open water season.

The character of the plume is expected to change seasonally, as shown schematically in **Figure 78,** from the shallow, strongly-stratified and surface-advected plume (red) of early summer to the bottom-advected plume type of late summer and fall (blue). The latter develops in late summer and fall after mixing has destroyed the

stratification and likely includes a swift alongshore geostrophic flow embedded within the front that can carry materials eastward along the Alaskan coast. Moreover the front effectively blocks cross-shelf transport and so materials shoreward of the front tend to remain trapped there unless the flow is interrupted by upwelling winds and/or frontal instabilities.

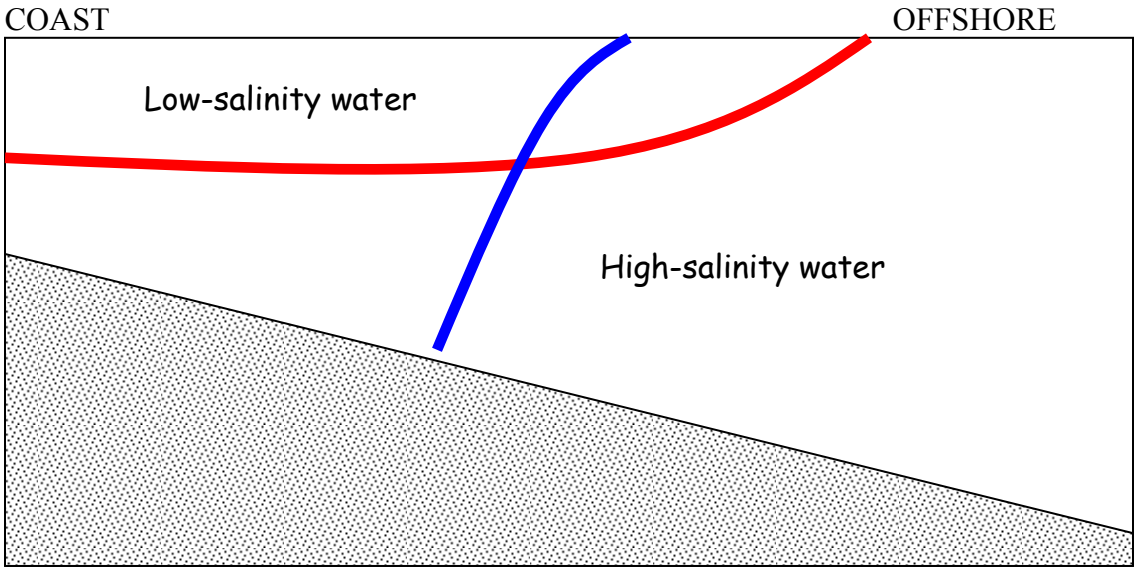

Figure 78. Schematic of the freshwater plume types likely to form in summer and fall in the nearshore region of the Beaufort Sea.

Instabilities have been observed in satellite images of the Alaskan Beaufort Sea (**Figures 79 - 81**). Although not directly wind-driven, the frontal structure and hence the characteristics of the instability do depend upon the seasonal wind history as these affect the frontal structure through mixing. The images show tongues of turbid water extending from near the coast to the shelfbreak and beyond (in some cases more than 100 km offshore). While **Figures 79 and 80** suggest that the plumes may be restricted to portions of the shelf, **Figure 81** indicates that the entire shelf may be enveloped by a series of unstable waves along the frontal boundary separating relatively fresh inshore waters from

saltier offshore waters. In **Figure 81**, this front appears to extend to the shelfbreak. The flow in these unstable plumes has not been measured in the Alaskan Beaufort Sea.

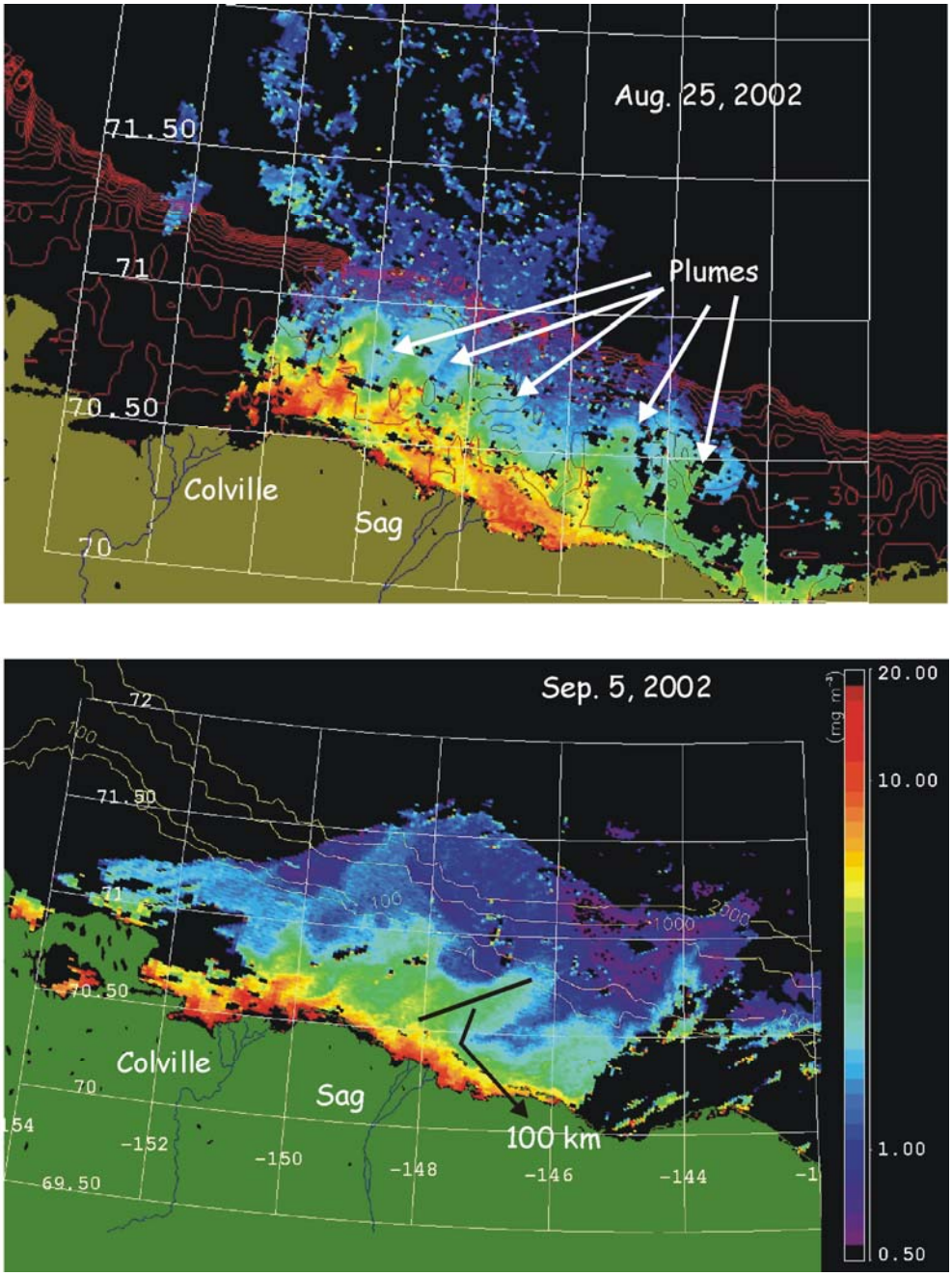

Figure 79. Beaufort Sea SeaWIFS imagery from August 25, 02 (upper panel) and September 5, 02 (lower panel). Winds were weak and variable for the week preceding these images. (Imagery courtesy of G. M. Schmidt with MODIS/Aqua data obtained from Ocean Color Data Processing Archive NASA / Goddard Space Flight Center Greenbelt, MD – USA.)

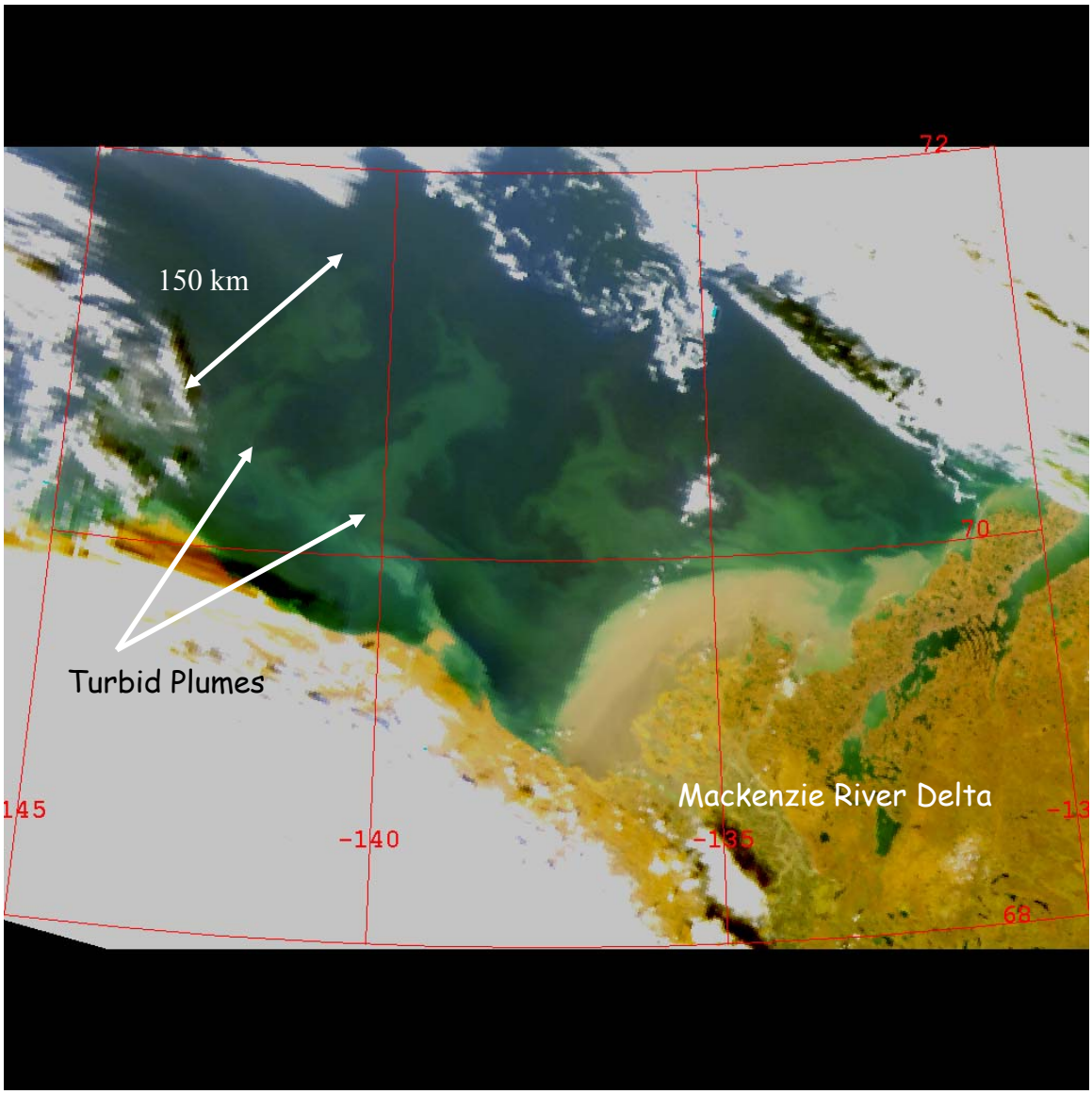

Figure 80. Visible SeaWIFS image from September 4, 2404 showing turbid plumes extending seaward from the Alaskan Beaufort Sea shelf across the continental slope. (Imagery courtesy of G. M. Schmidt with MODIS/Aqua data obtained from Ocean Color Data Processing Archive NASA / Goddard Space Flight Center Greenbelt, MD – USA.)

However, *Weingartner et al.* [1999] sampled similar features associated with the buoyancy-forced Siberian Coastal Current in the Chukchi Sea and found cross-shore velocities of up to 30 cm-s^{-1}. Thus, instabilities could rapidly transport materials and pollutants from the nearshore Beaufort Sea offshore and possibly, based on these images, across the shelfbreak and along the major fall migration corridor for bowhead whales.

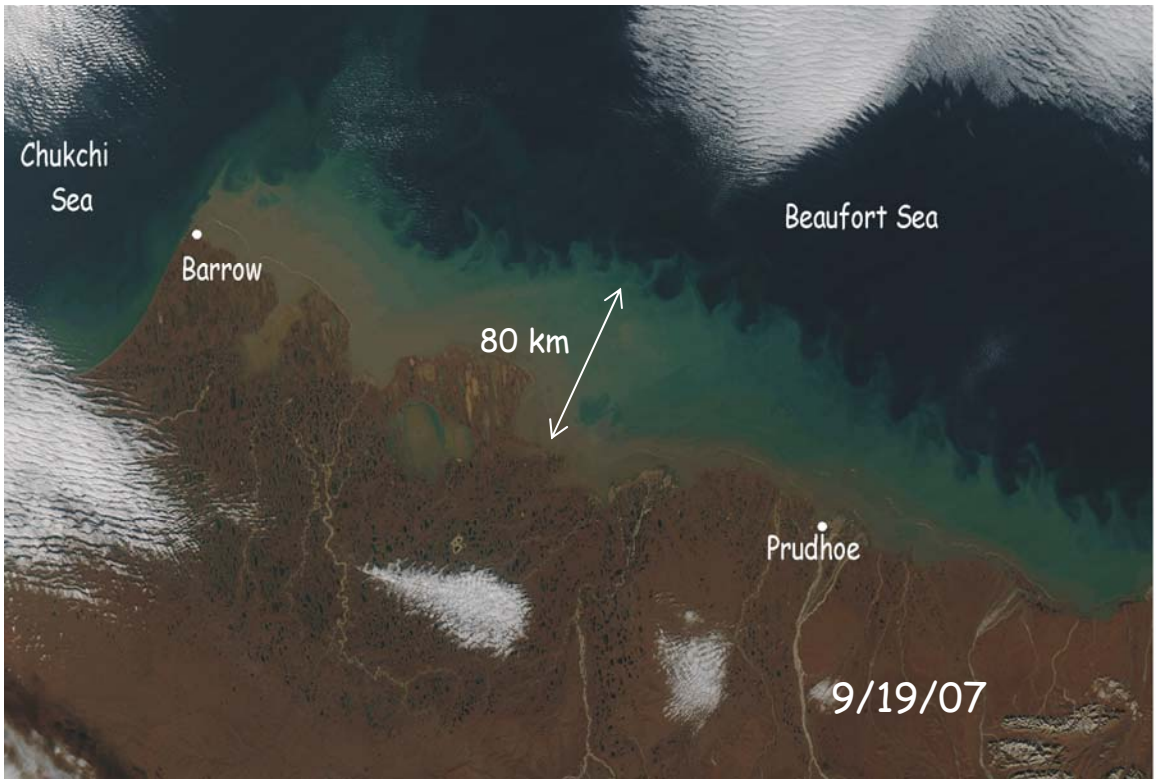

Figure 81. A September 18, 2007 MODIS image of the ABS shelfbreak showing a train of unstable waves developing along a turbid front at the edge of the shelfbreak.

We conclude this section by noting that in addition to the buoyancy influx from the small rivers emptying into the Alaskan Beaufort Sea, waters from the Mackenzie Shelf, diluted by the enormous outflow from the Mackenzie River may also influence the ABS. Under westward winds, portions of this plume flow westward. As suggested by the sequence of three thermal images, obtained between July 7 and July 27, 2007 (**Figure 82)**, this relatively warm water advection enhances sea ice melt over the ABS. The dispersal of Mackenzie plume waters is clearly dependent upon the wind stress (*Melling*, 1988), however, the preponderance of westward winds suggests that, at least during the

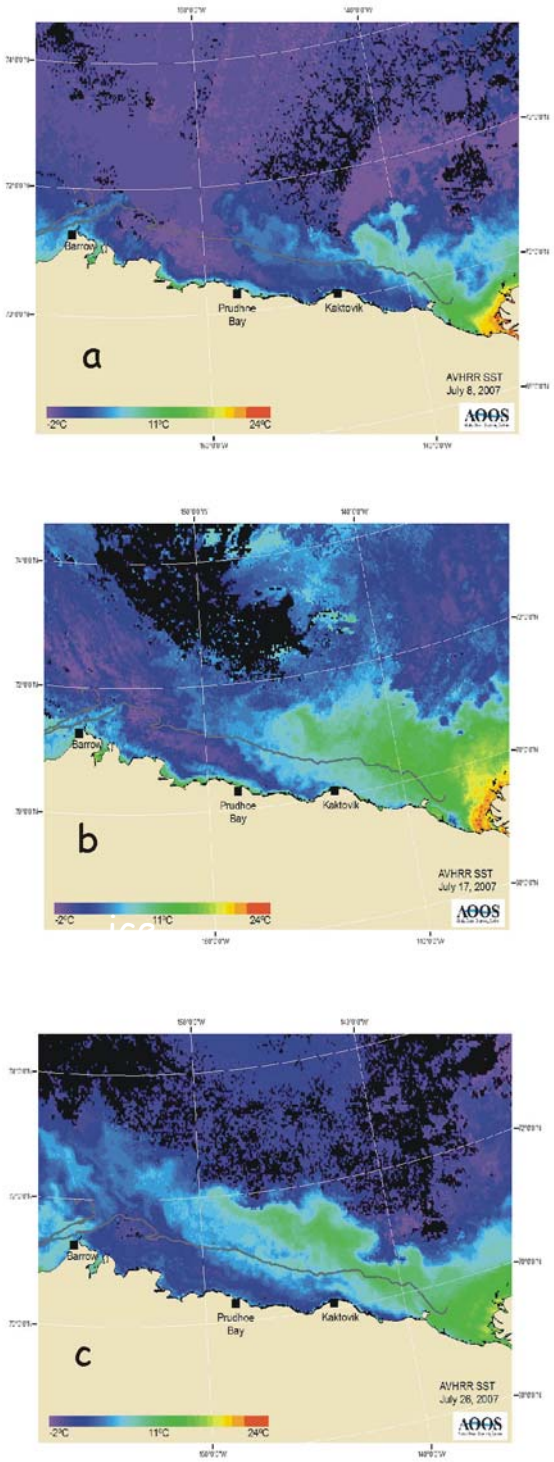

Figure 82. A sequence of AVHRR thermal images over the Alaskan Beaufort Sea on a) July 8, b) July 17, and c) July 26. Black indicates clouds, blue is sea ice and other colors are according to the temperature scale.

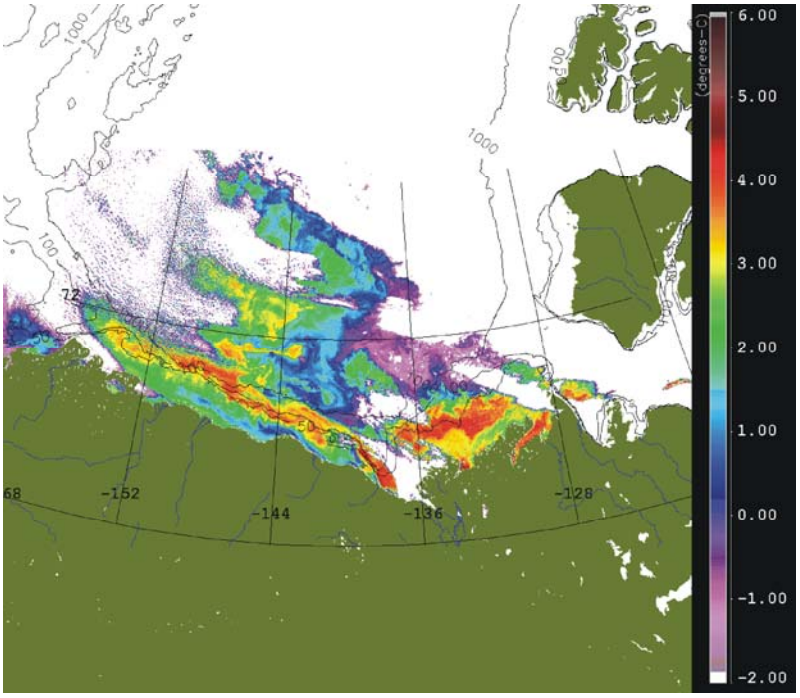

Figure 83. September 16, 2008 thermal image of the Beaufort Sea shelf showing relatively warm Mackenzie plume waters advected westward onto the ABS. (Imagery courtesy of G. M. Schmidt with MODIS/Aqua data obtained from Ocean Color Data Processing Archive NASA / Goddard Space Flight Center Greenbelt, MD – USA.)

open water season much of this water is transported westward (**Figure 83**) through the fall. For example, **Figure 84** (left panel) shows the mean (Sept. 28 – Oct. 22, 2006) surface velocity field within and offshore of Stefansson Sound as estimated from shore-based, high-frequency, surface current mapping radars. Although westward on average, the flow varied between being eastward and westward (**Figure 84**; right panel) in accordance with the winds throughout this 25-day period. On average the surface currents were ~20 cm s^{-1}, which if assumed to be uniform along the ABS means that water parcels drifted more than 400 km westward. Hence, waters from the Mackenzie shelf could easily have been advected into this area during this time period.

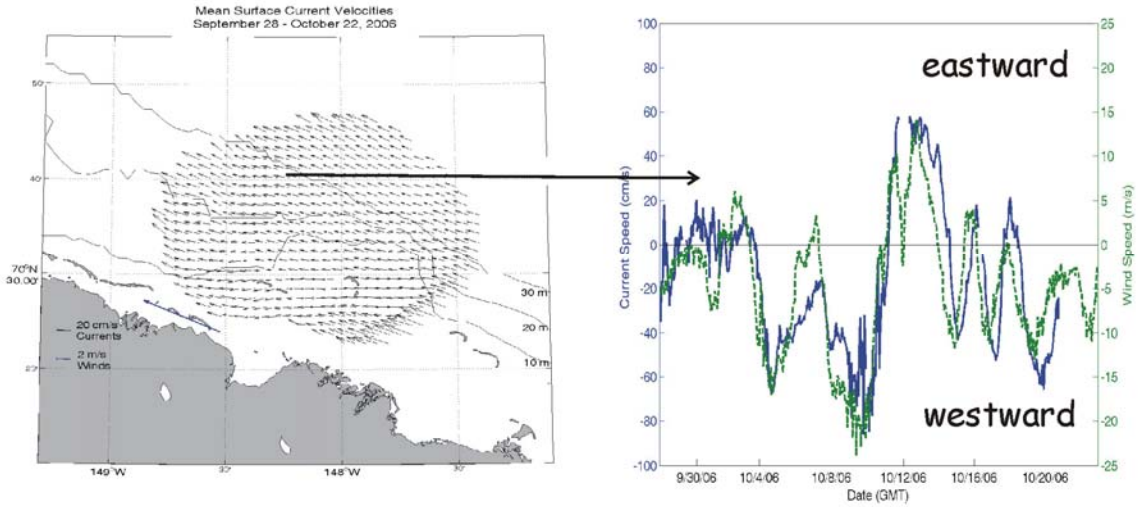

Figure 84. The left panel shows the September 28 – October 22 mean surface currents estimated from a shore-based surface current mapping radar deployed on the Alaskan coast in the vicinity of Prudhoe Bay. The right panel shows the time series of the currents (blue) at one point within the radar mask and winds (red).

VI. CONCLUSIONS AND RECOMMENDATIONS

Six years of current meter and water property measurements were made in the nearshore region of the Alaskan Beaufort Sea to assess circulation dynamics of the region within the landfast ice. The measurements were made year-round from moored instruments deployed in and offshore of Stefannsson Sound and elsewhere along the coast of the Alaskan Beaufort Sea. The data reveal a pronounced seasonal cycle that is associated with the formation and ablation of the landfast ice.

The mean flow, whether averaged over the entire record or by season, is small and is seldom significantly different from zero. It is, however, highly variable in time with the dominant mode of variability being in the along-shore direction. During the open water season the currents can be swift (10 – 50 cm-s^{-1} and occasionally approach 100 cm-s^{-1}), strongly sheared, especially when the flow is westward, and significantly correlated with the winds. During the landfast ice season currents are small (generally ~5 cm-s^{-1}), weakly sheared, and uncorrelated with winds. Progressive vector diagrams suggest that under the

landfast ice 90% of oil spilled will remain within 20 km of the origin of the spill site, while during the open water season 90% of spilled oil will remain within 200 km of the origin. Our measurements suggest that most of the oil will be dispersed in the along-shore direction.

Nevertheless, the winter sub-tidal flow variance implies fluctuating along-shore sea level gradients of about 10^{-6}. The along-shore velocity is coherent with the along-shore bottom pressure difference. The origin of these pressure gradients is not known, although preliminary model results suggest that along- and cross-shore variations in the underice friction coefficient can establish these gradients. The modeling and observations suggest that the underice current field is sensitive to the underice topography, which is poorly known.

Freshwater discharge associated with the springtime freshet creates shallow, strongly stratified, underice plumes that likely spread up to 20 km or more offshore. The cross-shore flows associated with these plume can be as large as 10 cm-s^{-1} and are much larger than the cross-shore flows generally observed beneath the landfast ice in winter. Little is known about these plumes, although they provide a vehicle by which nearshore suspended and dissolved materials can be carried offshore by spreading of the plume beneath the ice, offshore Ekman transport (once the ice breaks up), or through frontal instabilities. The latter generate large cross-shelf plumes that can extend across the Beaufort shelf and slope. Measurements obtained from similar features in the Chukchi Sea indicate that cross-shelf velocities associated with these instabilities can be ~25 cm-s^{-1}. We recommend that measurements be conducted to quantify the flow within these cross-shore jets and to determine the mechanisms by which they are generated.

Stratification due to freshwater inflow leads to a strong asymmetric response in the velocity shear between upwelling (westward winds) and downwelling (eastward) conditions on the inner shelf. Westward surface flows are intensified during upwelling events because the wind's momentum is trapped to a strongly stratified surface layer, while eastward surface currents are weaker during downwelling because stratification is weaker and the momentum from the surface stress is mixed over a deeper layer. The results imply that circulation models must correctly incorporate runoff and stratification in order to reproduce the surface circulation field correctly. Observations of the seasonal evolving stratification are needed to better understand this asymmetry and for model evaluations.

The seasonal cycle in sediment transport likely consists of rapid deposition from the freshwater plume as it spreads beneath the sea ice followed by re-suspension events during the open water season. Upon re-suspension, sediments can be advected offshore within the coastal flows or carried offshore due to instabilities. Re-suspension appears to be most vigorous during fall freeze-up due to storms and perhaps by sediment re-suspension by frazil ice. Sediments are incorporated into the landfast ice at this time (*Barnes et al*., 1982; *Reimnitz et al*., 1990) where it remains until the landfast ice melts or drifts away in the following summer. Hence sediments can be transported by both the currents or within sea ice, although it is not known how the load is partitioned between the two. While the present study results bear solely on oil in water, the fate of sediments and landfast ice are relevant to the pollutant transport issue as well. For example, spilled oil can adhere to sediments and discharged muds and cuttings can be placed on the top of solid ice during winter drilling operations. We recommend studies that examine the fate

of the landfast ice after breakup. Such a study would examine the proportion of landfast ice that melts *in-situ* melt versus the fraction that drifts away from a region and subsequently melts. In addition, we recommend studies that address sediment transport processes on this shelf. This requires understanding the wave climate on the ABS, which is likely changing due to apparent increases in duration of the open water season and sea ice extent.

Our data suggest that oil is unlikely to be carried far in the event of a spill beneath the landfast ice assuming that the *Cox and Schmidt* [1980] and *Buist et al.* [2008] laboratory measurements apply to this region of the Beaufort Sea. These laboratory measurements suggest that oil in contact with the ice will not move under the influence of the current speeds typically observed. However, oil in the water column will be transported back and forth along the coast. In the event of an underice spill here, the rate and direction of the spreading oil can be monitored easily because the current field is spatially coherent over ~100 km in the alongshore direction. Thus a single current meter can be lowered through a hole in the ice and configured to transmit current data in real-time to the spill recovery team. Direct measurements are required because of the absence of a significant wind-current correlation in winter.

Oil spilled beneath the ice during the spring freshet could be carried offshore in the Alaskan Beaufort Sea by underice river plumes. Theories developed for mid-latitude settings on the offshore extent of a river plume discharged into the sea suggests that oil might be carried at least 20 km offshore during the spring freshet. However, these theories do not consider the possibly complex frictional coupling between the ice and flow field or the impulsive nature of arctic river discharges. We recommend that

theoretical and observational studies be conducted in the Alaskan Beaufort Sea directed at understanding the underice spreading of river plumes. We believe that the current measuring techniques developed in this project can be applied to such a study.

The complex deformation field of the landfast ice regime suggests that frictional coupling between ice and currents will vary substantially over that portion of the shelf impacted by this ice type. In conjunction with the flow field, the underice topography affects both skin and form drag [*McPhee*, 1990] and could steer currents. Measurements and models are required to quantify this frictional coupling. As a first step it is critical that the temporal and spatial scales of variability of the underice topography be determined. Hence, we recommend that mapping the ice topography be conducted several times per winter over a variety of along- and cross-shore spatial scales. The larger horizontal scales (~40 m) can be mapped efficiently using airborne electromagnetic sensors and laser profilometry, whereas smaller scales will require ground-based measurements.

Based upon preliminary numerical modeling activities, it appears that there is little exchange between waters beneath the landfast ice and those offshore. This topic needs further exploration using models and observations. Direct current measurements offshore of Harrison Bay are now underway to examine this linkage. Another integrated observational approach that would be relatively simple to undertake would be to measure the $\delta^{18}O$ fraction in ice cores in spring after the ice reaches its maximum thickness. Since this isotope ratio is substantially different between sea-water and river water, spring ice cores will precisely record when the river water was exhausted from the nearshore region [*Macdonald et al*., 1999b]. This will lead to a distinct horizon in the ice core of the

isotope ratio transition. The timing of the transition can be determined by calculating ice growth rate from coastal meteorological data. This is a relatively inexpensive procedure that would provide a measure of year-to-year differences in the rate of freshwater depletion from the nearshore Beaufort Sea after the landfast ice forms.

Finally, satellite imagery suggests that the Mackenzie River has an important influence on the sea ice regime of the ABS. It likely plays an important dynamical role also, especially in the eastern Beaufort Sea, where it will affect stratification and the wind-forced response of the shelf during the open water season and perhaps the underice flow regime in winter. We recommend that the connection between the Mackenzie shelf and the eastern Beaufort Sea be investigated with Canadian science partners.

ACKNOWLEDGEMENTS

We are grateful for the financial support provided by the Minerals Management Service and the equipment provided by the Alaska Department of Environmental Conservation. We thank Dave Leech for his expertise in designing and deploying the moorings and for his cheerful approach throughout the project. Dr. John Trefey assisted with the 2001 CTD measurements. Heloise Chenelot, Caleb Conley, and Markus Janout assisted with the dive recoveries on some of the moorings. G. Michael Schmidt kindly processed the ocean color images. Dr. Bill Streever (BP, Inc.) and BP, Inc. provided logistical support. Finally, we thank our MMS program manager, Dr. Richard Prentki, whose guidance and enthusiastic support contributed much to the success of the project.

REFERENCES

Aagaard, K., The Beaufort Undercurrent. IN: *The Alaskan Beaufort Sea: Ecosystems and Environment*, edited by P. W. Barnes, D. M. Schell, and E. Reimnitz, pp. 47-71. Academic Press, New York, 1984.

Aagaard, K., and A.T. Roach, Arctic ocean-shelf exchange: Measurements in Barrow Canyon, *J. Geophys. Res.*, *95*, 18163-18175, 1990.

Barnes, P. W., D. M. Rearic, and E. Reimnitz, Ice gouging characteristics and processes IN: *The Alaskan Beaufort Sea: Ecosystems and Environment*, edited by P. W. Barnes, D. M. Schell, and E. Reimnitz, pp. 185 - 212. Academic Press, New York, 1984.

Barnes, P. W., E. Reimnitz, and D. Fox Ice rafting of Fine-Grained Sediment, a Sorting and Transport Mechanism, Beaufort Sea, Alaska. *J. Sed. Petrol.* 52 (2), 493-502. 1982

Barnes and Reimnitz, 1974 IN The Coast and Shelf of the Beaufort Sea (JC Reed and J E Sater, eds.) p. 439, Arctic Institute of North America, Arlington, VA. 1974

Benjamin, T. B., Gravity currents and related phenomena, *J. Fluid Mech., 31, (2),* 9 – 248, 1968

Brower, W. A., Jr., R. G. Baldwin, C. N. Williams, Jr., J. L .Wise, and L.D. Leslie, *Climate atlas of the outer continental shelf waters and coastal regions of Alaska*, *volume III, Chukchi-Beaufort Sea*, 497 pp., National Climatic Data Center, Asheville, NC, 28801, 1988.

Buist, I., R. Belore, D. Dickins, D. Hackenberg, A. Guarino, and W. Zhang, *Empirical Weathering Properties of Oil in Ice and Snow*. Final Report Project Number 1435-01-04-RP-34501. [http://www.mms.gov/alaska/reports/2008rpts/2008_033/2008_033.pdf] U.S. Dept. Int., Minerals Management Service, Alaska Outer Continental Shelf Region, Anchorage Alaska. 154 p. 2008.

Carmack, E. C., R. W. Macdonald, and J. E. Papdakis, Water mass structure and boundaries in the Mackenzie Shelf Estuary, *J. Geophys. Res., 94*, 18043-18055, 1989.

Chapman, D. C. and S. J. Lentz, Trapping of a coastal density front by the bottom boundary layer, *J. Phys. Oceanogr., 24*, 1464-1479, 1994.

Colonell, J. M. and B. J. Galloway, Wind-driven transport and dispersion of age-0 arctic ciscoes along the Alaska Beaufort coast. IN: *Fish Ecology in Arctic North America*, American Fisheries Society Symposium 19, Bethesda, MD., p – 90 – 103, 1997.

Cox, J. C. and I. A. Schultz, The transport and behavior of spilled oil under ice. Proceedings of the Third Annual Technical Seminar, Arctic Marine Oil Spill Program, Edmonton, June 1979, p. 45 – 61, 1980.

Csanady, G. T. Circulation in the Coastal Ocean, D. Reidel, Boston, p. 279, 1982.

Danielson, S. L. and T. J. Weingartner, Estimates of Oil Spill Dispersion Extent in the Nearshore Alaskan Beaufort Sea Based On In-Situ Oceanographic Measurements prepared for ADEC, 154 pp., 2007 (available at http://www.ims.uaf.edu/beaufort/index3.html).

Danielson, S. L. and Z. Kowalik, Tidal currents in the St. Lawrence Island region. *J. Geophys. Res.,* in press.

Dean, K. G., W. Stringer, K. Ahlnaes, S.C. Searcy, and T. Weingartner, The influence of river discharge on the thawing of sea ice: Mackenzie River Delta: Albedo and temperature analysis, *Polar Res., 13*, 83-94, 1994.

Dunton, K. H., E. Reimnitz, and S. V. Schonberg, An arctic kelp community in the Alaskan Beaufort Sea, *Arctic, 35*: 465 – 484., 1982.

Denman, K. L. and M. Miyake, Upper layer modification at ocean station Papa: observations and simulation, *J. Phys. Oceanogr*., 3, 185 – 196, 1973.

Guay, C. K. and K. K. Falkner, A survey of dissolved barium in the estuaries of major Arctic rivers and adjacent seas. *Cont. Shelf Res., 8:* 859 – 882, 1998.

Foreman, M. G.G. Manual for Tidal Currents Analysis and Prediction. Pacific Marine Science Report 78-6, Institute of Ocean Sciences, Patricia Bay, Sidney, B.C., 1978, 70 pp.

Furey, P., The large-scale surface wind field over the western Arctic Ocean, 1981 – 1993, MS thesis, 121 pp. Univ. of Alaska, Fairbanks, 1998

Kowalik, Z. and A. Y. Proshutinsky, The Arctic Ocean Tides, in *The Polar Oceans and Their Role in Shaping the Global Environment; Geophys. Monogr. 85,* pp. 137-158, edited by O. M. Johannessen, R. D. Muench and J. E. Overland, Amer. Geophys. Union, Washington, DC, 1994.

Kozo, T. L., An observational study of sea breezes along the Alaska Beaufort Sea coast, *J. Appl. Met. 21*: 891- 905, 1982a.

Kozo, T. L., An mathematical model of sea breezes along the Alaska Beaufort Sea coast, *J. Appl.* Met. 21: 906 - 924, 1982b.

Kozo, T. L. Mesoscale wind phenomena along the Alaskan Beaufort Sea coast. IN: *The Alaskan Beaufort Sea: Ecosystems and Environment*, edited by P. Barnes and E. Reimnitz, pp. 23 - 45. Academic Press, New York, 1984.

Kozo, T. L. Mountain barrier baroclinicity effects on surface winds along the Alaskan Arctic coast. *Geophys. Res. Lett*., 7, 377 – 380, 1980.

Lentz, S. J. Current dynamics over the northern California inner shelf, *J. Phys. Oceanogr.,* 24, 2461 – 2478, 1994.

Lentz, S., R. T. Guza, S. Elgar, F. Fedderesen, and T.H. C. Herbers, Momentum balances on the North Carolina inner shelf, *J. Geophys. Res.,* 104, 185 – 18226, 1999.

Liu, A. K., C. Y. Peng, and T. J. Weingartner (1994), Ocean-ice interaction in the marginal ice zone using SAR. *J. Geophys. Res*., 99, 22391 – 22400.

Macdonald, R.W., E.C. Carmack, F. A. McLaughlin, K. K. Falkner, and J. H. Swift, Connections among ice, runoff, and atmospheric forcing in the Beaufort Gyre, *Geophys. Res. Lett.,* 26:15:2223 – 2226*,* 1999a.

MacDonald, R. W., E. C. Carmack, and D. W. Paton. Using the delta ^{18}O composition in landfast ice as a record of arctic estuarine processes. *Mar. Chem*. 65: 3 – 24, 1999b.

Macdonald, R.W., E.C. Carmack, F. A. McLaughlin, K. Iseki, D.M. Macdonald, and M. C. O'Brien, Composition and Modification of water masses in the Mackenzie Shelf Estuary, *J. Geophys. Res., 94*, 18057-18070, 1989.

Macdonald, R. W. and E. C. Carmack, The role of large-scale under-ice topography in separating estuary and ocean on an arctic shelf. *Atmosphere-Ocean, 29*: 37 -51, 1991.

Matthews, J.B., Observations of Under-ice circulation in a shallow lagoon in the Alaskan Beaufort Sea, *Ocean Management*, 6, 223-234, 1981.

Maslanik, J. A., M. A. Serreze, and T. Agnew, On the record reduction in 1998 Western Arctic Sea ice cover, *Geophys. Res. Lett*., 26, 1905 – 1908, 1999.

Maykut, G. A. The surface heat and mass balance, IN: *The Geophysics of Sea Ice*, edited by N. Untersteiner, pp. 395 -464, Plenum Press, New York, NY, 1986.

McPhee, M. G., Small-Scale Processes. IN: *Polar Oceaongraphy Part A: Physical Science*, edited by W. O. Smith, Jr., pp. 287 - 280. Academic Press, New York, 1990.

Melling, H. 1993. The formation of a haline shelf front in a ice-covered arctic sea. *Continental Shelf Research.* **13**:1123-1147.

Morris, K., S. Li, and M. Jefferies, Meso- and microscale sea-ice motion in the East Siberian Sea as determined from ERS-1 SAR data. *J. Glaciol.,* 45(15): 370 – 383, 1999.

Mountain, D. G., Coachman, L. K., and K. Aagaard, On the flow through Barrow Canyon, *J. Phys. Oceanogr*. 6, 461 – 470, 1976.

Muench, R.D., 1990. A review of mesoscale processes in the polar oceans. In Polar Oceanography (W.O. Smith, ed.), Academic Press, NY, 223-285.

Nikolopoulos, A., R. S. Pickart, P. S. Fratantoni, K. Shimada, D. J. Torres, and E. P. Jones, The western Arctic boundary current at 152^{o}W: Structure, variability, and transport. *in press Deep-Sea Res*, *II*.

North, G. R., T. L. Bell, and R. F. Cahalan, Sampling Errors in the estimation of empirical orthogonal functions, *Monthly Weath. Rev., 110*, 699-706, 1982

Pawlowicz, R., B. Beardsley, and S. Lentz. Classical tidal harmonic analysis including error estimates in MATLAB using T.TIDE, *Comp. and Geosci*., 28, 929- 937, 02.

Pickart, R. S. Shelbreak circulation in the Alaskan Beaufort Sea: Mean structure and variability, *J. Geophys. Res*., 2004.

Pickart, R.S., T. Weingartner, L.J. Pratt, S. Zimmermann, and D. J. Torres, Flow of winter-transformed Pacific water into the western Arctic. *Deep-Sea Research*, *Pt. II*, 52: 3175 – 3198, 2005.

Reimnitz, E., Interaction of river discharge with sea ice in proximity of Arctic deltas: a review, *Polarforschung*, 70: 123 – 134, 00.

Reimnitz, E., E. W. Kempema, W. S. Weber, J. R. Clayton, and J. R. Payne, Suspended-Matter Scavenging by rising frazil ice. IN: *Sea Ice Properties and Processes: Proceedings of the W.F.Weeks Sea Ice Symposium*, edited by S.F. Ackley and W.F. Weeks, pp.97 - 100. Cold Regions Research and Engineering Laboratory Monograph, no 90-1. U.S. Army Cold Regions Research and Engineering Laboratory, 1990.

Reimnitz, E. and E. W. Kempema, Pack ice interaction with stamukhi shoal. IN: The Alaskan Beaufort Sea: Ecosystems and Environment, edited by P. W. Barnes, D. M. Schell, and E. Reimnitz, pp. 159 - 184. Academic Press, New York, 1984.

Searcy, C., K. Dean, and W. Stringer, A river-coastal sea ice interaction model: Mackenzie River Delta, *J. Geophys. Res., 101*, 8885-8894, 1996.

Tucker III, W. B., W. F. Weeks, and M. Frank, Sea Ice ridging over the Alaskan continental shelf, *J. Geophys. Res., 84*, 4885 – 4897, 1979.

Weingartner, T., J., S. R. Okkonen, and S. L. Daneilson. Circulation and Water Property Variations in the Nearshore Alaskan Beaufort Sea, Final Report, OCS Study MMS 2005-028, 103 p.

Weingartner, T., K. Aagaard, R. Woodgate, S. Danielson, Y. Sasaki, and D. Cavalieri (2005b), Circulation on the North Central Chukchi Sea Shelf. *Deep-Sea Res., Pt. II*, 52: 3150-3174, doi:10.1016/j.dsr2.2005.10.015.

Weingartner, T.J., S. Danielson, Y. Sasaki, V. Pavlov, and M. Kulakov, The Siberian Coastal Current: A wind- and buoyancy-forced arctic coastal current, *J. Geophys. Res.*, 104, 29697-29713, 1999.

Weingartner, T.J., D.J. Cavalieri, K. Aagaard, and Y. Sasaki, Circulation, dense water formation, and outflow on the northeast Chukchi shelf, *J. Geophys. Res.*, *103*, 7647-7661, 1998.

Wiseman et al., W.J., Suhayda, J.N., Hus, S.A., and Walters, C.D., IN The Coast and Shelf of the Beaufort Sea (JC Reed and J E Sater, eds.) p. 49, Arctic Institute of North America, Arlington, VA. 1974

Woodgate, R. A., K. Aagaard, and T. Weingartner (2005a), A Year in the Physical Oceanography of the Chukchi Sea: moored measurements from autumn 1990-91, *Deep-Sea Res., Pt II,* 52, 3116-3149.

Yankovsky, A. Interaction of transient shelf currents with a buoyancy-driven coastal current. *J. Mar. Res., 62,* 545–563, 2004.

Yankovsky, A. E. and D. C. Chapman, A simple theory for the fate of buoyant coastal discharges, *J. Phys. Oceanogr., 27,* 1386-1401, 1997.

The Department of the Interior Mission

As the Nation's principal conservation agency, the Department of the Interior has responsibility for most of our nationally owned public lands and natural resources. This includes fostering sound use of our land and water resources; protecting our fish, wildlife, and biological diversity; preserving the environmental and cultural values of our national parks and historical places; and providing for the enjoyment of life through outdoor recreation. The Department assesses our energy and mineral resources and works to ensure that their development is in the best interests of all our people by encouraging stewardship and citizen participation in their care. The Department also has a major responsibility for American Indian reservation communities and for people who live in island territories under U.S. administration.

The Minerals Management Service Mission

As a bureau of the Department of the Interior, the Minerals Management Service's (MMS) primary responsibilities are to manage the mineral resources located on the Nation's Outer Continental Shelf (OCS), collect revenue from the Federal OCS and onshore Federal and Indian lands, and distribute those revenues.

Moreover, in working to meet its responsibilities, the **Offshore Minerals Management Program** administers the OCS competitive leasing program and oversees the safe and environmentally sound exploration and production of our Nation's offshore natural gas, oil and other mineral resources. The MMS **Royalty Management Program** meets its responsibilities by ensuring the efficient, timely and accurate collection and disbursement of revenue from mineral leasing and production due to Indian tribes and allottees, States and the U.S. Treasury.

The MMS strives to fulfill its responsibilities through the general guiding principles of: (1) being responsive to the public's concerns and interests by maintaining a dialogue with all potentially affected parties and (2) carrying out its programs with an emphasis on working to enhance the quality of life for all Americans by lending MMS assistance and expertise to economic development and environmental protection.